

LATTICE BOLTZMANN MODELS FOR HEAT TRANSFER AND ANISOTROPIC FLOWS

by

Zimeng Wang

A thesis submitted in partial fulfillment
of the requirements for the degree of
Master of Science (MSc) in Natural Resources Engineering

The Faculty of Graduate Studies
Laurentian University
Sudbury, Ontario, Canada

© Zimeng Wang, 2019

THESIS DEFENCE COMMITTEE/COMITÉ DE SOUTENANCE DE THÈSE
Laurentian Université/Université Laurentienne
 Faculty of Graduate Studies/Faculté des études supérieures

Title of Thesis Titre de la thèse	Lattice Boltzmann Models for Heat Transfer and Anisotropic Flows	
Name of Candidate Nom du candidat	Wang, Zimeng	
Degree Diplôme	Master of Science	
Department/Program Département/Programme	Engineering	Date of Defence Date de la soutenance October 16, 2019

APPROVED/APPROUVÉ

Thesis Examiners/Examineurs de thèse:

Dr. Junfeng Zhang
(Supervisor/Directeur(trice) de thèse)

Dr. Brahim Chebbi
(Committee member/Membre du comité)

Dr. Helen Shang
(Committee member/Membre du comité)

Dr. Sebastien Leclair
(External Examiner/Examineur externe)

Approved for the Faculty of Graduate Studies
 Approuvé pour la Faculté des études supérieures
 Dr. David Lesbarrères
 Monsieur David Lesbarrères
 Dean, Faculty of Graduate Studies
 Doyen, Faculté des études supérieures

ACCESSIBILITY CLAUSE AND PERMISSION TO USE

I, **Zimeng Wang**, hereby grant to Laurentian University and/or its agents the non-exclusive license to archive and make accessible my thesis, dissertation, or project report in whole or in part in all forms of media, now or for the duration of my copyright ownership. I retain all other ownership rights to the copyright of the thesis, dissertation or project report. I also reserve the right to use in future works (such as articles or books) all or part of this thesis, dissertation, or project report. I further agree that permission for copying of this thesis in any manner, in whole or in part, for scholarly purposes may be granted by the professor or professors who supervised my thesis work or, in their absence, by the Head of the Department in which my thesis work was done. It is understood that any copying or publication or use of this thesis or parts thereof for financial gain shall not be allowed without my written permission. It is also understood that this copy is being made available in this form by the authority of the copyright owner solely for the purpose of private study and research and may not be copied or reproduced except as permitted by the copyright laws without written authority from the copyright owner.

Abstract

Fluid flows and associated heat and mass transfer problems are governed by several nonlinear second-order partial differential equations for which the analytical solutions are hard to obtain. Therefore, the numerical simulations are very useful in the research of the flow and heat transfer problems. In the last decade of the 20th century, a relatively new computational fluid dynamic (CFD) method, so called the lattice Boltzmann method (LBM) was proposed. The method is coding and meshing friendly and is rapidly developing in recent years.

In this thesis, three new methods for the flow and heat transfer based on the LBM are presented. First, we give a counter-extrapolation approach to calculate the heat and mass transfer problems between conjugate interfaces with the interfacial discontinuity. By applying the finite difference approximation and extrapolation, the conjugate interface problem can be separated into two individual heat and mass transfer problems with Dirichlet boundaries, and the Dirichlet boundary problems can be solved by applying the LBM (or other CFD methods).

Secondly, we consider the inlet and outlet treatment of periodic thermal flow. The periodic features of fully developed periodic incompressible thermal flows will be carefully examined by applying the LBM. The distribution modification (DM) approach and the source term (ST) approach are proposed, which can be both used for periodic thermal flows with constant wall temperature (CWT) and surface heat flux boundary conditions.

The last method is a rectangular lattice Boltzmann model for anisotropic flows based on coordinate and velocity transformation. Unlike the other existing rectangular models which tuned the lattice Boltzmann algorithm to fit the rectangular or cuboid lattice grids, this method applies the general lattice Boltzmann method to solve the transformed system over regular square lattice grids.

All these methods have been carefully examined in several simulations by comparing the LBM results to those of analytical solutions and previous publications using

different numerical techniques. The results of the first and second methods are satisfactory. However, the result of the last method for the rectangular lattice Boltzmann model suffers numerical instability and inaccuracy. The reason has been analyzed, and a possible reform has also been suggested. The future research topics for each method have been proposed as well.

Acknowledgements

I would like to express sincere thanks to my supervisor, Professor Junfeng Zhang for his instructive suggestions in my Master program. I am grateful to Dr. Brian Wong for his support to my research on the blood flow simulation project. I would also give my thanks to my current and former lab members, Ping Li, Mayssaa Jbeili, Farhad Amiri, Sudip Das, Ayoub Msaddak, Othmann Oulaid, and Vivek Joshi. I appreciate Professor Guigao Le for his support as well.

Contents

Abstract	iii
Acknowledgements	v
1 Introduction	1
2 Heat and Mass Transfer Between Discontinuous Conjugate Interfaces	5
2.1 Introduction	5
2.2 Theory and Methods	8
2.2.1 Governing Equations and Conjugate Interface Condition	9
2.2.2 LBM Model for Transport Phenomenon	10
2.2.3 The Counter-Extrapolation Method	12
2.3 Validation and Demonstration Simulations	15
2.3.1 One-Dimensional Steady Diffusion System	15
2.3.2 Steady and Unsteady Convection-Diffusion Processes with a Flat Interface	17
Model Description and Analytical Solution	17
Steady Simulation	18
Unsteady Simulation	20
2.3.3 Steady Diffusion System with a Circular Interface	23
2.3.4 Accuracy Analysis	24
2.3.5 Cooling Process of a Hot Cylinder in a Cold Flow under Dif- ferent Insulation Conditions	29
2.4 Summary and Concluding Remarks	35
3 Inlet And Outlet Treatment of Periodic Thermal Flow	39

3.1	Introduction	39
3.2	Theory and Methods	42
3.2.1	Fully Developed Periodic Thermal Flows	42
3.2.2	Simulating Periodic Thermal Flows with LBM	47
	For Flow Field	47
	For Thermal Field: The Source Term (ST) Approach	48
	For Thermal Field: The Distribution Modification (DM) Ap- proach	49
3.3	Validation and Demonstration Simulations	50
3.3.1	Heat Transfer of Laminar Flow through 2D Flat Channel	51
3.3.2	Heat Transfer of Laminar Flow through 2D Wavy Channel	53
3.3.3	Heat Transfer in Flow through Square Cylinder Array	56
3.4	Summary and Concluding Remarks	59
4	Rectangular LBM For Anisotropic Flows	64
4.1	Introduction	64
4.2	Coordinate and Velocity Transform to Reduce System Anisotropy	66
4.3	Simulations and Discussions	68
4.3.1	Poiseuille Flow in Straight Channel	68
4.3.2	Taylor-Green Vortex	70
4.3.3	Flow through Wavy Channel	73
4.3.4	Flow through a Model Anisotropic Porous Medium	75
4.3.5	Stability and Accuracy Analysis and Discussions	77
4.4	Summary and Concluding Remarks	80
5	Conclusion and Further Research	82
5.1	Conclusion	82
5.2	Future Research	83
A	The Double-Distribution Thermal LBM Model	85
B	The Analytical Solution for Developed Thermal Flow	88

List of Figures

- 2.1 Schematic illustrations for method description: (a) the D2Q5 lattice structure, (b) the counter-extrapolation method for conjugate interfaces, (c) the bilinear interpolation operation for estimating the property at an arbitrary position \mathbf{x} from its four neighboring lattice nodes, and (d) the ϕ distribution profile with discontinuity across the interface along the normal direction. 8
- 2.2 Effects of the interface conductance on the ϕ profile across the gap between two parallel plates. The interface locates at $y = H/2$. The LBM results are displayed as symbols in comparison to the corresponding theoretical solutions from Eq.(2.27) as solid lines. 15
- 2.3 The schematic for the flat interface system used in steady and unsteady convection-diffusion simulations. The relative position of the interface to the underlying lattice grid is denoted the offset Δ , the distance from the interface to the first lattice grid line below it. 17

- 2.4 The ϕ distributions in the computational domain (a), the ϕ profiles along $x/L = 0, 0.25, 0.5,$ and 0.75 across the interface at $y/H = 0.5$ (b), the variations of interfacial values $\phi_{int, 1}$ and $\phi_{int, 2}$ along the interface (c), and the variations of the interfacial gradients $(\partial\phi/\partial n)_{int, 1}$ and $(\partial\phi/\partial n)_{int, 2}$ along the interface (d) for the steady convection-diffusion system with a flat interface. In (a) the background color patches are from our LBM calculation and the black contour lines are from the analytical solution. In (b)-(d) the symbols are LBM results and the underlying curves are theoretical predictions. The dashed lines in (a) and (b) indicate the interface location; and the dashed lines in (c) and (d) are used to separate the positive and negative scalar or gradient values along the interface. 19
- 2.5 The variations of the ϕ values in separate domains (a) and the interfacial scalar (b) and gradient (c) values with simulation time for the unsteady convection-diffusion system with a flat interface. The symbols are LBM results and the underlying curves are from analytical solution Eq.(2.29). 20
- 2.6 The ϕ distributions (a), the ϕ profiles along $x/L = 0, 0.25, 0.5,$ and 0.75 (b), the variations of interfacial values $\phi_{int, 1}$ and $\phi_{int, 2}$ along the interface (c), and the variations of interfacial gradients $(\partial\phi/\partial n)_{int, 1}$ and $(\partial\phi/\partial n)_{int, 2}$ along the interface (d) for the unsteady convection-diffusion system with a flat interface at $t = 4\pi/\omega$. In (a) the background color patches are from our LBM calculation and the black contour lines are from the analytical solution. In (b)-(d) the symbols are LBM results and the underlying curves are theoretical predictions. The dashed lines in (a) and (b) indicate the interface location; and those in (c) and (d) are used to separate the positive and negative scalar and gradient values. 21

- 2.7 The schematic of the steady diffusion system with a circular interface at $r = R_1$, which separates the two coaxial domains Ω_1 for $r < R_1$ and Ω_2 for $R_1 < r < R_2$. Different transport parameters are assigned to the two domains, and a steady but non-uniform boundary condition as given by Eq.(2.34) is imposed at the outer boundary at $r = R_2$ 24
- 2.8 The ϕ distributions (a), the ϕ profiles along $\theta = 0$ and $\pi/4$ (b), the variations of interfacial values $\phi_{int, 1}$ and $\phi_{int, 2}$ along the interface (c), and the variations of interfacial gradients $(\partial\phi/\partial y)_{int, 1}$ and $(\partial\phi/\partial y)_{int, 2}$ along the interface (d) for the steady diffusion system with a circular interface. In (a) the background color patches are from our LBM calculation and the black contour lines are from the analytical solution. In (b)-(d) the symbols are LBM results and the underlying curves are theoretical predictions. The dashed arc in (a) and the dashed vertical line in (b) indicate the interface location; The dashed lines in (c) and (d) are used to separate the positive and negative interfacial properties. 25
- 2.9 The relative errors E_2 (a1, b1, and c1), $E_{2, int, 1}$ (a2, b2 and c2), $E_{2, int, 2}$ (a3, b3 and c3), and $E_{2, qint}$ (a4, b4 and c4) for the steady (a1-a4) and unsteady (b1-b4) convection-diffusion systems with a flat interface and the steady diffusion systems with a circular interface (c1-c4). Effects of the interface-lattice offset distance (a1-a4: $\Delta = 0.01$ as black circles, 0.5 as blue squares, and 0.75 as red diamonds), heat capacity ratio (b1-b4: $\sigma = 0.1$ as black circles, 1 as blue squares, and 10 as red diamonds), and interface conductance (c1-c4: $\lambda R_2/D' = 0.1$ as black circles, 2 as blue squares, and 100 as red diamonds) on the numerical accuracy have also been investigated. Straight lines with slope values are used to indicate the convergence order. 26
- 2.10 The schematic for simulations of the cooling processes of a hot cylinder in a cold flow. Fluid enters from the left edge of the simulation domain with density ρ_0 , velocity U_0 , and temperature T_0 , and domain boundary conditions are described in details in text. 29

- 2.11 The distributions of flow vorticity (top row) and temperature (lower three rows, one for each case simulated) at three representative time instants during the cooling processes of the system in Fig. 2.10. All three simulations start from the same initial condition with the fluid at rest of $T_f = T_0 = 0$ and the solid cylinder of $T_s = 1$. The temperature fields here are displayed using a same color scale for direct comparison; however, the color scale is limited in the range of $0 \sim 0.15$ (i.e., temperature higher than 0.15 will be shown in the same color, which is dark red here) so we can see the relatively low fluid temperature clearly. 31
- 2.12 Close pictures of the local temperature fields inside and around the solid cylinder during the cooling processes. The temperature fields here are displayed using a same color scale for direct comparison; and the color scale is set for the range of $0 \sim 0.40$ (i.e., temperature higher than 0.40 will be shown in the same color, which is dark red here) to show the temperature fields clearly. 37
- 2.13 The changes of the average temperature of the cylinder during the cooling process for the three cases studied. The decay behavior can be approximated as an exponential decay starting from the initial temperature $T_s = 1$. The dashed lines are best fittings according to the Newton cooling law Eq.(2.43). 38
- 2.14 The temperature distributions along the system centerline (center row) as well as at $30 \delta x$ above (top row) and below (bottom row) the centerline for the three cases studied at the three representative time instances $t^* = 5$ (left column), 20 (center column), and 50 (right column). The grey areas in the center row indicate the solid region of the cylinder. 38

3.1	Schematic illustration of the periodic flow passage. The vertical dashed lines are plotted to divide the flow passage into individual periodic modules. The coordinate system is set with the x direction in the flow direction and the y direction in the transverse direction.	42
3.2	Schematic illustrations of the modified periodic boundary treatment for thermal field. The inlet nodes are displayed as squares and the outlet nodes are shown as circles, with the color changing from black to white along the flow direction. The numbered arrows are used to show how a density distribution leaving the outlet can be adopted to specify the incoming distribution at the inlet. Please refer the text for detailed method description.	48
3.3	The simulated temperature field (a) and transverse profiles (b) for flow through the flat channel with CWT condition on the channel surfaces. In (b) the symbols are our LBM results and the underlying curves are from the analytical solution in Appendix B.	51
3.4	The relative errors E_2 (a) and E_{Nu} (b) for flows through CWT flat channels with different channel height H . The straight lines are liner fittings of the LBM data points (symbols) in the log-log plots, and the line slopes are displayed in the figure labels.	52
3.5	The simulated flow (a and a') and temperature (b and b') fields and transverse velocity and temperature profiles (c and c' for the stream-wise velocity; and d and d' for the temperature) at two locations $x = 0$ and $x = L/2$ for the flows through a wavy channel with Reynolds number $Re = 25$ (a-d) and $Re = 100$ (a'-d').	54
3.6	Distributions of the normalized wall vortex ζ_w and local Nusselt number Nu along the channel wall.	55

- 3.7 Result comparison of the simulations for the cooling process of flow around cylinder with one or two modules included in the simulation domain. In (a) for the temperature field, the color patches are from the two-module simulation, and the isotherm lines are from the one-module simulation. The temperature profiles at $x/L = 0, 3/8, 1,$ and $11/8$ (indicated by labels) are displayed in (b), with the symbols from the one-module calculation and curves from the two-module calculation. 56
- 3.8 Distributions of temperature difference in the left $L \times L$ domain between the one-module and two-module simulations (a), and that between the left ($x \in [0, L]$) and right ($x \in [L, 2L]$) half domain from the two-module simulation (b). In (b) the temperature in the right half domain has been scaled up by a factor of $e^{\lambda L}$ for direct comparison. Panel (c) shows the temperature difference from panels (a) and (b) at two representative x locations. 57
- 3.9 Result comparison of the simulations for the thermal flows around cylinder using the DM or ST approaches for the CWT (a and b) and SHF (a' and b') wall conditions. In the temperature fields (a and a'), the color patches are from the DM approach, and the isotherm lines are from the ST approach. The temperature profiles at $x/L = 0$ and $3/8$ (indicated by labels) are displayed in (b) and (b'), with the symbols from the DM approach and curves from the ST approach. 61
- 3.10 Distributions of temperature difference between simulations using the ST and DM approaches for the CWT (a and b) and SHF (a' and b') wall conditions. The temperature difference from panels (a) and (a') at two representative locations $x/L = 0$ (black solid line) and $3/8$ (blue dashed line) are shown in (c). 62
- 4.1 Schematic illustration of (a) an anisotropic flow system and (b) the transformed system with an approximate spatial isotropy. 66

4.2	Simulated velocities for the straight channel flow using our rectangular LBM model with different a_y values. For comparison, the theoretical profile from fluid mechanics is also displayed as the solid line. The inset enlarges the results near the channel centerline for a better comparison of the calculated and theoretical velocities.	69
4.3	Comparisons of the simulated and analytical velocity distributions (velocity u in a and velocity v in b) for the Taylor-Green vortex flow with $L_x = 100$ and $L_y = 50$. The background color patches are from our LBM calculation and the black contour lines are from the analytical solution Eqs. (4.12-4.13).	70
4.4	Comparisons of the simulated (symbols) and analytical (lines) velocity profiles (velocity u in a and velocity v in b) at $t = T_d/2, T_d$, and $2T_d$ along the vertical line $x = 0.125L_x$ for the Taylor-Green vortex flow.	71
4.5	Comparisons of the simulated (symbols) and analytical (lines) velocities (black for u and blue for v) at two locations ($0.125L_x, 0.125L_y$) (circles) and ($0.125L_x, 0.475L_y$) (squares) for the Taylor-Green vortex flow.	72
4.6	The velocity relative errors for the Taylor-Green vortex flow simulations with different aspect ratios and lattice mesh resolutions. The solid black line is plotted to indicate the second order convergence rate of our method.	72
4.7	Comparisons of (a) pressure distributions and (b) streamlines for the wavy channel flow from (top) the fine mesh LBM simulation over square lattice grids and (b) the $a_y = 0.75$ simulation using our rectangular model.	73
4.8	Comparisons of simulated velocity profiles for the wavy channel flow from our rectangular LBM model (symbols) and the fine mesh general LBM method (solid lines) at three streamwise locations. The inset in each panel enlarges the curve and symbols in the maximum velocity region near the centerline $y = 0$ for a better comparison.	74

- 4.9 Comparisons of (a) pressure distributions and (b) streamlines for the flow through the elliptical particle array from (top) the fine mesh LBM simulation over square lattice grids and (b) the $a_y = 0.758$ simulation using our rectangular model. 75
- 4.10 Comparisons of simulated velocity profiles for the elliptical particle array flow from our rectangular LBM model (symbols) and the fine mesh general LBM method (solid lines) at three streamwise locations. The inset in each panel enlarges the curve and symbols in the maximum velocity region near the top domain edge $y/L = 0.25$ for a better comparison. 77

Chapter 1

Introduction

Fluid flows and associated heat and mass transport processes are important in numerous natural and industrial systems. For example, in steam power plant, cooling waters flow through the condenser to remove the heat from steam as it condenses to liquid water [45, 71]. Also, in the air conditioning system, heat is added or removed to achieve the desired air temperature [45]. Moreover, in microelectronic devices, the heat generated from electronic units needs to be taken away to prevent overheat of the unit, and fans are often used to create airflow in such devices [45]. To improve heat transfer efficiency, water-cooled computers are available for high-performance systems.

The flow and heat transfer in such systems are governed by several differential equations, which are derived from the fundamental conservation of mass, momentum, and energy. Due to the complexity of these nonlinear second order partial differential equations, exact solutions are rare and limited to few simple situations [32, 63]. With the advances in computer technologies, numerical modeling and simulations have become more and more useful for studying complex systems. The advantages of computational simulations include, for example, the low cost and high efficiency, the ability to provide detailed information, and the easiness for parametric investigations [32, 63].

For the flow and heat systems, the governing equations, which are established from the fundamental conservation principles of mass, momentum, and energy, need to be solved simultaneously. Several numerical schemes have been developed, such

as the finite element (FE), finite volume (FV) and finite difference (FD) methods. Details of such methods can be found in computational fluid dynamics (CFD) textbooks [32]. Although these methods are capable in the simulation of various kinds of complex fluid systems, some difficulties still exist. For example, one major step in the finite difference and finite volume method is the meshing process, which divides the continuous physical domain into the discrete computational domain. However, the meshing process often takes a significant amount of computation, and has a substantial impact on the stability of the simulation [32], which is often considered as a negative factor.

In the late 1980s, a novel approach, the lattice Boltzmann method (LBM), was proposed to solve the continuity and momentum equations for incompressible flows [22, 37, 62, 87]. Different from other traditional CFD methods, LBM models the fluid as fictitious particles using the density distribution function from statistical physics, and such particle distribution functions undergo consecutive propagation and collision processes over a discrete lattice space [37, 62]. While the fundamental equations in LBM were developed based on the Boltzmann equation and the Maxwell distribution in statistical physics, the macroscopic continuity and momentum equations can be obtained via the Chapman-Enskog analysis [7, 37, 62]; this justifies the appropriateness for using LBM for flow simulations.

From the practical aspect, the LBM has a simple algorithm and can work with complex boundary geometry and moving boundaries. Parallel computation can also be efficiently implemented due to the locality of LBM algorithms [37, 62]. In addition, the particulate representation in LBM provides the convenience to incorporate microscopic effects in macroscopic flows as in multiphase flows [41] and microscopic gas flows [83]. For these reasons, over the past three decades, the basic LBM algorithm for incompressible flows has been extended to other more complicated situations, such as porous flows, non-Newtonian flows, compressible flows, turbulent flows, particulate flows, heat and mass transfer, chemical reaction flows, and electrohydrodynamics and magnetohydrodynamics systems [18, 33, 37, 79].

As with other numerical schemes, boundary treatments are crucial for the efficient

and accuracy of LBM simulations. In addition, due to the isotropy requirement for the lattice structures (hexagonal or square in two-dimensional space or cubic in three-dimensional space), LBM cannot incorporate the anisotropic features of flows (for example, flows through channels or in cavities with large aspect ratios) naturally as the other CFD methods do. A uniform lattice mesh is needed, and this affects the LBM calculation efficiency.

This thesis summarizes the research work on LBM model developments during my Master's program. Chapter 2 presents an extension of the counter-extrapolation treatment for the conjugate interfaces in heat transfer systems with interface discontinuity [70]. The method can be applied universally on CFD methods, including the LBM, to solve the heat and mass transfer problems with interface discontinuity. The method provides a solution for the simulation of thermal contact resistance phenomenon, which may affect the thermal efficiency of power engines dramatically. In Chapter 3, the inlet-outlet treatments for LBM simulations of periodic thermal flows are described [68]. Several validation and demonstration simulations are performed to illustrate the correctness, accuracy, and usefulness of our proposed methods in LBM simulations of periodic incompressible thermal flows. In Chapter 4, an LBM model for anisotropic flows based on coordinate and velocity transforms is proposed with several demonstration examples [69]. Although as the numerical results show, the method suffers numerical instability and inaccuracy, but it provides an alternative approach for anisotropic flows which doesn't tune the lattice Boltzmann algorithm. All of the above results have been published in peer-reviewed journals.

In addition to those results in Chapters 2–4, the author has worked on the development of a simulation platform for the blood flows in coronary arteries. The open-source LBM package Palabos (<http://www.palabos.org/>) has been employed, and several validations and demonstration calculations have been performed. We are ready to conduct realistic, patient-specific simulations once the clinic data (artery geometry, blood properties, and artery pressure or velocity measurements) are available. The details of this platform development have been described in a project report to the supporter of this project; however, they are not included in this thesis for

the lack of theoretical contributions to the fluid flow.

Chapter 2

Heat and Mass Transfer Between Discontinuous Conjugate Interfaces ¹

2.1 Introduction

Conjugate heat and mass transfer between two media with different transport properties can be found in many natural, biological, and industrial systems [4, 26, 34, 48, 58, 60]. Across a conjugate interface, the heat or mass flux should be continuous due to the energy or mass conservation principle, except some less common situations with chemical reactions on the interface [8, 9, 14, 29, 35]. The transport scalar (temperature or mass concentration) is typically assumed to be continuous across the interface; however, systems with appreciable jump in the transport scalar are also frequently encountered. For example, the contact thermal resistance may cause a temperature discontinuity for heat transfer across a solid-solid interface due to the surface roughness [26]. Similarly, an insulation layer on the surface of an object immersed in a fluid can also generate a temperature difference on the two sides of the insulation layer. Moreover, thermal resistance across a solid-liquid or even a liquid-liquid interface could also play significant roles in microscopic transport systems [42, 52]. For solute transport through a permeable membrane in biological

¹The contents in this Chapter had been published in *International Journal of Numerical Methods for Heat and Fluid Flow*(27: 2231–2258, 2017). Minor revisions have been made in this Chapter.

systems, the solute concentration difference across the membrane is also associated to the solute flux [4, 60].

In recent years, the lattice Boltzmann method (LBM) has become a useful choice for computational simulations of various flow and transport systems, including convection-diffusion systems for heat and mass transfer [3, 13, 17, 78]. Compared to other conventional numerical methods, LBM is advantageous in parallel computation and treating complex boundary geometry. Several LBM conjugate models have been proposed in the literature [27, 38, 43, 44, 56]. For example, Huang and Wu [28] and Chen et al. [12] utilized the total enthalpy LBM model to simulate the heat transfer process in heterogeneous media. The different thermal conductivity and thermal capacity values of different materials/phases can be conveniently incorporated in the equilibrium distribution. On the other hand, Yoshida et al. [76] employed variable weight coefficients in the equilibrium distribution expression to account different thermal transport coefficients across an interface and scaled the density distributions when they cross the interface according to the thermal capacities of respective domains. Furthermore, Karani and Huber [36] adopted an artificial source term to the diffusion equation to recover the thermal conduction equation. The source term requires the calculation of the spatial gradient of the reciprocal of the volume thermal capacity, and they have assumed that the interface locates halfway along the intersecting lattice links. The spatial accuracy in most of these studies [12, 27, 28, 36, 43, 44, 56, 76] is limited to the lattice resolution since the exact boundary location is not considered. Moreover, the interfacial discontinuity has not been addressed in all these previous publications.

Recently, Guo et al. [16] extended their previous work [40] to the jump condition, where the discontinuity terms for both the transport scalar and its transport flux have been considered. In this model, these discontinuity terms are predefined before the simulation, while actually they should be determined simultaneously from the current, local transport scalar field: the jump in transport scalar is typically assumed proportional to the local flux (see Eq.2.2 below), and the jump in transport flux should be related to chemical reaction rate on the interface. In addition, the

mathematical formulation in Ref. [16] is relatively complicated even for the simplest D2Q5 (two-dimensional, five lattice velocities) lattice model. The method and formulation in Ref. [16] are limited to the D2Q5 lattice model; and they are difficult to be applied to other lattice structures and cannot be utilized for other numerical methods. Moreover, the general algorithm (Eq.15 in [16]) cannot be applied at the vicinity where the lattice lines intersect the interface perpendicularly (for example, the very top/bottom/left/right edge of a particle in the D2Q5 lattice domain. See Fig. 1 in Ref. [16]). Special treatments (for example, switching to the decoupled scheme Eq.22 in Ref. [16]) could be adopted to bypass this problem; however, this will make the interface method less efficient and less consistent.

In this chapter, the counter-extrapolation LBM method for conjugate interfaces recently developed by Le et al. [38] has been extended to include the interface discontinuity. By extrapolating the transport scalar distribution from each domain toward of the interface in the normal direction with the conjugate interface requirements properly considered, the transport scalar values on the both sides of interface are able to be determined. Once the scalar values on the interface are available, the conjugate system has been transferred into a Dirichlet boundary problem for each domain, and appropriate Dirichlet boundary methods can be readily applied. Compared to the method in Ref. [16], our method appears advantageous in terms of the mathematical clarity and algorithm simplicity. The transport scalar jump across the interface is related to the local flux via the interfacial resistance, following the typical treatments for heat and mass transfer systems [26, 60]. For the rarity of interfacial reactions in typical heat or mass transfer systems, the discontinuity in transport flux have not been considered. Validation simulations are performed to examine the correctness and accuracy of our model by comparing LBM results to analytical solutions for steady and unsteady systems with flat and curved interfaces. Numerical stability has also been tested with satisfactory results. The cooling processes of a hot cylinder in a cold flow under different surface insulation conditions are also presented as a demonstration example for the potential usefulness of our model. The model

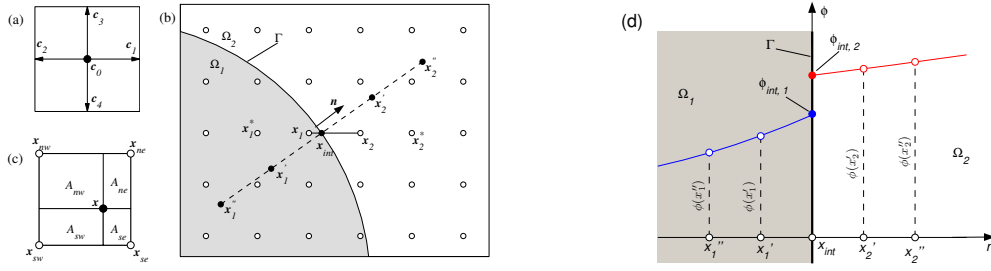


FIGURE 2.1: Schematic illustrations for method description: (a) the D2Q5 lattice structure, (b) the counter-extrapolation method for conjugate interfaces, (c) the bilinear interpolation operation for estimating the property at an arbitrary position x from its four neighboring lattice nodes, and (d) the ϕ distribution profile with discontinuity across the interface along the normal direction.

description and simulations are presented using the D2Q5 lattice structure for simplicity; however, the interface treatment described here can be readily applied to other lattice structures and even other numerical methods (such as finite-difference method and finite-volume method) of computational heat and mass transfer. Also implementing a flux jump according to the interfacial chemical reactions is straightforward by following the algorithm outline in this work.

2.2 Theory and Methods

Here, the fundamentals and numerical models used in this study will be summarized. Section 2.2.1 briefly outlines the transport equation and the conjugate condition across an interface between two transport media, and Section 2.2.2 describes the D2Q5 LBM model for the convection-diffusion equation. These materials are available in the literature; however, they are included here for the completeness of this chapter. Section 2.2.3 extends the recent conjugate method by Le et al. [38] to consider the discontinuity in transport scalar to the simultaneous local flux. A boundary method for the Dirichlet condition is also required and here we adopt the midpoint bounce-back method [75]. In addition to the formulations presented here, when fluid flows are involved, an appropriate flow solver is also necessary.

2.2.1 Governing Equations and Conjugate Interface Condition

Considering an interface Γ separating two domains Ω_1 and Ω_2 with different transport parameters. The spatial distribution and temporal evolution of a transport scalar property ϕ (ϕ can be taken as the temperature T for heat transfer or the concentration C for mass transfer) is governed by the following differential convection-diffusion equation:

$$\begin{aligned}\partial\phi/\partial t + \mathbf{u} \cdot \nabla\phi &= D_1\nabla^2\phi + G, & \text{in } \Omega_1; \\ \partial\phi/\partial t + \mathbf{u} \cdot \nabla\phi &= D_2\nabla^2\phi + G, & \text{in } \Omega_2.\end{aligned}\quad (2.1)$$

Here t is time, \mathbf{u} is the velocity, G is the source term, and D_1 and D_2 are the transport diffusivities in domains Ω_1 and Ω_2 , respectively. At the conjugate interface Γ , the discontinuity in transport scalar ϕ can be related to the transport flux q_n along the normal direction \mathbf{n} as [26, 60]

$$C_i(\phi_{int,1} - \phi_{int,2}) = q_n, \quad (2.2)$$

and the normal flux q_n is given by

$$q_n = -\beta_1 D_1 (\partial\phi/\partial n)_{int,1} = -\beta_2 D_2 (\partial\phi/\partial n)_{int,2}. \quad (2.3)$$

Here C_i can be considered as the thermal interface conductance for heat transfer, or the membrane permeability for solute transport across a membrane in industrial or biological systems. The inverse $1/C_i$ is usually called the contact thermal resistance in heat transfer. The parameter β is simply 1 for mass transfer and it is the volumetric heat capacity ρc_p (ρ as the mass density and c_p as the regular heat capacity) for heat transfer. The subscript *int* is used to indicate that the variable or its gradient is measured at the interface, and subscripts 1 and 2 denote on which side of the interface or in which domain these properties are considered. $\partial/\partial n$ represents the derivative in the local normal direction \mathbf{n} , pointing from domain Ω_1 toward domain Ω_2 . Following the notations in recent relevant studies [16, 38, 40], Eqs.(2.2) and (2.3)

can be written as follows:

$$\lambda(\phi_{int,1} - \phi_{int,2}) = \frac{q_n}{\beta_1} ; \quad (2.4)$$

$$\frac{q_n}{\beta_1} = -D_1 (\partial\phi/\partial n)_{int,1} = -\sigma D_2 (\partial\phi/\partial n)_{int,2} , \quad (2.5)$$

where $\lambda = C_i/\beta_1$ can still be considered as the interface conductance, and $\sigma = \beta_2/\beta_1$.

2.2.2 LBM Model for Transport Phenomenon

To solve the convection-diffusion equation Eq.(2.1), the multiple-relaxation-time (MRT) LBM model is employed as in Ref. [16, 38, 40]. The distribution function $g_i(\mathbf{x}, t)$ (\mathbf{x} is the lattice node location and the subscript i denotes the lattice direction) evolves according to the following lattice Boltzmann equation:

$$g_i(\mathbf{x} + \mathbf{c}_i\delta t, t + \delta t) - g_i(\mathbf{x}, t) = \Lambda_i + \omega_i G(\mathbf{x}, t)\delta t , \quad (2.6)$$

where δx is the lattice grid size, δt is the time step and Λ_i is the collision operator. For the D2Q5 lattice structure (Fig. 2.1a) employed in this study, the lattice velocity \mathbf{c}_i and lattice weight ω_i are given as: $\mathbf{c}_0 = [0,0]$, $\mathbf{c}_1 = [\delta x/\delta t, 0]$, $\mathbf{c}_2 = [-\delta x/\delta t, 0]$, $\mathbf{c}_3 = [0, \delta x/\delta t]$, $\mathbf{c}_4 = [0, -\delta x/\delta t]$, $\omega_0 = 1/3$, and $\omega_{1-4} = 1/6$. The collision operator Λ_i is usually written in matrix expressions as

$$\Lambda = [\Lambda_0, \Lambda_1, \Lambda_2, \Lambda_3, \Lambda_4]^T = -\mathbf{M}^{-1}\mathbf{S}[\mathbf{m}(\mathbf{x}, t) - \mathbf{m}^{eq}(\mathbf{x}, t)] . \quad (2.7)$$

The superscript T denote the transpose of a vector, and the transformation matrix \mathbf{M} and the relaxation matrix \mathbf{S} for the D2Q5 lattice structure are given as:

$$M = \begin{bmatrix} 1 & 1 & 1 & 1 & 1 \\ 0 & 1 & -1 & 0 & 0 \\ 0 & 0 & 0 & 1 & -1 \\ 4 & -1 & -1 & -1 & -1 \\ 0 & 1 & 1 & -1 & -1 \end{bmatrix}, \quad S = \begin{bmatrix} \tau_0 & 0 & 0 & 0 & 0 \\ 0 & \tau_1 & 0 & 0 & 0 \\ 0 & 0 & \tau_2 & 0 & 0 \\ 0 & 0 & 0 & \tau_3 & 0 \\ 0 & 0 & 0 & 0 & \tau_4 \end{bmatrix}^{-1}. \quad (2.8)$$

For the isotropic diffusion systems concerned in the present study, the elements τ_1 and τ_2 in matrix \mathbf{S} are related to the diffusion coefficients D_1 and D_2 in Eq.(2.1) as

$$\tau_1 = \tau_2 = \begin{cases} \frac{1}{2} + \frac{3D_1\delta t}{(\delta x)^2}, & \text{in } \Omega_1 ; \\ \frac{1}{2} + \frac{3D_2\delta t}{(\delta x)^2}, & \text{in } \Omega_2 . \end{cases} \quad (2.9)$$

The relaxation coefficient τ_0 does not affect the numerical solution, and the components τ_3 and τ_4 have no effect on the leading-order terms in the resulted convection-diffusion equation from the LBM algorithm. The off-diagonal components in the relaxation matrix \mathbf{S} can also be set to non-zero values for anisotropic diffusion systems. In this study, we only consider isotropic situations, and use $\tau_0 = \tau_3 = \tau_4 = 1$. The vector \mathbf{m} in Eq.(2.7) is related to the distribution functions g_i via the transformation matrix \mathbf{M} :

$$\mathbf{m} = [m_0, m_1, m_2, m_3, m_4]^T = \mathbf{M}[g_0, g_1, g_2, g_3, g_4]^T. \quad (2.10)$$

With the equilibrium distribution functions given as

$$g_i^{eq} = \omega_i \phi (1 + 3\mathbf{c}_i \cdot \mathbf{u}), \quad (2.11)$$

and the transport scalar

$$\phi = \sum_i g_i = \sum_i g_i^{eq}, \quad (2.12)$$

it is ready to obtain the following expression for the equilibrium counterpart for vector \mathbf{m} :

$$\mathbf{m}^{eq} = [m_0^{eq}, m_1^{eq}, m_2^{eq}, m_3^{eq}, m_4^{eq}]^T = \mathbf{M}[g_0^{eq}, g_1^{eq}, g_2^{eq}, g_3^{eq}, g_4^{eq}]^T = [\phi, u\phi, v\phi, 2\phi/3, 0]^T, \quad (2.13)$$

where u and v are the components of velocity \mathbf{u} in the x and y directions, respectively.

2.2.3 The Counter-Extrapolation Method

For the convenience of further discussion, the lattice Boltzmann equation Eq.(2.6) is split into two steps: the *collision* step:

$$\bar{g}_i(\mathbf{x}, t) = g_i(\mathbf{x}, t) + \Lambda_i + \omega_i G(\mathbf{x}, t) \delta t; \quad (2.14)$$

and the *propagation* step:

$$g_i(\mathbf{x} + \mathbf{c}_i \delta t, t + \delta t) = \bar{g}_i(\mathbf{x}, t). \quad (2.15)$$

The intermediate distribution function \bar{g}_i is called the post-collision distribution. A general curved interface Γ is considered, which is separating domains Ω_1 and Ω_2 as shown in Fig. 2.1b. At a certain time step t , all the distribution functions g_i at each lattice node are available, and the post-collision distribution functions \bar{g}_i can be calculated from Eq.(2.14). However, the propagation process cannot be performed as usual for lattice links crossing the interface, such as that connecting node \mathbf{x}_1 in domain Ω_1 and node \mathbf{x}_2 in domain Ω_2 (Fig. 2.1b). The intersecting position is labeled as \mathbf{x}_{int} . Following previous studies in dealing with boundary gradients [11, 38, 49], we draw a line at point \mathbf{x}_{int} perpendicular to the interface. On this line we have points \mathbf{x}'_1 and \mathbf{x}''_1 in domain Ω_1 , and points \mathbf{x}'_2 and \mathbf{x}''_2 in domain Ω_2 . The distance between any two adjacent points along the perpendicular line is kept constant δ , i.e., $|\mathbf{x}''_1 - \mathbf{x}'_1| = |\mathbf{x}'_1 - \mathbf{x}_{int}| = |\mathbf{x}_{int} - \mathbf{x}'_2| = |\mathbf{x}'_2 - \mathbf{x}''_2| = \delta$ (Fig. 2.1b). The ϕ values at points $\mathbf{x}''_1, \mathbf{x}'_1, \mathbf{x}'_2,$ and \mathbf{x}''_2 can be obtained from neighboring lattice nodes in their individual

domain via, for example, bilinear interpolations [11]:

$$\phi(\mathbf{x}) \approx \frac{A_{nw}\phi(\mathbf{x}_{se}) + A_{ne}\phi(\mathbf{x}_{sw}) + A_{sw}\phi(\mathbf{x}_{ne}) + A_{se}\phi(\mathbf{x}_{nw})}{(\delta x)^2}, \quad (2.16)$$

where \mathbf{x}_{nw} , \mathbf{x}_{ne} , \mathbf{x}_{sw} , and \mathbf{x}_{se} are the four nearest lattice nodes of position \mathbf{x} , and A_{nw} , A_{ne} , A_{sw} , and A_{se} are the four fractional areas in the lattice square (Fig. 2.1c). By assuming second-order polynomial variations along the perpendicular line in both domains, the normal gradient on each domain side at the intersecting point \mathbf{x}_{int} can be expressed as:

$$(\partial\phi/\partial n)_{int,1} \approx \frac{3\phi_{int,1} - 4\phi(\mathbf{x}'_1) + \phi(\mathbf{x}''_1)}{2\delta}, \quad (2.17)$$

$$(\partial\phi/\partial n)_{int,2} \approx -\frac{3\phi_{int,2} - 4\phi(\mathbf{x}'_2) + \phi(\mathbf{x}''_2)}{2\delta}. \quad (2.18)$$

The conjugate boundary conditions Eqs.(2.4) and (2.5) are then used in combination with Eqs.(2.17) and (2.18) to solve the interface values $\phi_{int,1}$ and $\phi_{int,2}$ (Fig. 2.1d):

$$\phi_{int,1} = \frac{(\alpha + \gamma)[4\phi(\mathbf{x}'_1) - \phi(\mathbf{x}''_1)] + [4\phi(\mathbf{x}'_2) - \phi(\mathbf{x}''_2)]}{3(1 + \alpha + \gamma)}; \quad (2.19)$$

$$\phi_{int,2} = \frac{\gamma[4\phi(\mathbf{x}'_1) - \phi(\mathbf{x}''_1)] + (1 + \alpha)[4\phi(\mathbf{x}'_2) - \phi(\mathbf{x}''_2)]}{3(1 + \alpha + \gamma)}; \quad (2.20)$$

where

$$\alpha = \frac{3D_1}{2\lambda\delta}, \quad \gamma = \frac{D_1}{\sigma D_2}. \quad (2.21)$$

When the interface resistance is negligible, we have the conductance $\lambda \rightarrow \infty$ and thus $\alpha \rightarrow 0$, and the above equations revert back to those in [38]. Once the interface values $\phi_{int,1}$ and $\phi_{int,2}$ become available, the original conjugate interface problem has been converted to a Dirichlet boundary problem for each domain, and an appropriate boundary method for the Dirichlet condition can be used. Here, we adopt

the midpoint bounce-back scheme for its simple algorithm and good numerical accuracy [11]:

$$g_{\bar{i}}(\mathbf{x}_1, t + \delta t) = -\bar{g}_i(\mathbf{x}_1, t) + 2\omega_i\phi_1^m \quad , \quad (2.22)$$

$$g_i(\mathbf{x}_2, t + \delta t) = -\bar{g}_{\bar{i}}(\mathbf{x}_2, t) + 2\omega_{\bar{i}}\phi_2^m \quad . \quad (2.23)$$

Here the lattice direction i is from node \mathbf{x}_1 to node \mathbf{x}_2 and the lattice direction \bar{i} is the reverse direction. For the particular situation in Fig. 2.1b, we have $i = 1$ and $\bar{i} = 2$. Parameters ϕ_1^m and ϕ_2^m are the estimated ϕ values at the midpoint $\mathbf{x}^m = (\mathbf{x}_1 + \mathbf{x}_2)/2$ via interpolation or extrapolation from each domain side, respectively [11, 75]:

$$\phi_1^m = \begin{cases} \frac{\phi_{int, 1} + (1-2\Delta)\phi(\mathbf{x}_1)}{2(1-\Delta)} \quad , \Delta \leq 1/2 \quad , \\ \frac{3\phi_{int, 1} - (2\Delta-1)\phi(\mathbf{x}_1^*)}{2(2-\Delta)} \quad , \Delta > 1/2 \quad , \end{cases} \quad (2.24)$$

$$\phi_2^m = \begin{cases} \frac{\phi_{int, 2} - (1-2\Delta)\phi(\mathbf{x}_2)}{2\Delta} \quad , \Delta \leq 1/2 \quad , \\ \frac{3\phi_{int, 2} - (1-2\Delta)\phi(\mathbf{x}_2^*)}{2(1-\Delta)} \quad , \Delta > 1/2 \quad . \end{cases} \quad (2.25)$$

In these equations, \mathbf{x}_1^* and \mathbf{x}_2^* are the second lattice nodes along the intersecting lattice link from the interface into each domain, and Δ is the fraction in domain Ω_1 of the lattice link connecting \mathbf{x}_1 and \mathbf{x}_2 (Fig. 2.1b):

$$\Delta = \frac{|\mathbf{x}_{int} - \mathbf{x}_1|}{|\mathbf{x}_2 - \mathbf{x}_1|} \quad . \quad (2.26)$$

The counter-extrapolation method described above performs extrapolations of ϕ along the local normal direction of the conjugate interface. With a properly selected extrapolation interval δ ($\delta = 1.5\delta x$ in this study) [11, 49], all the extrapolation control points \mathbf{x}_1'' , \mathbf{x}_1' , \mathbf{x}_2' , and \mathbf{x}_2'' are well defined in their respective domains; unless the local curvature radius is very small (for example, a circular interface with a radius $R < 2\delta x$), and such situation should be avoided anyway for the low spatial resolution.

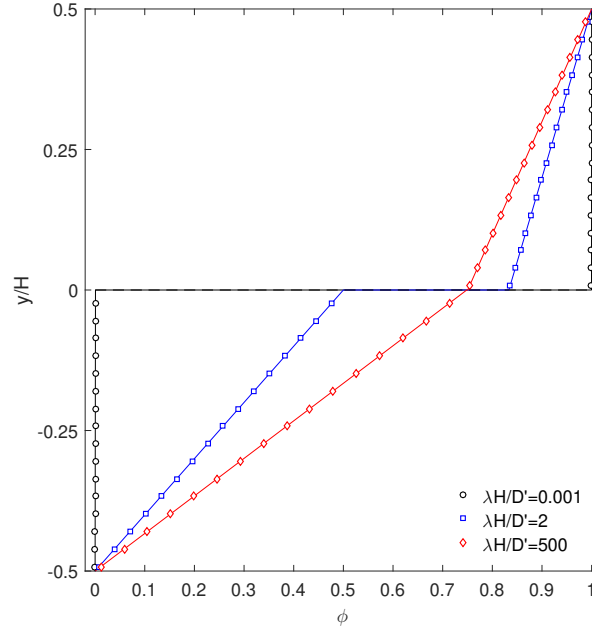


FIGURE 2.2: Effects of the interface conductance on the ϕ profile across the gap between two parallel plates. The interface locates at $y = H/2$. The LBM results are displayed as symbols in comparison to the corresponding theoretical solutions from Eq.(2.27) as solid lines.

2.3 Validation and Demonstration Simulations

We start with a very simple one-dimensional (1D) system to demonstrate that the jump condition at interface has been well represented in our model. After that, several more complicated simulations are presented to examine the performance of the proposed method. These simulations are similar to those in previous studies [16, 38, 40], and they cover steady and unsteady situations with flat and curved interfaces. We also simulate the cooling process of a hot cylinder in a cold flow under different surface insulation conditions as a demonstration example to illustrate potential applications of our conjugate interface treatment.

2.3.1 One-Dimensional Steady Diffusion System

Here we consider the steady diffusion system between two infinitely large, parallel plates with a gap H , and the conjugate interface locates at the center plane $y = H/2$ (y is the coordinate across the gap starting from one plate). We consider the region $0 < y < H/2$ as Domain 1 and the region $H/2 < y < H$ as Domain 2. For simplicity,

the boundary values on the plates are set as $\phi(y = 0) = 0$ and $\phi(y = H) = 1$. The theoretical solution of ϕ in this system is

$$\phi(y) = \begin{cases} \frac{2y}{H+HD_1/(\sigma D_2)+2D_1/\lambda}, & 0 < y \leq H/2, \\ 1 - \frac{2(1-y)}{H+H\sigma D_2/D_1+2\sigma D_2/\lambda}, & H/2 \leq y < H, \end{cases} \quad (2.27)$$

and the interfacial values $\phi_{int,1}$ and $\phi_{int,2}$ can be easily obtained by letting $y = H/2$ in the two respective expressions in the above equation. Here we use $H = 64$, $\sigma = 1$, $D_1 = 1/18$, $D_2 = 1/6$, and the interface (as well as the boundary plates) locates half-way between two horizontal lattice grid lines. The LBM calculations are performed over a rectangular domain with the periodic boundary condition in the direction along the plates. Various interfacial conductance parameter λ values have been tested; and Fig. 2.2 displays three representative cases. The case with $\lambda H/D' = 0.001$ [$D' = D_1 D_2 / (D_1 + D_2)$] has a relatively low interface conductance (i.e., high interface resistance), and the interface acts like an insulation layer between the two domains. As the result, we have almost uniform ϕ values in each domain: $\phi = 0$ in Domain 1 and $\phi = 1$ in Domain 2, determined by the respective wall boundary values. On the other extreme end, the case with $\lambda H/D' = 500$ represents the situation with an interface of a good conductance or very low interface resistance, and therefore virtually there is no ϕ discontinuity observed at the interface. The case of $\lambda H/D' = 2$ is presented here just to illustrate the intermediate situations between those two extreme conditions above. In all these cases, the LBM results (symbols) match their corresponding exact solutions from Eq.(2.27) perfectly with no visual difference. Other diffusivity (D_1 and D_2) and interface-lattice offset (Δ) values have also been tested, and similar excellent agreement has been observed. Numerically, the difference between LBM and theoretical results is of the order of $\sim 10^{-10}$. We believe these tiny errors are mainly from the computer round-off errors, since all our assumptions (including the bilinear interpolations via Eq.2.16 and the second-order finite-difference approximation of interface gradient via Eqs.(2.17) and (2.18) are exactly satisfied, and the LBM algorithm for the convection-diffusion equation has a second-order accuracy (while the ϕ distribution is linear in this 1D diffusion system).

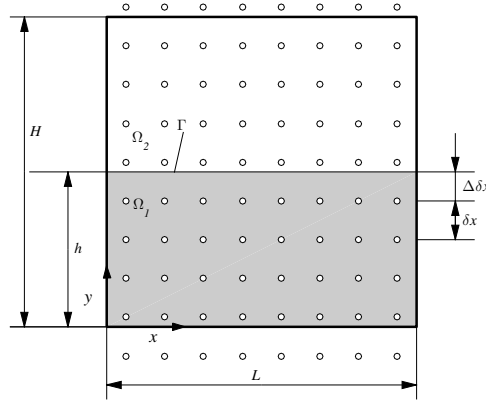


FIGURE 2.3: The schematic for the flat interface system used in steady and unsteady convection-diffusion simulations. The relative position of the interface to the underlying lattice grid is denoted the offset Δ , the distance from the interface to the first lattice grid line below it.

2.3.2 Steady and Unsteady Convection-Diffusion Processes with a Flat Interface

Model Description and Analytical Solution

Next we consider the system shown in Fig. 2.3 with a flat, horizontal interface. In this study, we limit ourselves to square systems with the interface in the middle, i.e., $L = H$ and $h = H/2$. The relative position of the interface to the underlying lattice mesh lines is represented by the interface-lattice offset Δ . The variable ϕ values at the top and bottom walls are specified by:

$$\phi(x, y = 0) = \phi(x, y = H) = \cos(kx + \omega t) , \quad (2.28)$$

where $k = 2\pi/L$ is the wavenumber and ω is the temporal frequency. This system has been simulated in Refs. [38, 40] with no interface discontinuity considered; and it has also been utilized in Ref. [16] with predefined interface jumps in transport scalar and flux. Here we will apply the classical conjugate condition Eqs.(2.4) and (2.5) instead.

The midpoint bounce-back boundary method [11] is utilized for this Dirichlet boundary problem for each domain, and periodic boundary conditions [78] are implemented at the left and right boundaries. In addition, a uniform flow $\mathbf{u} = (U_0, 0)$ (U_0 is a constant) is applied over the entire computational domain. The analytical

solution of this system is:

$$\phi_{ex}(x, y, t) = \begin{cases} \text{Re}\{e^{i(kx+\omega t)}[\gamma_1 e^{-\lambda_1 y} + (1 - \gamma_1)e^{\lambda_1 y}]\}, & 0 \leq y \leq h ; \\ \text{Re}\{e^{i(kx+\omega t)}[\gamma_2 e^{-\lambda_2 y} + (1 - \gamma_2)e^{-\lambda_2 H}e^{-\lambda_2(H-y)}]\}, & h \leq y \leq H ; \end{cases} \quad (2.29)$$

with relevant parameters defined as below:

$$\gamma_1 = \frac{\lambda_1(a_3^2 - a_2^2) + \kappa\sigma\lambda_2(2a_1a_2a_3 - a_2^2 - a_3^2) + \kappa\sigma\lambda_1\lambda_2D_1(a_2^2 + a_3^2)/\lambda}{(\lambda_1 + \kappa\sigma\lambda_2)(a_1^2a_3^2 - a_2^2) - (\lambda_1 - \kappa\sigma\lambda_2)(a_1^2a_2^2 - a_3^2) + \kappa\sigma\lambda_1\lambda_2D_1(a_1^2 + 1)(a_2^2 + a_3^2)/\lambda} , \quad (2.30)$$

$$\gamma_2 = \frac{\lambda_1(a_1^2a_3 + a_3 - 2a_1a_2) + \kappa\sigma\lambda_2(a_1^2 - 1)a_3 + \kappa\sigma\lambda_1\lambda_2D_1(a_1^2 + 1)a_3/\lambda}{(\lambda_1 + \kappa\sigma\lambda_2)(a_1^2a_3^2 - a_2^2) - (\lambda_1 - \kappa\sigma\lambda_2)(a_1^2a_2^2 - a_3^2) + \kappa\sigma\lambda_1\lambda_2D_1(a_1^2 + 1)(a_2^2 + a_3^2)/\lambda} , \quad (2.31)$$

$$a_1 = e^{-\lambda_1 h} , \quad a_2 = e^{-\lambda_2 h} , \quad a_3 = e^{-\lambda_2 H} , \quad (2.32)$$

$$\lambda_1 = k\sqrt{1 + i\frac{\omega + kU_0}{k^2D_1}} , \quad \lambda_2 = k\sqrt{1 + i\frac{\omega + kU_0}{k^2D_2}} , \quad \kappa = D_2/D_1 . \quad (2.33)$$

Again, with $\lambda \rightarrow \infty$ for negligible interfacial resistance, the last terms in the numerators and denominators in Eqs.(2.30) and (2.31) disappear and the solution reverts back to that in Refs. [38, 40].

Steady Simulation

By setting $\omega = 0$, the temporal vibrational effect can be removed, and the system becomes steady. Here, following Refs. [38, 40], we use $D_1 = 1/60$, $D_2 = 1/6$, $\sigma = 1$, and the Peclet number $Pe = U_0H/D_1 = 20$ for the steady simulation. A moderate interface conductance $\lambda H/D' = 2$ is selected based on the simulations in Sect. 2.3.1. Fig. 2.4 compares the LBM results to those from Eq.(2.29) for the case with $H = 64$ and the interface-lattice offset $\Delta = 0.5\delta x$. In Fig. 2.4a, we plot the ϕ distributions from our LBM calculation (the background color patches) and the analytical solution Eq.(2.29) (the black lines as iso- ϕ contours). Here we have a visually perfect match in the contours. Actually if we plot the LBM and theoretical results both in contour lines, we will not be able to distinguish them from each other. For a more quantitative comparison, Fig. 2.4b displays the ϕ distribution profiles along four constant- x lattice lines, with the symbols from our LBM simulation and the curves

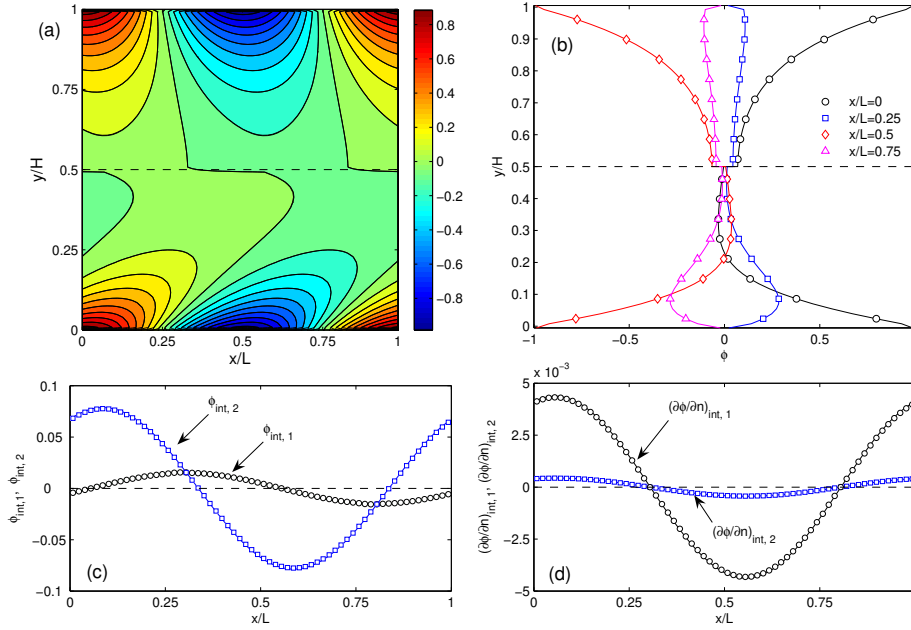


FIGURE 2.4: The ϕ distributions in the computational domain (a), the ϕ profiles along $x/L = 0, 0.25, 0.5$, and 0.75 across the interface at $y/H = 0.5$ (b), the variations of interfacial values $\phi_{int,1}$ and $\phi_{int,2}$ along the interface (c), and the variations of the interfacial gradients $(\partial\phi/\partial n)_{int,1}$ and $(\partial\phi/\partial n)_{int,2}$ along the interface (d) for the steady convection-diffusion system with a flat interface. In (a) the background color patches are from our LBM calculation and the black contour lines are from the analytical solution. In (b)-(d) the symbols are LBM results and the underlying curves are theoretical predictions. The dashed lines in (a) and (b) indicate the interface location; and the dashed lines in (c) and (d) are used to separate the positive and negative scalar or gradient values along the interface.

from Eq.(2.29). Again excellent agreement is observed here, both in the individual domains and across the interface.

To check the model performance along the interface, we plot the transport values and gradients on both sides of the interface in Figs. 2.4c and d. We see $\phi_{int,1} > \phi_{int,2}$ in the range of $0.305 < x/L < 0.805$, and $\phi_{int,1} < \phi_{int,2}$ in the rest (Fig. 2.4c); correspondingly, the interfacial gradients $(\partial\phi/\partial n)_{int,1}$ and $(\partial\phi/\partial n)_{int,2}$ are both positive (i.e., flux from Domain 1 into Domain 2) in $0.305 < x/L < 0.805$, and they are both negative (i.e., flux from Domain 2 into Domain 1) in the rest of the interface (Fig. 2.4d). At the separating locations $x/L = 0.305$ and $x/L = 0.805$, $\phi_{int,1} = \phi_{int,2}$ as well as $(\partial\phi/\partial n)_{int,1} = (\partial\phi/\partial n)_{int,2} = 0$. The two gradients follow the same variation fashion along the interface, and the magnitude of $(\partial\phi/\partial n)_{int,1}$ is away larger that of $(\partial\phi/\partial n)_{int,2}$, since we have used $D_1 = 1/60$ and $D_2 = 1/6$ in

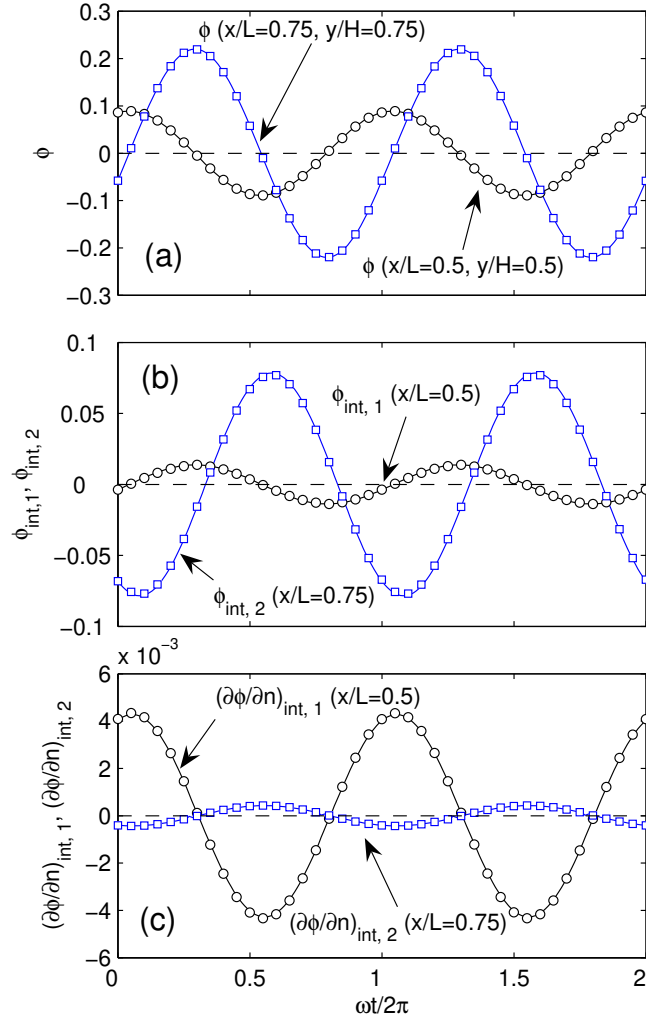


FIGURE 2.5: The variations of the ϕ values in separate domains (a) and the interfacial scalar (b) and gradient (c) values with simulation time for the unsteady convection-diffusion system with a flat interface. The symbols are LBM results and the underlying curves are from analytical solution Eq.(2.29).

this calculation. This shows the conjugate requirements Eqs.(2.4) and (2.5) have been correctly considered in our algorithm. Also plotted there are the theoretical solutions calculated from Eq.(2.29). The agreement is excellent in both interface value and gradient.

Unsteady Simulation

We continue to examine the performance of our counter-extrapolation method in dealing with unsteady problems. The system in Fig. 2.3 is re-utilized, however, with a dynamic boundary condition. The frequency ω in Eq.(2.28) is set from the Stokes

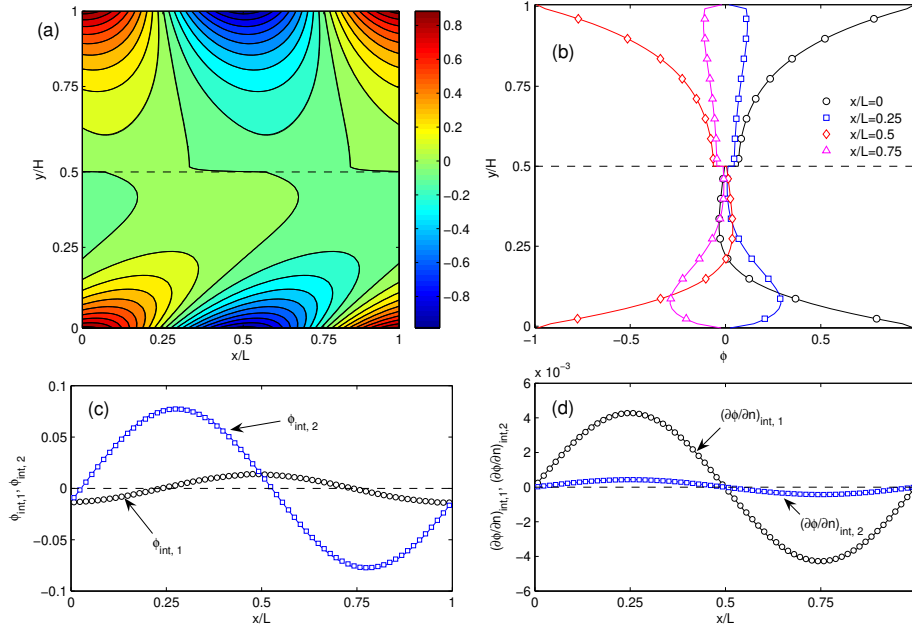


FIGURE 2.6: The ϕ distributions (a), the ϕ profiles along $x/L = 0, 0.25, 0.5$, and 0.75 (b), the variations of interfacial values $\phi_{int,1}$ and $\phi_{int,2}$ along the interface (c), and the variations of interfacial gradients $(\partial\phi/\partial n)_{int,1}$ and $(\partial\phi/\partial n)_{int,2}$ along the interface (d) for the unsteady convection-diffusion system with a flat interface at $t = 4\pi/\omega$. In (a) the background color patches are from our LBM calculation and the black contour lines are from the analytical solution. In (b)-(d) the symbols are LBM results and the underlying curves are theoretical predictions. The dashed lines in (a) and (b) indicate the interface location; and those in (c) and (d) are used to separate the positive and negative scalar and gradient values.

number $St = \sqrt{\frac{H^2\omega}{2\pi D_1}} = 1$ [38, 40]. The ratio σ is set to 10 to represent more general cases, for example, the heat transfer between two media with different volumetric heat capacities. All other parameters are kept the same as in the previous steady case. The simulation starts with the theoretical solution from Eq.(2.29) as the initial condition. We record the ϕ values at two locations away from the interface and boundaries (one at $x/L = y/H = 0.25$ in Domain 1, and another at $x/L = y/H = 0.75$ in Domain 2), and the ϕ values and its gradients on two interfacial locations [$\phi_{int,1}$ and $(\partial\phi/\partial n)_{int,1}$ at $x/L = 0.5$; $\phi_{int,2}$ and $(\partial\phi/\partial n)_{int,2}$ at $x/L = 0.75$]. Their revolutions with simulation time (normalized by the variation period $2\pi/\omega$) are displayed in Fig. 2.5. It can be seen there all recorded variables (symbols) follow their individual analytical solutions (curves) very well with no evident deviations. Please note that here the interface values and gradients on side 1 and side 2 are

obtained at different locations on the interface, and the correlations discussed for Fig. 2.4 do not apply here. Also, as for the steady case, we compare the overall ϕ distributions (Fig. 2.6a), the ϕ profiles along constant- x lattice lines (Fig. 2.6b), and the ϕ and its gradient variations along the interface (Figs. 2.6c and d) at time instant $t = 4\pi/\omega$ (i.e., two periods after the simulation starts). In general, good agreement between the LBM results and the exact solutions is confirmed.

The numerical stability of this conjugate method is then tested using this unsteady system. For this purpose, we start with the same parameters as given above, and change one individual parameter significantly to see if the calculation is stable or not. Here are the parameters and their values we have examined:

- Diffusivity: $D_1 = 1/1000$ and $D_2 = 1$; and $D_1 = 1$ and $D_2 = 1000$.
- Heat capacity ratio: $\sigma = 1/100$; and $\sigma = 100$.
- Interface conductance: $\lambda = 1/1000$; and $\lambda = 1000$.
- The Peclet number: $Pe = 200$.

All these calculations are stable for at least three periods. The only case that the simulation becomes unstable is when we increase the Stokes number $St = \sqrt{\frac{H^2\omega}{2\pi D_1}}$. The program works well till $St = 40$, and it turns unstable at $St = 50$. At $St = 40$, the temporal variation period $2\pi/\omega$ is $153.6\delta t$. Further increasing the Stokes number St with other parameters the same will increase the frequency ω and reduce the variation period $2\pi/\omega$ at a two-order faster speed. Such faster variations in temperature can cause strong numerical oscillation and break down the simulation. In addition, at a high frequency, the temperature variation is limited in a thin layer near the top and bottom boundaries, while the temperature in the central region remains approximately zero unchanged. A large spatial temperature gradient in the y -direction is then developed near the boundaries, and this can also damage the simulation stability. Overall, the stability of our method is satisfactory considering the large ranges of parameter values tested.

2.3.3 Steady Diffusion System with a Circular Interface

For a more general case, we now consider the diffusion system illustrated in Fig. 2.7, with Domain 1 in the central region of $r < R_1$ and Domain 2 in the surrounding ring region of $R_1 < r < R_2$. For this case, only the steady situation is simulated and the boundary ϕ value on the outer edge $r = R_2$ is specified by [38, 40]:

$$\phi(r = R_2) = \cos(n\theta) \quad , \quad (2.34)$$

where θ is the polar angle and n is an integer. The analytical solution of this system is given by:

$$\phi(r, \theta) = \begin{cases} b_1 r^n \cos(n\theta) \quad , \quad 0 \leq r \leq R_1 \quad , \\ (b_2 r^n + b_3 r^{-n}) \cos(n\theta) \quad , \quad R_1 \leq r \leq R_2 \quad , \end{cases} \quad (2.35)$$

and the parameters b_1 , b_2 , and b_3 are expressed as:

$$\begin{aligned} b_1 &= \frac{2\kappa\sigma R_1 R_2^{-n}}{(\kappa\sigma + 1)R_1 R_2^{2n} + (\kappa\sigma - 1)R_1^{2n+1} - n\kappa\sigma D_1(R_1^{2n} + R_2^{2n})/\lambda} \quad , \\ b_2 &= \frac{[(\kappa\sigma + 1)R_1 + n\kappa\sigma D_1/\lambda]R_2^n}{(\kappa\sigma + 1)R_1 R_2^{2n} + (\kappa\sigma - 1)R_1^{2n+1} - n\kappa\sigma D_1(R_1^{2n} + R_2^{2n})/\lambda} \quad , \\ b_3 &= \frac{[(\kappa\sigma - 1)R_1 + n\kappa\sigma D_1 - 1/\lambda]R_1^{2n} R_2^n}{(\kappa\sigma + 1)R_1 R_2^{2n} + (\kappa\sigma - 1)R_1^{2n+1} - n\kappa\sigma D_1(R_1^{2n} + R_2^{2n})/\lambda} \quad . \end{aligned} \quad (2.36)$$

Once again, for a no-resistance interface with $\lambda \rightarrow \infty$, the expressions for b_1 , b_2 , and b_3 reduce to the simpler version in Refs. [38, 40]. In our simulations, we maintain $n = 4$, $R_2/R_1 = 2$, $D_1 = 1/60$, $D_2 = 1/6$, and $\sigma = 1$, following previous studies [38, 40]. The interface conductance is set as $\lambda R_2/D' = 2$.

In Fig. 2.8, the LBM results for the case with $R_2 = 2R_1 = 32.5\delta x$ [38, 40] are compared to the exact solution in Eq.(2.35). Similar to Figs. 2.4 and 2.6, here we display the ϕ distribution contours (Fig. 2.8a; only a quarter of the system is shown for system symmetry), the ϕ radial profiles along $\theta = 0$ and $\theta = \pi/4$ (Fig. 2.8b), and the interfacial ϕ value and normal gradient variations along the interface $r = R_1$ (Figs.

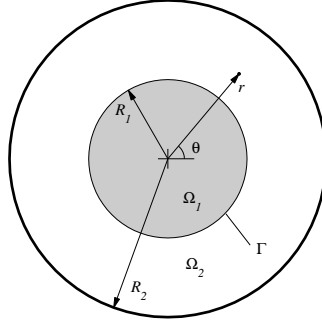


FIGURE 2.7: The schematic of the steady diffusion system with a circular interface at $r = R_1$, which separates the two coaxial domains Ω_1 for $r < R_1$ and Ω_2 for $R_1 < r < R_2$. Different transport parameters are assigned to the two domains, and a steady but non-uniform boundary condition as given by Eq.(2.34) is imposed at the outer boundary at $r = R_2$.

2.8c and d). Again there is no visual difference noticed in the distribution contours, except at the center, where the $\phi = 0$ contour line does not reach the domain center radially but turns back near it. This is from the plotting software, since the ϕ magnitude is very small near the center ($\phi = 0$ at $r = 0$) and the plotting program cannot distinguish such tiny difference in this region. Nevertheless, the contour lines are from the exact solution, and our LBM calculation actually has captured the local ϕ distribution to a reasonable accuracy (see the color patches near the center in Fig. 2.8a). Again as with the flat interfaces in previous sections, excellent agreement can be noticed in ϕ values in the separate domains and across the interface (Fig. 2.8b), as well as in the value and gradient variations along the circular interface (Figs. 2.8c and d). The correlation between the interfacial value and gradient specified by the conjugate condition Eqs.(2.4) and (2.5) is also correctly enforced.

2.3.4 Accuracy Analysis

In this section, the accuracy of our method is examined by varying the plate-plate distance H for the flat-interface system with keeping $L = H$ and $h = H/2$, or changing the inner radius R_1 for the circular-interface system with holding $R_2 = 2R_1$. To measure the numerical accuracy of our counter-extrapolation algorithm in the entire computation domain and along the conjugate interface, the following relative errors

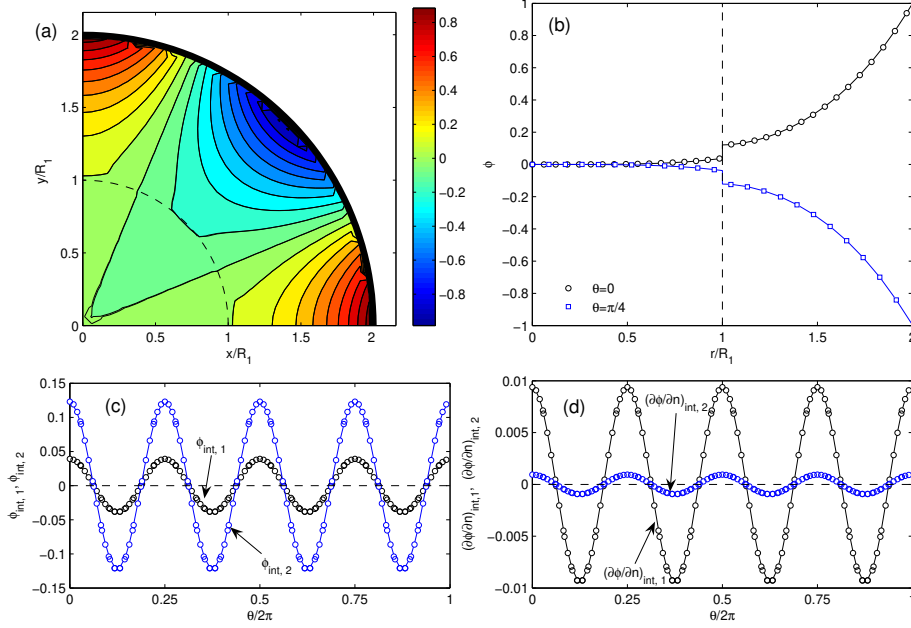


FIGURE 2.8: The ϕ distributions (a), the ϕ profiles along $\theta = 0$ and $\pi/4$ (b), the variations of interfacial values $\phi_{int,1}$ and $\phi_{int,2}$ along the interface (c), and the variations of interfacial gradients $(\partial\phi/\partial y)_{int,1}$ and $(\partial\phi/\partial y)_{int,2}$ along the interface (d) for the steady diffusion system with a circular interface. In (a) the background color patches are from our LBM calculation and the black contour lines are from the analytical solution. In (b)-(d) the symbols are LBM results and the underlying curves are theoretical predictions. The dashed arc in (a) and the dashed vertical line in (b) indicate the interface location; The dashed lines in (c) and (d) are used to separate the positive and negative interfacial properties.

are defined [38, 40]:

$$E_2 = \frac{\sum_{\Omega_1+\Omega_2} (\phi^{LBM} - \phi^{ex})^2}{\sum_{\Omega_1+\Omega_2} (\phi^{ex})^2}, \quad (2.37)$$

$$E_{2,int,1} = \frac{\sum_{\Gamma} (\phi_{int,1}^{LBM} - \phi_{int,1}^{ex})^2}{\sum_{\Gamma} (\phi_{int,1}^{ex})^2}, \quad (2.38)$$

$$E_{2,int,2} = \frac{\sum_{\Gamma} (\phi_{int,2}^{LBM} - \phi_{int,2}^{ex})^2}{\sum_{\Gamma} (\phi_{int,2}^{ex})^2}, \quad (2.39)$$

$$E_{2,qint} = \frac{\sum_{\Gamma} [(\partial\phi/\partial n)_{int,1}^{LBM} - (\partial\phi/\partial n)_{int,1}^{ex}]^2}{\sum_{\Gamma} [(\partial\phi/\partial n)_{int,1}^{ex}]^2}. \quad (2.40)$$

Here superscripts *LBM* and *ex* are used to denote the properties obtained from LBM simulations or the exact analytical solutions. We do not have another error term defined for the interface gradient $(\partial\phi/\partial n)_{int,2}$ like $E_{2,qint}$ in Eq.(2.40) for $(\partial\phi/\partial n)_{int,1}$, considering the direct proportionality between the two interface gradient terms in

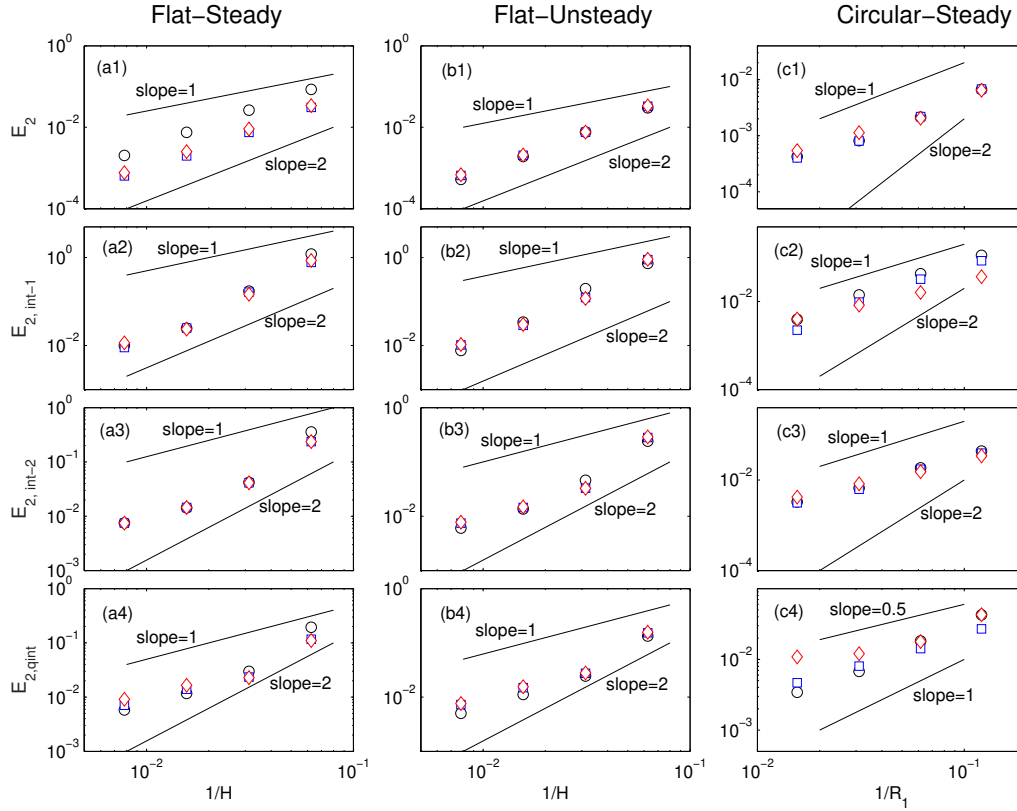


FIGURE 2.9: The relative errors E_2 (a1, b1, and c1), $E_{2, \text{int}, 1}$ (a2, b2 and c2), $E_{2, \text{int}, 2}$ (a3, b3 and c3), and $E_{2, \text{qint}}$ (a4, b4 and c4) for the steady (a1-a4) and unsteady (b1-b4) convection-diffusion systems with a flat interface and the steady diffusion systems with a circular interface (c1-c4). Effects of the interface-lattice offset distance (a1-a4: $\Delta = 0.01$ as black circles, 0.5 as blue squares, and 0.75 as red diamonds), heat capacity ratio (b1-b4: $\sigma = 0.1$ as black circles, 1 as blue squares, and 10 as red diamonds), and interface conductance (c1-c4: $\lambda R_2 / D' = 0.1$ as black circles, 2 as blue squares, and 100 as red diamonds) on the numerical accuracy have also been investigated. Straight lines with slope values are used to indicate the convergence order.

Eq.(2.5). For unsteady simulations, the above defined errors also vary with time, and periodicity can be observed shortly after a simulation starts. The periodical variations of the errors have much shorter periods (compared to the imposed boundary value variation period $2\pi/\omega$) and very small variation amplitudes. For these situations, we use the averaged error values over a complete error variation period for our following analysis.

In Fig. 2.9 we collect all the error data for E_2 (top row), $E_{2, \text{int}, 1}$ (second row), $E_{2, \text{int}, 2}$ (third row), and $E_{2, \text{qint}}$ (bottom row) from our steady (left column) and unsteady (center column) flat-interface simulations and steady circular-interface simulations

(right column). Effects of several system parameters on the simulation accuracy have also been investigated here. These errors are plotted against $1/H$ or $1/R_1$ with logarithm scales for both axes. Straight lines with their individual slope values in the log-log plots are also displayed to visualize the convergence order.

For steady cases with flat interfaces (left column in Fig. 2.9), we use $\sigma = 1$ with different interface-lattice offsets: $\Delta = 0.01$ (black circles), 0.5 (blue squares), and 0.75 (red diamonds). It appears that the offset $\Delta = 0.01$ generates larger E_2 errors (Fig. 2.9-a1), probably due to the less accurate midpoint value ϕ^m calculated via linear interpolation or extrapolation via Eqs.(2.24). The convergence orders for all errors are between 1 and 2, with that for E_2 very close to 2 (Fig. 2.9-a1) and that for $E_{2, qint}$ approximately 1.5 (Fig. 2.9-a4). It is reasonable to see E_2 has the best accuracy since it is calculated over the entire computation domain, while the inaccuracy is mainly concentrated in a thin layer near the boundary or interface where approximations are introduced [73]. On the other side, for $E_{2, qint}$, the calculation involves *finite-difference approximations* (via Eqs.2.17 and 2.18) from the *interpolated* ϕ values (via Eq.2.16) in the *interfacial* region. Since the finite-difference approximation has a second-order accuracy and the bilinear interpolation has a first-order accuracy, the error in interfacial flux $E_{2, qint}$ therefore exhibits an accuracy order between 1 and 2. Similar reduced accuracy orders have been reported in previous LBM simulations when finite-difference approximations are involved [11, 25, 49]; however, the exact mechanism is complicated and difficult to explore. For example, a recent study by Chen et al. [11] indicated that the overall numerical accuracy order and magnitude could be affected by several factors, including the system geometry and the boundary values imposed. Le et al. [38] have also tested the nine-node Lagrange quadratic interpolation scheme for the calculation of ϕ values at the finite-difference control points, and no apparent improvement has been observed in the relative errors. In the unsteady flat-interface systems (center column in Fig. 2.9), we fix the interface-lattice offset $\Delta = 0.5\delta x$ and use different σ values: $\sigma = 0.1$ (black circles), 1 (blue squares), and 10 (red diamonds). The accuracy behavior is very similar to that for the steady cases, in both the error magnitudes and convergence orders. This implies

that the unsteady variation as well as the ratio σ have no major impact on the performance of our method. The approximately second-order accuracy here are close to those reported in Ref. [16] for a similar flat-interface system; however, it should be noted that in Ref. [16] the general algorithm cannot be used for interfaces approximately parallel or perpendicular to the underlying lattice grid lines; instead, a specific decoupled algorithm was used for flat interfaces by taking advantage of the particular interface shape and orientation.

In the right column of Fig. 2.9, the errors from the steady simulations with a circular interface discussed in Sect. 2.3.3 with different interface conductance ($\lambda R_2/D' = 0.1$ as black circles, 2 as blue squares, and 100 as red diamonds) are displayed. It appears that the interface conductance does not affect the accuracy much. The overall convergence orders are approximately 1 for E_2 , $E_{2, int, 1}$, and $E_{2, int, 2}$. The $E_{2, qint}$ errors also follow the slope=1 trend in general, except the data point for $R_1 = 64.25 \delta x$ and $\lambda_2/D' = 100$. It is difficult to identify the exact reason for this particular data point considering the complexity of the system and calculations. The reduced accuracy, in all error quantities examined here, from the circular-interface cases compared the flat-interface cases are expected when one considers following facts. For the D2Q5 lattice structure used in this work, the four control points for the finite-difference approximation of interfacial gradients (Fig. 2.1b) are all along a vertical lattice grid line, and the bilinear interpolations for the ϕ values at these points via Eq.(2.16) have been simplified to linear interpolations between two lattice nodes. Also in the flat-interface systems, the interfacial values $\phi_{int, 1}$ and $\phi_{int, 2}$ are obtained from finite-difference approximations along the same lattice line where the midpoint boundary method is performed. These might be responsible for the better accuracy of flat-interface systems. Similar reduced convergence order and error scatters have also been observed in Refs. [16, 38, 40].

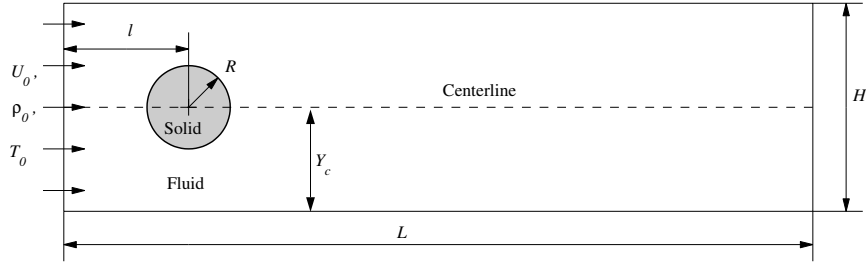


FIGURE 2.10: The schematic for simulations of the cooling processes of a hot cylinder in a cold flow. Fluid enters from the left edge of the simulation domain with density ρ_0 , velocity U_0 , and temperature T_0 , and domain boundary conditions are described in details in text.

2.3.5 Cooling Process of a Hot Cylinder in a Cold Flow under Different Insulation Conditions

At last, we simulate the cooling process of a hot cylinder with a cold fluid flowing over. The system involves unsteady flow and curved interface, and it serves as an example to demonstrate potential usefulness of our model in conjugate heat transfer systems. The transport scalar ϕ is replaced with temperature T in the following discussion. Fig. 2.10 provides a schematic description of the system setup, and we use subscripts f and s to distinguish properties of the fluid and the solid cylinder, respectively. The center of the solid cylinder of a radius R locates at $x = l$ from the inlet and $y = Y_c = H/2$ from the bottom. At the left inlet ($x = 0$), we impose a uniform flow with constant velocity U_0 , density ρ_0 , and temperature T_0 . For the top ($y = H$) and bottom ($y = 0$) boundaries and the right exit ($x = L$), we apply the following no-gradient conditions: $(\partial u / \partial y)_{y=0} = (\partial u / \partial y)_{y=H} = 0$, $(\partial \rho / \partial y)_{y=0} = (\partial \rho / \partial y)_{y=H} = 0$ (ρ is the fluid density), $(\partial T / \partial y)_{y=0} = (\partial T / \partial y)_{y=H} = 0$, $(\partial u / \partial x)_{x=L} = (\partial v / \partial x)_{x=L} = 0$, $(\partial \rho / \partial x)_{x=L} = 0$, and $(\partial T / \partial x)_{x=L} = 0$. Also the transverse velocity v is set to zero at $y = 0$ and $y = H$: $v(y = 0) = v(y = H) = 0$ [10]. The flow field is solved using the standard single-relaxation-time (SRT) LBM model with the D2Q9 (two-dimensional, nine lattice velocities) lattice structure [78, 17]. While MRT models for flows have better numerical stability in general, the simpler SRT D2Q9 model serves the demonstration purpose here well. The no-slip boundary condition over the cylinder surface is accomplished using the midpoint velocity boundary method [75]. The flow velocity from the flow calculation is then

utilized in the calculation of temperature field, in particular, via Eq.(2.13). For simplicity, we assume that the fluid properties (density, viscosity, and heat capacity) are not changing with the fluid temperature. Before starting the simulation, we set the fluid with a constant density $\rho(t = 0) = \rho_0$ and no flow velocity $\mathbf{u}(t = 0) = (0, 0)$; and $T(t = 0) = T_s$ in the cylinder and $T(t = 0) = T_f$ in fluid. These boundary and initial conditions are typical in computational studies of flows over objects, and more detailed description of the flow calculation can be found in the literature [10]. In our following simulations, we use $R = 20\delta x$, $L = 1600\delta x$, $H = 640\delta x$, $l = 300\delta x$, $\rho_0 = 1$, $U_0 = 0.05$, $T_0 = T_f = 0$, and $T_s = 1$. The fluid kinematic viscosity ν is obtained from the Reynolds number $Re = 2U_0R/\nu = 100$; and similarly the fluid heat diffusivity D_f is calculated from the Prandtl number $Pr = \nu/D_f = 2$. The heat transfer properties of the cylinder are assumed as the same of the fluid, i.e., $D_s = D_f$ and $\sigma = (\rho c_p)_s/(\rho c_p)_f = 1$.

We consider the following three cases with difference interfacial conductance configurations on the cylinder surface to mimic different insulation situations:

- *Case I*: $\lambda R/D_f = 200$ over the entire cylinder surface. This large conductance (small thermal resistance) represents the situation with no insulation layer on the surface. The results from this case have been compared to those of Case 1 in Ref. [38] (no interface discontinuity considered there) and no evident difference has been observed.
- *Case II*: $\lambda R/D_f = 1$ over the entire cylinder surface. This small conductance (large thermal resistance) represents the situation with an insulation layer around the hot cylinder.
- *Case III*: $\lambda R/D_f = 1$ for the upper half surface and $\lambda R/D_f = 200$ for the lower half surface. This setup corresponds to the situation where the insulation layer only presents on the upper half surface, and the lower half surface is exposed to fluid directly.

Fig. 2.11 shows the distributions of flow vorticity (top row) and temperature (second row for Case I, third row for Case II, and bottom row for Case III) at normalized time

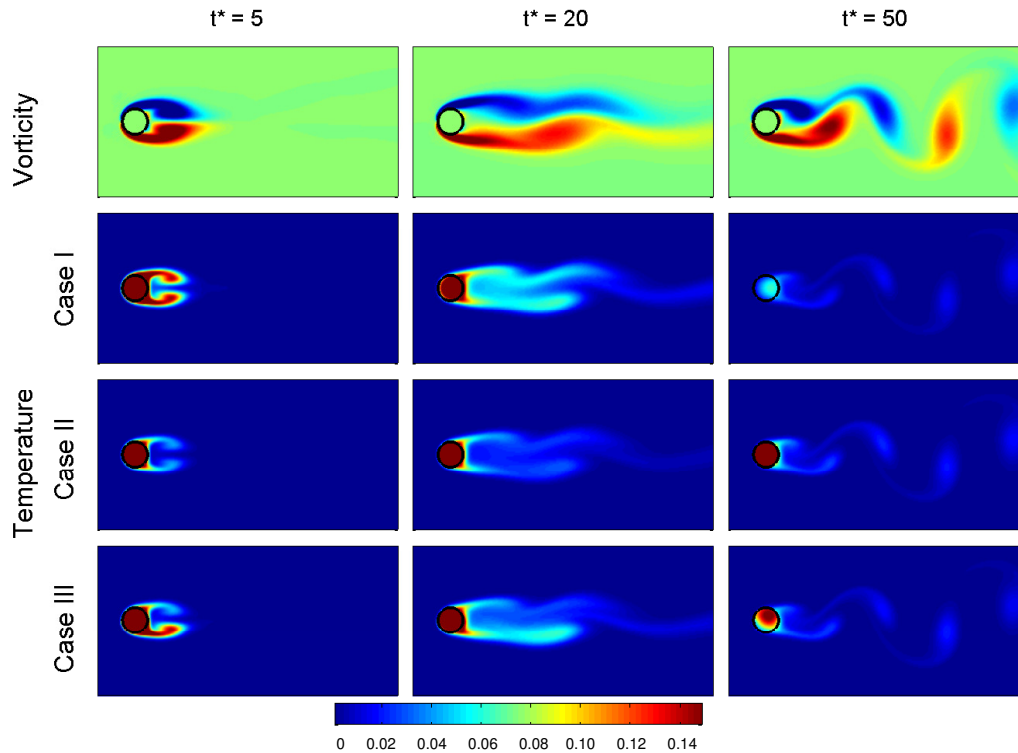


FIGURE 2.11: The distributions of flow vorticity (top row) and temperature (lower three rows, one for each case simulated) at three representative time instants during the cooling processes of the system in Fig. 2.10. All three simulations start from the same initial condition with the fluid at rest of $T_f = T_0 = 0$ and the solid cylinder of $T_s = 1$. The temperature fields here are displayed using a same color scale for direct comparison; however, the color scale is limited in the range of $0 \sim 0.15$ (i.e., temperature higher than 0.15 will be shown in the same color, which is dark red here) so we can see the relatively low fluid temperature clearly.

$t^* = tU_0/2R = 5$ (left column), 20 (center column), and 50 (right column). The flow field is the same for all the three cases since we have neglected the thermal effect on fluid properties. At $t^* = 5$, the flow is still in the early development stage and an approximately symmetric vorticity pattern is observed. The symmetric structure is then quickly destroyed as time processes, and the unsteady nature of this moderate Reynolds number flow becomes dominant at $t^* = 20$. At $t^* = 50$, the well-known Karman vortex street pattern has been established behind the cylinder. These flow patterns are consistent to results reported in previous studies [10]. The temperature fields show clear relationship to the flow structure for this convection-dominant system with the Peclet number $Pe = RePr = 200$. At $t^* = 5$, the temperature fields for Cases I and II appear symmetric about the system midplane due to the symmetric

flow structure. However, the fluid temperature in Case II is lower than that in Case I, since the surface resistance in Case II has reduced the heat flux entering fluid. For Case III, we see the temperature pattern is asymmetric about the centerline: It is similar to Case I in the lower part and similar to Case II in the upper part. Clearly this is due to the particular surface insulation condition described above.

Now we have a close look at the temperature distributions inside and around the cylinder during the cooling processes (Fig. 2.12). At $t^* = 5$, one can see the cylinder temperature in Case I has reduced slightly along the front surface, since the front surface is facing the incoming cold flow. This is not visible for Cases II, and only been seen in the lower front surface area for Case III. Meanwhile, the fluid temperature is relatively high near the two separation points of Case I and the lower separation point of Case III. This indicates that the cylinder in Case I has released more heat into fluid through its conductive surface. On the other hand, the surface resistance in Cases II and III has effectively reduced the heat flux leaving the cylinder. At $t^* = 20$, the temperature of the cylinder in Case I has significantly reduced, while that in Case II is still relatively high. Strong asymmetry is developed for the temperature field in Case III, and the pattern is clearly related to the surface insulation configuration: The solid is hotter above and cooler below, and the fluid is cooler above and hotter below. As simulations proceed, more heat is released to fluid and the cylinder temperature decreases with time. At $t^* = 50$, cylinder temperature in Case I is already quite low. In contrast, under the protection of a closed insulation layer in Case II, the cylinder is still relatively hot. Again the condition in Case III is somehow between Cases I and II, due to its half insulated surface. The fluid temperature behind the cylinder, however, appears similar among the three cases, since at this instant the temperature difference across the surface is relatively small (Case I and the lower surface in Case III) or the insulation layer (Case II and the upper surface in Case III) has efficiently depressed the heat flux for a mild temperature difference. In addition to the asymmetric patterns in Case III, also we notice the hot spot (the area with highest temperature) inside the cylinder locates slightly near the rear edge of the cylinder. This is due to the fast heat release to incoming cold fluid at the front surface.

The average cylinder temperature \bar{T} has also been calculated and plotted in Fig. 2.13. The average temperature decays with time in an approximately exponential fashion, and we thus assume the Newton cooling law. The average heat flux \bar{q} from an object can be expressed as the product of the apparent heat transfer coefficient \bar{h} and the temperature difference between the object and the surrounding medium:

$$\bar{q} = \bar{h}(\bar{T} - T_0) \quad . \quad (2.41)$$

According to the energy conservation principle, the following differential equation can be established:

$$(\rho c_p)_s R \frac{d\bar{T}}{dt} = 2\bar{h}(T_0 - \bar{T}) \quad , \quad (2.42)$$

and its solution with the initial condition $\bar{T}(t = 0) = T_s$ is

$$\bar{T} = T_s \exp(-kt) \quad , \quad (2.43)$$

where the parameter $k = 2\bar{h}/[(\rho c_p)_s R]$ controls the decaying behavior. The dashed lines in Fig. 2.13 are best fittings according to this equation. The fitted k values are 0.07933 for Case I, 0.02676 for Case II, and 0.04837 for Case III. Since $\bar{h} \propto k$, we have the heat transfer coefficient ratio for these three cases as 1:0.34:0.61, which clearly indicates the surface insulation has reduced the heat lose rate. The number 0.61 for Case III is slightly lower than the average of Case I (1.0) and Case II (0.33). This is likely due to the less uniform temperature distribution in Case III: The average temperature over-represents the effective object temperature in the Newton cooling law Eq.(2.41).

At last, in Fig. 2.14, we plot the temperature distributions along the flow direction at three transvers positions: above the cylinder at $y = Y_c + 30\delta x$ (top row), along the centerline $y = Y_c$ (center row), and below the cylinder at $y = Y_c - 30\delta x$ (bottom row). The gray areas in the center row indicate the solid region inside the cylinder, and the top and bottom rows are all for fluid temperature, since the cylinder radius

is $R = 20\delta x$. The above discussed cylinder temperature variation and decrease can be observed more quantitatively in the center row subfigures. We can also see the large temperature jump across the interface for Case II (red dashed lines).

We now turn our attention to the fluid temperature field around and downstream from the cylinder in the top and bottom rows. In the early stage of the cooling process (left and center columns), the fluid temperature in Case I is higher than that in Case II, because of the good interface conductance in Case I. The Case III curves lie between those of Cases I and II, but they are more close Case I in the lower area (Figs. 2.14 a3 and b3) and more close to Case II in the upper region (Figs. 2.14 a1 and b1), due to its particular insulation configuration. In the later simulation stage (right column), we see the fluid temperature in Case II becomes the highest, and that of Case I is the lowest. This is because at this stage the thermal energy left in the Case I cylinder is very limited (represented by the low cylinder temperature), while the Case II cylinder is still relatively hot (Fig. 2.14 c2). As a result, there is less heat released to fluid in Case I (with a conductive interface but low cylinder temperature) than in Case II (with a less conductive interface but a high cylinder temperature). The fluid temperature distribution for Case III at $t^* = 50$ exhibits some interesting features. Considering the surface conductance in Case III is identical to Case II on the upper half and to Case I on the lower half, we have expected to see the trend observed in early stage (Case III curves follow Case I below and follow Case II up) continuing in the later stage. However, this is not what we observe in Fig. 2.14 (c1) and (c3): It is very close to that of Case I in the upper region (Fig. 2.14 c1), however, very similar to that of Case II in the lower region (Fig. 2.14 c3). Our quantitative explanation to this less intuitive observation is as follows. Compared to Case I, Case III has a higher cylinder temperature at this stage but also a higher surface resistance on the upper half surface. It seems here the higher temperature has balanced the higher resistance, and as a result, they release similar heat flux on the upper surface, and the fluid passing the upper surface receives similar heat amount. On the other hand, for Cases III and II, Case III has a lower cylinder temperature but a better

surface conductance on the lower surface, and their counter effects on heat flux cancel each other approximately. This might be a coincidence from this particular set of simulation parameters we use here, and a quantitative description is difficult. Nevertheless, further investigations and analysis on this phenomenon could be an interesting topic.

2.4 Summary and Concluding Remarks

We have proposed a conjugate interface method for simulations of convection-diffusion systems between two materials with the interface discontinuity considered. With the interfacial scalar values obtained via extrapolations from individual domains, the original conjugate problem can be solved as two Dirichlet boundary value systems with an appropriate method. Compared to the other existing method [16], our counter-extrapolation method is advantageous in terms of the simple and straightforward algorithm and robust applicability to any interface-lattice relative orientation. In addition, in our model the interfacial discontinuity is simultaneously obtained from the interfacial transport flux, which is consistent to the typical treatment in heat and mass transfer. Validation simulations of steady and unsteady systems with flat and circular interfaces have been conducted, and the effects of various parameters (including the interface offset, transport diffusivity, heat capacity ratio, and interfacial conductance) have been investigated. Numerical stability has also been examined, and it is found that the method is stable over larger ranges of key system parameters, including the heat capacity, thermal conductivity, interface conductance, and temporal variation frequency. At last, the cooling process of a hot cylinder in a cold flow under different surface insulation conditions has been simulated to demonstrate the potential applications of our model in complex systems.

The discontinuity in interfacial flux has been neglected in this model development for the less commonality of interfacial chemical reactions. If necessary, the conjugate interface requirements Eqs.(2.4) and (2.5) have to be rewritten to incorporate the chemical reaction effects [8, 9, 14, 29, 35], and other equations can be modified correspondingly following the mathematical steps outlined here. The interface shapes

in this study are either planar or circular, and therefore the local normal direction is readily available. For general interfaces with arbitrary shapes, one can discretize the interface into small surface elements and use the normal direction of the surface element as an approximation of the local normal direction. For systems with large interface areas such as porous media, these local normal directions can be calculated before the simulation iterations. In this work, we have not considered the spatial motion of the interface in this study for simplicity. When the interface moves in the domain, a lattice node near the interface may switch its status from an Ω_1 node to an Ω_2 node, or vice versa. At such a node, the distribution functions for the flow and temperature (concentration) fields in the new domain do not exist, since this node has just entered into this domain. One possible technique is to approximate the missing distribution values at such nodes via extrapolations from existing neighboring nodes in this domain. This method has been used in a recent study for the diffusion-convection process of a cylinder moving in a straight channel and satisfactory results have been observed there [11]. The extrapolation and bilinear interpolation near the interface may also affect the computational efficiency, especially in parallel computation. However, such cost is inevitable to enhance the flux continuity and temperature jump across the interface, in our current method as well as other previous methods [16, 58]. At last, all the model description and simulations in this chapter are based on the MRT LBM model with the D2Q5 lattice structure; however, there is no technical difficulty to extend this method to other LBM models or lattice structures. Moreover, the basic idea of our counter-extrapolation method can also be used in other computational methods such as the finite-element or finite-volume methods for heat and mass transfer simulations.

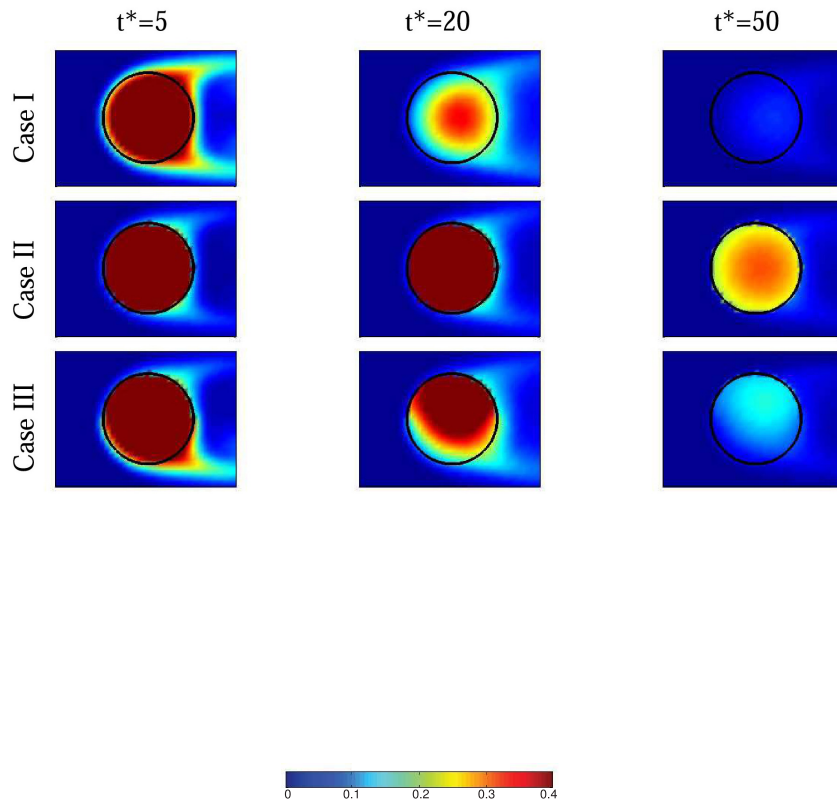


FIGURE 2.12: Close pictures of the local temperature fields inside and around the solid cylinder during the cooling processes. The temperature fields here are displayed using a same color scale for direct comparison; and the color scale is set for the range of $0 \sim 0.40$ (i.e., temperature higher than 0.40 will be shown in the same color, which is dark red here) to show the temperature fields clearly.

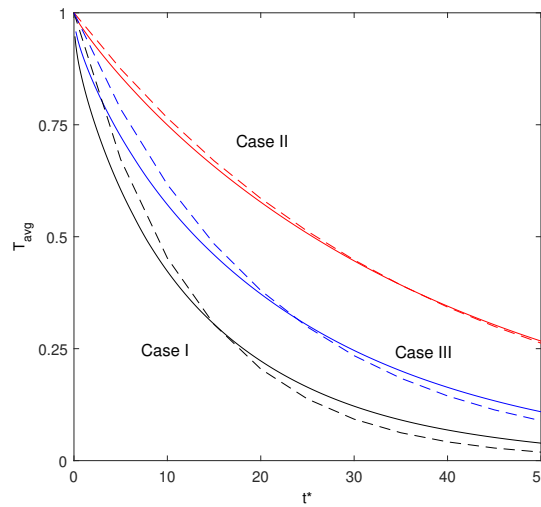


FIGURE 2.13: The changes of the average temperature of the cylinder during the cooling process for the three cases studied. The decay behavior can be approximated as an exponential decay starting from the initial temperature $T_s = 1$. The dashed lines are best fittings according to the Newton cooling law Eq.(2.43).

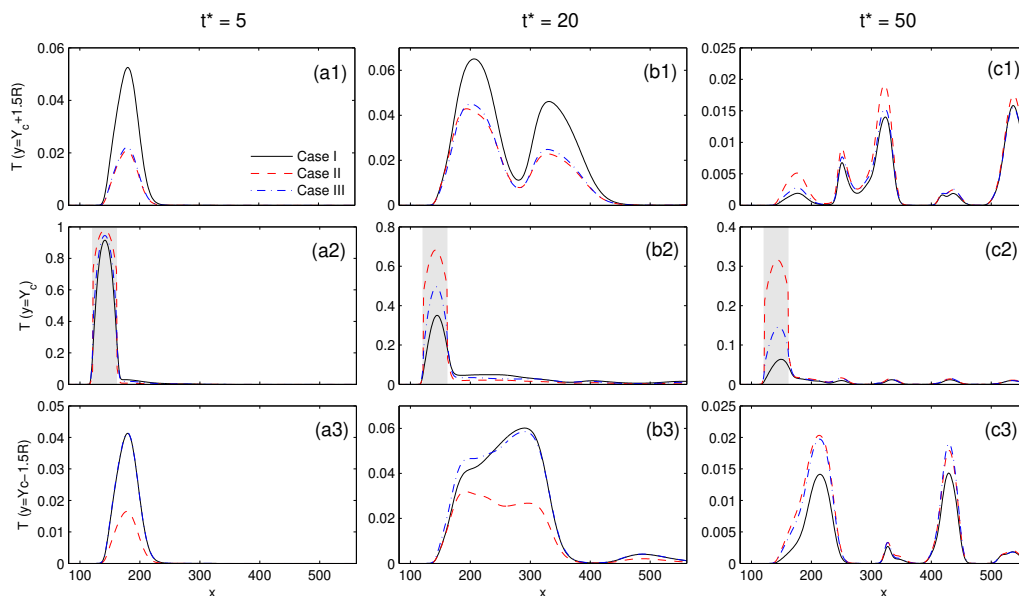


FIGURE 2.14: The temperature distributions along the system centerline (center row) as well as at $30 \delta x$ above (top row) and below (bottom row) the centerline for the three cases studied at the three representative time instances $t^* = 5$ (left column), 20 (center column), and 50 (right column). The grey areas in the center row indicate the solid region of the cylinder.

Chapter 3

Inlet And Outlet Treatment of Periodic Thermal Flow ¹

3.1 Introduction

Periodic structures are often encountered in heat exchangers and other heat transfer systems, such as wavy or grooved pipes, fin-pin cold plates, and cross-flow heat exchangers [26, 30]. When fluid property changes neglected, identical flow field and similar temperature distributions can be observed in consecutive periodic modules after some distance from the entrance. The flow is then called fully developed in both flow and thermal fields [15, 51]. Numerous studies have been conducted on this topic; among them, existing simulations mainly used traditional numerical techniques such as the finite-difference and finite-volume methods [1, 2, 15, 47, 59, 51].

Over the past two decades, the lattice Boltzmann method (LBM) has experienced significant development. In addition to various flow systems [46, 57, 66, 74, 77], LBM has also been successfully adopted to study other processes and phenomena, such as heat and mass transfer and electric and magnetic fields [17, 61, 78]. Unlike other

¹The contents in this Chapter had been published in *Physical Review E*(295: 063309, 2017). Minor revisions have been made in this Chapter.

traditional numerical schemes such as the finite-element, finite-difference, and finite-volume methods, where the governing equations of macroscopic properties are discretized mathematically, LBM works with a set of density distributions at each lattice node, and the evolution of these density distributions follows a simple collision-propagation process consecutively. Interestingly, macroscopic equations (such as the continuity and momentum equations for fluid dynamics, the convection-diffusion equation for heat and mass transfer, and the Poisson equation for electric fields) can be correctly recovered from the density distribution dynamics via mathematical analysis [17, 61]. Studies and applications have shown that LBM has some advantages over other methods in simulating multiphase flows, incorporating complex boundary geometries and moving boundaries, and implementing for parallel computation.

To simulate thermal flow systems, several approaches have been developed along with the LBM advances over the past two decades. In general, these methods can be grouped in three categories: the multispeed approach, the double-distribution approach, and the hybrid approach [10, 41]. The multispeed approach utilizes one set of distribution functions for both flow and thermal fields; however, additional lattice speeds and higher-order velocity terms are introduced to recover the macroscopic energy equation. While this approach may appear computationally attractive, its applications are relatively limited due to the severe numerical instability and the narrow temperature variation range [10]. The hybrid approach uses LBM only for the flow field, and the energy equation is solved via some other traditional numerical schemes (e.g., the finite difference method); therefore the hybrid approach is not appropriate for our present work, since LBM is not involved in the thermal field solution at all. The double-distribution method employs two sets of distribution functions: one for the flow field and one for the thermal field. The double distribution method is most often used in thermal flow simulations, since the numerical stability is significantly improved compared to the multispeed method, and the computational implement is more convenient than the hybrid approach. For these concerns,

we use the double-distribution approach in our next method description and simulation demonstration. More details on these thermal LBM models can be found in several review articles and books and references therein [17, 41, 61, 78].

As with other numerical methods, appropriate boundary conditions are crucial for accurate and meaningful LBM simulations. At lattice nodes near the boundary, there are no density distributions entering the simulation domain after the propagation step, and therefore appropriate treatments must be implemented to assign values to such unknown density distributions such that the macroscopic boundary requirements are satisfied. Typically, macroscopic constraints on boundaries are available before simulations, such as the no-slip boundary condition on wall surfaces, the pressure values at the inlet and outlet, and the wall temperature or heat flux in thermal systems. Tremendous efforts have been devoted to develop accurate and efficient boundary schemes for flow and thermal situations [17, 41, 61, 78]. However, for the periodic thermal flow discussed in this chapter, the exact velocity and temperature values at the module inlet and outlet cannot be specified, and those LBM boundary methods cannot be used. Fortunately, the particulate nature of LBM density distributions provides great convenience for applying periodic and symmetric (including the free-slip boundary condition in fluid flows and the adiabatic boundary condition in heat transfer) boundary conditions along a lattice grid line, which can be accomplished by simply *recycling* or *reflecting* the density distributions that cross the domain boundaries [61, 78]. Both periodic and symmetric boundary treatments have been frequently used in LBM flow simulations [21, 61, 80, 81, 82]; however, this technical merit has not been recognized for LBM simulations of heat transfer processes in periodic incompressible flows yet.

In this chapter, we extend the pressure periodic boundary method by Zhang and Kwok [81] to fully-developed periodic incompressible thermal flows with constant wall temperature (CWT) or surface heat flux (SHF) boundaries. The similarity features of temperature field in periodic modules in such systems are first discussed; and then the double-distribution LBM method for heat transfer is briefly outlined for

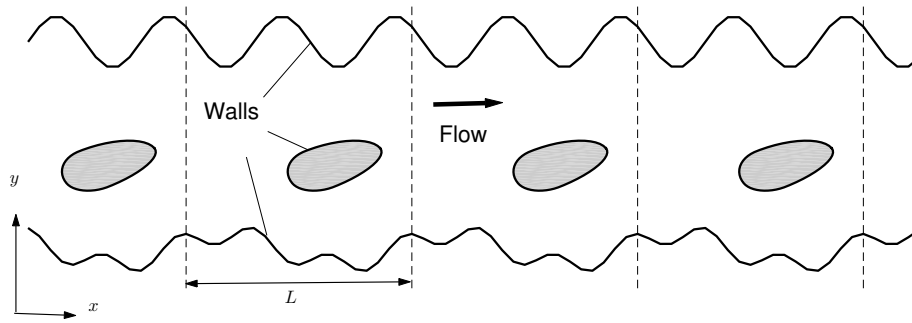


FIGURE 3.1: Schematic illustration of the periodic flow passage. The vertical dashed lines are plotted to divide the flow passage into individual periodic modules. The coordinate system is set with the x direction in the flow direction and the y direction in the transverse direction.

readers' convenience. Two different numerical approaches, the distribution modification (DM) and the source term (ST) approaches, are developed to incorporate these similarity features in LBM simulations. At last, several validation and demonstration simulations are performed to illustrate the correctness, accuracy, and usefulness of our proposed methods in LBM simulations of periodic incompressible thermal flows.

3.2 Theory and Methods

In this section we first describe in detail the periodic features of flow and temperature in fully developed periodic incompressible flows for both the CWT and SHF conditions. An outline of the LBM algorithm is included in Appendix A. Such information is well documented in the literature; and we re-present these materials here for the completeness of this chapter and for the convenience of the following discussions of our new periodic boundary treatments.

3.2.1 Fully Developed Periodic Thermal Flows

Consider the two-dimensional (2D) system illustrated in Fig. 3.1 as a general example of the fully developed periodic flows driven under a pressure gradient. The flow

and temperature fields are governed by the following continuity (Eq. 3.1), momentum (Eq. 3.2), and energy (Eq. 3.3) equations:

$$\frac{\partial \rho}{\partial t} + \rho \nabla \cdot \mathbf{u} = 0 \quad , \quad (3.1)$$

$$\frac{\partial \mathbf{u}}{\partial t} + \nabla \cdot (\mathbf{u}\mathbf{u}) = -\frac{\nabla P}{\rho} + \nu \nabla^2 \mathbf{u} \quad , \quad (3.2)$$

$$\frac{\partial T}{\partial t} + \mathbf{u} \cdot \nabla T = \alpha \nabla^2 T \quad , \quad (3.3)$$

where \mathbf{u} is the flow velocity, P is the pressure, T is the temperature, ρ is the fluid density, ν is the kinematic fluid viscosity, α is the fluid thermal diffusivity, and t is time. Here we have neglected the viscous dissipation term in the energy equation as in typically heat transfer research. When the flow is fully developed along the periodic passage, the velocity \mathbf{u} becomes identical at locations of the same relative position in each periodic module (we will call them image locations hereafter) [51, 59], i.e.,

$$\mathbf{u}(x \pm mL, y) = \mathbf{u}(x, y) \quad , \quad (3.4)$$

where L is the streamwise length of the periodic unit and m is a natural number. The fluid pressure keeps decreasing along the flow direction; however, the following relationship exists among image locations:

$$P(x \pm mL, y) = P(x, y) \mp m\Delta P_L \quad , \quad (3.5)$$

and the pressure drop over each periodic unit ΔP_L remains constant. It is easy to verify that $\mathbf{u}(x \pm mL, y)$ and $P(x \pm mL, y)$ are still valid solutions of the continuity and momentum equations Eqs. (3.1) and (3.2), since the identical velocity and shifted pressure cause no change to any terms in these governing differential equations. Meanwhile, the noslip boundary condition, if satisfied in one unit, will also be satisfied in all other units. To obtain an exact periodic boundary condition for pressure like Eq. (3.4) for velocity, Patankar et al. [51] split the fluid pressure P into two components: a global pressure term $-\Delta P_L x/L$ and a local reduced pressure \tilde{P} :

$$P(x, y) = -\frac{\Delta P_L}{L}x + \tilde{P}(x, y) \quad . \quad (3.6)$$

After this modification, the momentum equation Eq. (3.2) is rewritten to

$$\frac{\partial \mathbf{u}}{\partial t} + \nabla \cdot (\mathbf{u}\mathbf{u}) = -\frac{\nabla \tilde{P}}{\rho} + \nu \nabla^2 \mathbf{u} + \frac{\Delta P_L}{\rho L} , \quad (3.7)$$

and Eq. (3.5) now changes to a perfect periodic boundary condition:

$$\tilde{P}(x \pm mL, y) = \tilde{P}(x, y) . \quad (3.8)$$

As for the temperature field, the periodic features depend on the boundary conditions imposed on the walls. For fully developed periodic thermal flows to be established, the solid surfaces must have a uniform, constant wall temperature (CWT) T_w , or they can have specified surface heat flux (SHF). For the latter situation, the heat flux could be uniform or varying over the surface within one module, but it must have the same distribution for all units. For the CWT systems, usually we first shift the temperature field by the wall temperature T_w to a reduced temperature θ

$$\theta(x, y) = T(x, y) - T_w , \quad (3.9)$$

and the energy equation Eq. (3.3) becomes

$$\frac{\partial \theta}{\partial t} + \mathbf{u} \cdot \nabla \theta = \alpha \nabla^2 \theta ; \quad (3.10)$$

with the wall boundary condition for θ as $\theta(\Omega) = 0$ (here Ω denotes the wall surface). The periodic relationship for θ among modules is expressed as

$$\theta(x \pm mL, y) = e^{-\lambda_L(\pm mL)} \theta(x, y) , \quad (3.11)$$

where λ_L is the decaying rate that describes the overall temperature variation in the streamwise direction [59]. Similar to the flow velocity and pressure discussed above, one can see that, if $\theta(x, y)$ is a valid solution in one unit, $\theta(x \pm mL, y)$ from the above equation will automatically satisfy the energy equation Eq. (3.10) in other

units. Stalio and Piller [59] then introduced a normalized temperature $\bar{\theta}(x, y)$ as

$$\bar{\theta}(x, y) = \frac{\theta(x, y)}{e^{-\lambda_L x}} = \frac{T(x, y) - T_w}{e^{-\lambda_L x}} . \quad (3.12)$$

As a result, the energy equation for $\bar{\theta}$ is

$$\frac{\partial \bar{\theta}}{\partial t} + \mathbf{u} \cdot \nabla \bar{\theta} = \alpha \nabla^2 \bar{\theta} + (\alpha \lambda_L^2 + \lambda_L u_x) \bar{\theta} - 2\alpha \lambda_L \frac{\partial \bar{\theta}}{\partial x} \quad (3.13)$$

with an exact periodic boundary condition

$$\bar{\theta}(x \pm mL, y) = \bar{\theta}(x, y) . \quad (3.14)$$

In Eq. (3.13), u_x represents the x component of the flow velocity vector \mathbf{u} .

To determine the decaying rate λ_L , Stalio and Piller [59] integrated the energy equation Eq. (3.13) and obtained λ_L as the root of a quadratic equation. Here we propose another simpler approach to find λ_L by considering the energy conservation over a periodic module. Taking the fluid volume in a periodic unit as the control volume, there are five streams of heat fluxes crossing the control volume boundaries (including the walls and the inlet and outlet of the periodic unit):

- Heat flux *entering* the control volume with flow at the inlet: $\rho c \int_{in} u_{x, in} \theta_{in} dy$;
- Heat flux *leaving* the control volume with flow at the outlet: $\rho c \int_{out} u_{x, out} \theta_{out} dy$;
- Streamwise diffusion flux *leaving* the control volume at the inlet: $\kappa \int_{in} \left(\frac{\partial \theta}{\partial x} \right)_{in} dy$;
- Streamwise diffusion flux *entering* the control volume at the outlet: $\kappa \int_{out} \left(\frac{\partial \theta}{\partial x} \right)_{out} dy$;
- Heat flux *leaving* the control volume over the wall surface Ω : $\kappa \int_{\Omega} \left(\frac{\partial \theta}{\partial n} \right)_{\Omega} ds$.

According to the energy conservation principle, for a steady system we have:

$$\begin{aligned} \rho c \int_{in} u_{x, in} \theta_{in} dy &- \rho c \int_{out} u_{x, out} \theta_{out} dy - \kappa \int_{in} \left(\frac{\partial \theta}{\partial x} \right)_{in} dy \\ &+ \kappa \int_{out} \left(\frac{\partial \theta}{\partial x} \right)_{out} dy - \kappa \int_{\Omega} \left(\frac{\partial \theta}{\partial n} \right)_{\Omega} ds = 0 . \end{aligned} \quad (3.15)$$

Here we use the subscripts *in* and *out* to indicate the inlet and outlet locations, and n for the local normal direction on the wall surface. c is the heat capacity and κ is the thermal conductivity of the fluid. Now applying the periodic relationships in Eqs. (3.4) for velocity \mathbf{u} and (3.11) for T , the decaying rate λ_L can be solved as

$$\lambda_L = -\frac{1}{L} \ln \left[1 - \frac{\alpha \int_{\Omega} \left(\frac{\partial \theta}{\partial n} \right) ds}{\int_{in} \left(u_x \theta + \alpha \frac{\partial \theta}{\partial x} \right)_{in} dy} \right] . \quad (3.16)$$

Compared to the calculation method in Ref. [59], our method does not require volumetric integration over the entire simulation domain, which could be computational expensive especially in three-dimensional simulations.

Now we turn our attention to the SHF systems. In this situation, the periodic relationship for temperature is given as

$$T(x \pm mL, y) = T(x, y) \pm m\Delta T_L , \quad (3.17)$$

which is similar to that for the normal fluid pressure P in Eq. (3.5). Here ΔT_L is the temperature change over a periodic unit and it is constant along the flow. Accordingly, Patankar et al. [51] defined a reduced temperature \tilde{T} as

$$\tilde{T}(x, y) = T(x, y) - \frac{\Delta T_L}{L} x \quad (3.18)$$

to achieve a perfect periodic boundary condition for \tilde{T} :

$$\tilde{T}(x \pm mL, y) = \tilde{T}(x, y) ; \quad (3.19)$$

and the energy equation should be rewritten correspondingly to

$$\frac{\partial \tilde{T}}{\partial t} + \mathbf{u} \cdot \nabla \tilde{T} = \alpha \nabla^2 \tilde{T} - \frac{u_x \Delta T_L}{L} . \quad (3.20)$$

The temperature change ΔT_L can be relatively easily found from the energy conservation principle:

$$\Delta T_L = \frac{\int_{\Omega} q ds}{\rho c \int_{in} u_{x,in} dy} , \quad (3.21)$$

i.e., the temperature change equals the total thermal energy addition via the surface divided by the product of flow rate and volumetric heat capacity (ρc). Here q is the local heat flux entering the fluid domain via the boundary walls.

3.2.2 Simulating Periodic Thermal Flows with LBM

In LBM, governing equations are solved by means of density distributions, which undergo consecutive propagation and collision processes over a lattice grid. In the work, we use the double-distribution thermal LBM scheme for method descriptions and simulation demonstration. The D2Q9 (two-dimensional and of nine lattice velocities) lattice structure and the single-relaxation Bhatnagar-Gross-Krook (BGK) model are used for both flow and thermal fields. Please refer to Appendix A for details.

For Flow Field

Under a given pressure drop ΔP_L per periodic module, it is convenient to use the reduced pressure \tilde{P} defined in Eq. (3.6), and the LBM equations for f_i given in Appendix A can then be used $\mathbf{F} = (\Delta P_L / \rho L, 0)^T$. The classical periodic boundary condition [78] can then be applied at the periodic boundaries, meaning density distributions leaving the domain outlet will re-enter the domain at the inlet, or vice versa. This method has been widely used in LBM simulations, although more dedicated treatments are available to impose the pressure drop directly for some particular situations like multiphase or multicomponent flows [81]. To simulate a periodic flow with a specific flow rate, the pressure drop ΔP_L can be dynamically adjusted according to the simultaneous flow rate till the desirable value is established.

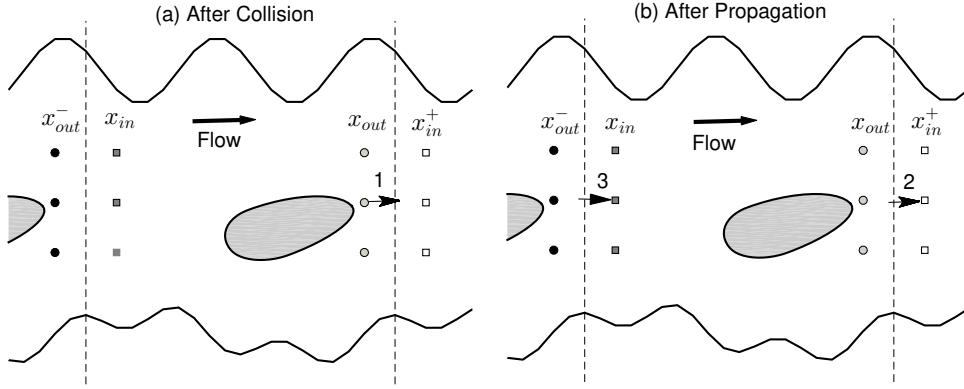


FIGURE 3.2: Schematic illustrations of the modified periodic boundary treatment for thermal field. The inlet nodes are displayed as squares and the outlet nodes are shown as circles, with the color changing from black to white along the flow direction. The numbered arrows are used to show how a density distribution leaving the outlet can be adopted to specify the incoming distribution at the inlet. Please refer the text for detailed method description.

For Thermal Field: The Source Term (ST) Approach

Similarly, by tuning the source term δh_i according to Eq. (A.13), the LBM algorithm for h_i in Appendix A can be used to solve Eq. (3.13) for CWT systems

$$\delta h_i = \omega_i \left[(\alpha \lambda_L^2 + \lambda_L u_x) \bar{\theta} - 2\alpha \lambda_L \frac{\partial \bar{\theta}}{\partial x} \right] \quad (3.22)$$

for energy scalar $A = \bar{\theta}$; or to solve Eq. (3.20) for SHF cases with

$$\delta h_i = \omega_i \left[-\frac{u_x \Delta T_L}{L} \right] \quad (3.23)$$

for energy scalar $A = \tilde{T}$. The temperature change ΔT_L for SHF cases can be readily calculated from the total heat flux over surface via Eq. (3.21); however, for CWT systems, the decaying rate λ_L is unknown before the simulation. In our practice, we start with an initial guess and run the simulation for some time (2000 time steps in our simulations) with that initial value. After that, a new λ_L value is calculated via Eq. (3.16) every certain time steps (we use 20 time steps), till the simulation becomes steady in flow and temperature fields. The differential term $\partial \bar{\theta} / \partial x$ in Eq. (3.13) can be estimated by a finite difference approximation.

For Thermal Field: The Distribution Modification (DM) Approach

Another way to incorporate the periodic features of the temperature field described in Sect. 3.2.1 is to modify those density distributions h_i that cross the module inlet or outlet boundaries, as done in Ref. [81] for pressure periodic boundary conditions. We consider the CWT situation in the periodic system shown in Fig. 3.1, and enlarge one module in Fig. 3.2 with the first column of lattice nodes at x_{in} (dark gray squares) and the last column at x_{out} (light gray circles). Also displayed there are the outlet nodes of the upstream module at $x_{out}^- = x_{in} - \delta x = x_{out} - L$ (black circles) and the inlet nodes of the downstream module at $x_{in}^+ = x_{in} + L = x_{out} + \delta x$ as (white squares); although these nodes are actually not involved in the LBM calculation. To avoid the extra source term in Eq. (3.13), we will use LBM to solve the energy equation Eq. (3.10) for θ . Now let us take the post-collision distribution $h_1^*(x_{out})$ at x_{out} (Arrow 1 in Fig. 3.2a) as an example. In the propagation step, $h_1^*(x_{out})$ is supposed to move to the next node in velocity $\mathbf{c}_1 = (1, 0)^T$, and becomes the incoming distribution at the inlet node of the downstream module x_{in}^+ (Arrow 2 in Fig. 3.2b). However, now it is out of our simulation domain and therefore cannot participate in the LBM calculation anymore. On the other side, we need the incoming distribution $h_1(x_{in})$ at the domain inlet x_{in} (Arrow 3 in Fig. 3.2b), but it is not available since the nodes at the x_{out}^- are not in the simulation domain either. Based on the periodic relationship of temperature given in Eq. (3.11) and $\theta = \sum_i h_i$ (Eq. A.3 with $A = \theta$), it is reasonable to assume the proportionality in θ can be extended to each distribution h_i , and therefore one has

$$h_1(x_{in}, t + \delta t) = e^{\lambda L} h_1(x_{in}^+, t + \delta t) = e^{\lambda L} h_1^*(x_{out}, t) \quad . \quad (3.24)$$

This analysis can be extended to other lattice distributions that cross the periodic boundaries during the propagation step, and a modified periodic boundary treatment for these distributions can be established as (for the D2Q9 lattice model used

here)

$$h_i(x_{in}, y_{in}, t + \delta t) = e^{\lambda_L L} h_i^*(x_{out}, y_{out}, t) \quad , \quad y_{in} = y_{out} + c_{i,y} \delta t, \quad i = 1, 5, 8 \quad (3.25)$$

$$h_i(x_{out}, y_{out}, t + \delta t) = e^{-\lambda_L L} h_i^*(x_{in}, y_{in}, t) \quad , \quad y_{out} = y_{in} + c_{i,y} \delta t, \quad i = 3, 6, 7 \quad (3.26)$$

Here $c_{i,y}$ is the y -component of the lattice velocity \mathbf{c}_i .

This distribution modification (DM) approach is also applicable to the SFH cases. Here we work with the original energy equation Eq. (3.3) and re-write the periodic relationship for the regular temperature T Eq. (3.17) to define a proportional factor β as

$$\beta = \frac{T(x_{in}^+)}{T(x_{in})} = 1 + \frac{\Delta T_L}{T(x_{in})} \quad ; \quad (3.27)$$

and, following the above discussion, the modified periodic boundary condition for h_i in SHF systems is

$$h_i(x_{in}, y_{in}, t + \delta t) = \beta^{-1} h_i^*(x_{out}, y_{out}, t) \quad , \quad y_{in} = y_{out} + c_{i,y} \delta t, \quad i = 1, 5, 8 \quad (3.28)$$

$$h_i(x_{out}, y_{out}, t + \delta t) = \beta h_i^*(x_{in}, y_{in}, t) \quad , \quad y_{out} = y_{in} + c_{i,y} \delta t, \quad i = 3, 6, 7 \quad . \quad (3.29)$$

Note these modified periodic treatments revert back to the classical periodic boundary condition in LBM when the proportional factor $e^{-\lambda_L}$ or β is set to 1.

3.3 Validation and Demonstration Simulations

In this section, we apply the periodic treatments described above to simulate the flow and temperature fields in several simple, however representative and carefully designed periodic systems, including flows through a flat channel, a wavy channel, and a square array of circular cylinders. Both CWT and SHF boundary conditions are considered, and results are compared with available analytical solutions, previous publications, or our own LBM results using different simulation techniques (DM vs. ST approaches and one-module vs. two-module domain simulations).

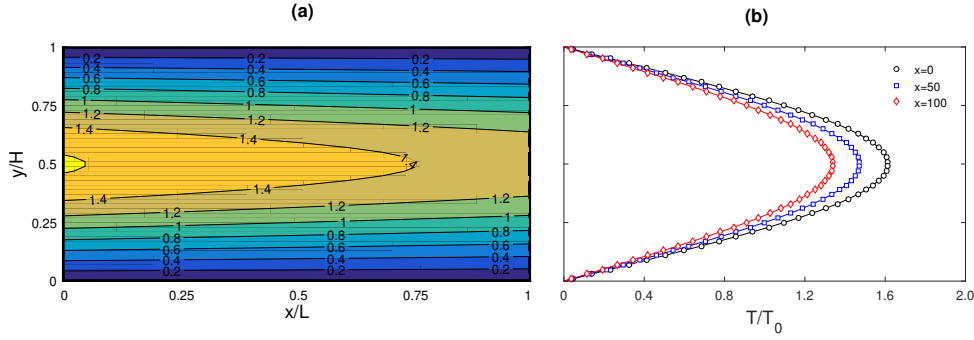


FIGURE 3.3: The simulated temperature field (a) and transverse profiles (b) for flow through the flat channel with CWT condition on the channel surfaces. In (b) the symbols are our LBM results and the underlying curves are from the analytical solution in Appendix B.

3.3.1 Heat Transfer of Laminar Flow through 2D Flat Channel

The fully developed flow in a uniform pipe or channel can be considered as an extreme example of periodic flows, for which the periodic module can be selected as a segment of the channel of any finite length. Here our simulation domain is a 2D rectangle of length $L = 100$ and height $H = 50$ (Both L and H , as well as other LBM parameters to be given in this section, are all non-dimensional values). The mid-point boundary method recently developed by Zhang and co-workers [10, 11, 75] is implemented at the solid-fluid boundaries for both flow and thermal LBM calculations for all simulations in this chapter. The Reynolds number $Re = U_0 H / \nu$ is 40, with the mean flow velocity U_0 defined as

$$U_0 = \frac{1}{H} \int_0^H u_x dy \quad (3.30)$$

The Prandlt number $Pr = \nu / \alpha$ is 0.7. The CWT situation is considered here and wall temperature T_w is set as 0; thus the regular temperature T and the reduced temperature θ are the same. During the simulation, the mean flow temperature at the domain inlet $T_0 = T_m(x = 0)$ is maintained at 1. Brown [6] had developed an analytical solution in polynomial series for thermal flows between parallel plates with constant temperature, however, with the axial diffusion neglected. In Appendix B, we extend the Brown solution to include the axial diffusion effect. Fig. 3.3 shows the comparison between our LBM results using the DM periodic boundary method

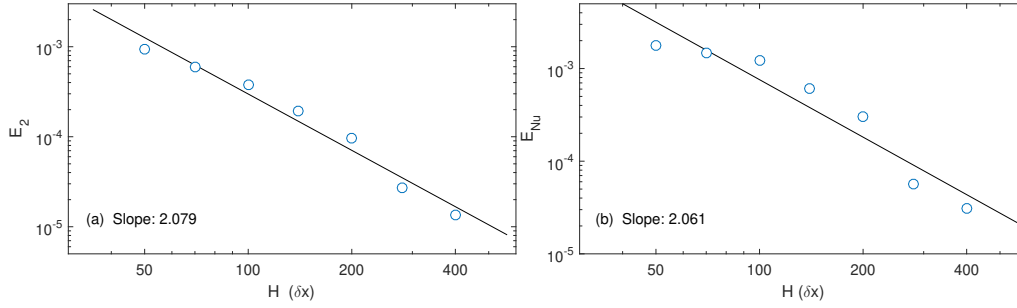


FIGURE 3.4: The relative errors E_2 (a) and E_{Nu} (b) for flows through CWT flat channels with different channel height H . The straight lines are linear fittings of the LBM data points (symbols) in the log-log plots, and the line slopes are displayed in the figure labels.

and those from our analytical solution (see Appendix B) for the temperature field. No visible discrepancy can be observed. According to our analytical solution the Nusselt number along the channel is constant at 3.7723; while our LBM yields a range of 3.7736 ± 0.0065 (mean \pm SD) along the channel. The relative difference is only $-0.14 \sim 0.21\%$. This small difference could be from several sources, including the basic LBM algorithm [17, 39, 61], the simple force term treatment in Eq. (A.12) [41], the finite-difference approximations involved in our calculation, as well as the boundary methods [50]. Further investigations for the individual contributions from different aspects (and they are very likely inter-coupled) is out of the scope of this chapter.

For a more quantitative assessment of the numerical accuracy, we simulate the above system using different channel height H with the length-height ratio constant at $L/H = 2$. The global relative error E_2 is defined as

$$E_2 = \left[\frac{\sum (T_{LBM} - T_{th})^2}{\sum T_{th}^2} \right]^{1/2}, \quad (3.31)$$

where both summations are carried out over all lattice nodes in the simulated domain. The subscripts LBM and th are used to indicate, respectively, the LBM calculated temperature values and theoretical values from the analytical solution given in Appendix B. In addition, the local Nusselt number for this system can be calculated

from the temperature filed by

$$Nu(x) = \frac{(\partial T / \partial n)_{y=0} H}{T_m(x) - T_w} , \quad (3.32)$$

where T_m is the local mean flow temperature

$$T_m(x) = \frac{\int_0^H u_x(x, y) T(x, y) dy}{\int_0^H u_x(x, y) dy} . \quad (3.33)$$

The relative error with respect to this theoretical Nusselt number Nu_{th} has also be defined as

$$E_{Nu} = \left[\frac{\sum (Nu_{LBM} - Nu_{th})^2}{\sum Nu_{th}^2} \right]^{1/2} . \quad (3.34)$$

Here the summations are performed along the two boundary walls, and $Nu_{th} = 3.7723$ from our analytical solution. These relative errors at different channel height H are plotted in Fig. 3.4 in the log-log scale. Clearly the relative errors decrease with the channel height H , and the declining slopes in the log-log graphs are approximately 2, which is similar to previous observations of other LBM models [17, 41].

3.3.2 Heat Transfer of Laminar Flow through 2D Wavy Channel

The flow and heat transfer through wavy channels have been extensively investigated for its practical applications [2, 47, 54, 59, 65]. Here we consider the same geometry as in these studies, and model the symmetric wavy wall shape by

$$H(x) = H_{avg} - 2a \cos \left(\frac{2\pi x}{L} \right) , \quad (3.35)$$

where $H(x)$ is the local channel width, H_{avg} is the average channel width over a periodic unit, and a is the wavy amplitude. The maximum channel width $H_{max} = H_{avg} + 2a$ occurs at the middle $x = L/2$ and the minimum width $H_{min} = H_{avg} - 2a$ occurs at the inlet $x = 0$ and outlet $x = L$. Following those previous studies, we use $H_{avg}/L = 13/28$ and $a/L = 1/8$. The computational domain length here is $L = 240$. As in the flat channel simulation, we have $T_w=0$, $T_0=1$, and $Pr=0.7$; and the

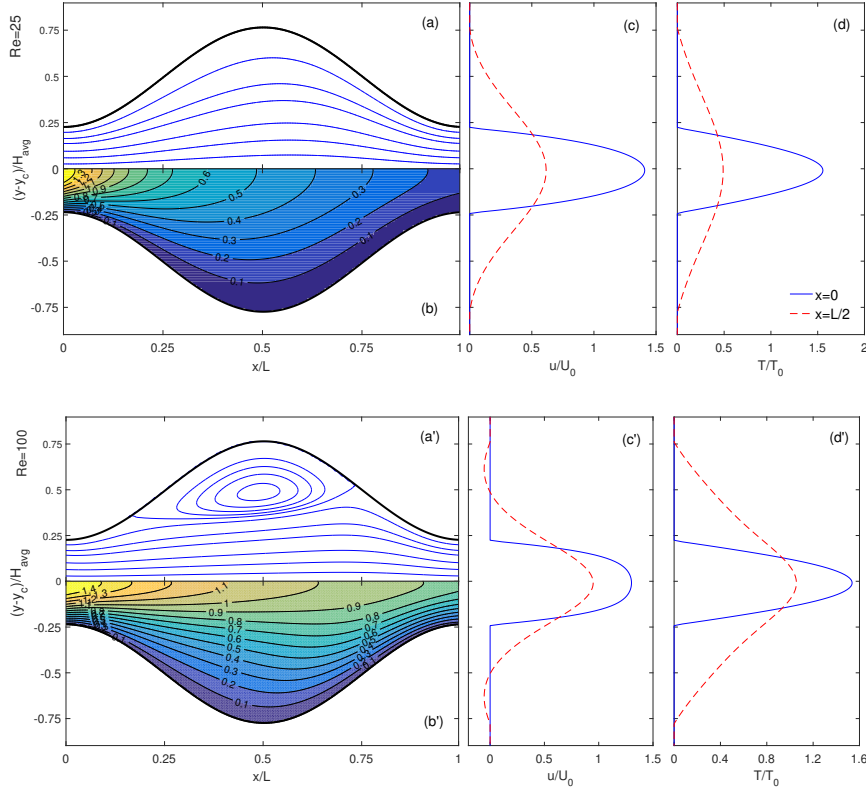


FIGURE 3.5: The simulated flow (a and a') and temperature (b and b') fields and transverse velocity and temperature profiles (c and c' for the streamwise velocity; and d and d' for the temperature) at two locations $x = 0$ and $x = L/2$ for the flows through a wavy channel with Reynolds number $Re = 25$ (a-d) and $Re = 100$ (a'-d').

DM method is used to incorporate the boundary periodicity. The Reynolds number is defined as $Re = U_0 H_{avg} / \nu$ [2, 54], and two values, $Re = 25$ and 100 , are tested in our simulations.

Fig. 3.5 collects our LBM results of these two calculations, including the flow streamlines, the isotherms, and the spanwise profiles of streamwise velocity u_x and temperature T at the maximum and minimum width locations. The streamline and isotherm patterns are very similar to those reported in previous studies [2, 54]; however, a direct comparison is difficult due to the lack of original data for those publications and analytical solutions of this system. At $Re = 100$, a pair of circulation vortex have developed in the wide section, and the separation and reattachment locations are similar to those in Ref. [2]. In Fig. 3.6, we also plot the distribution profiles of the

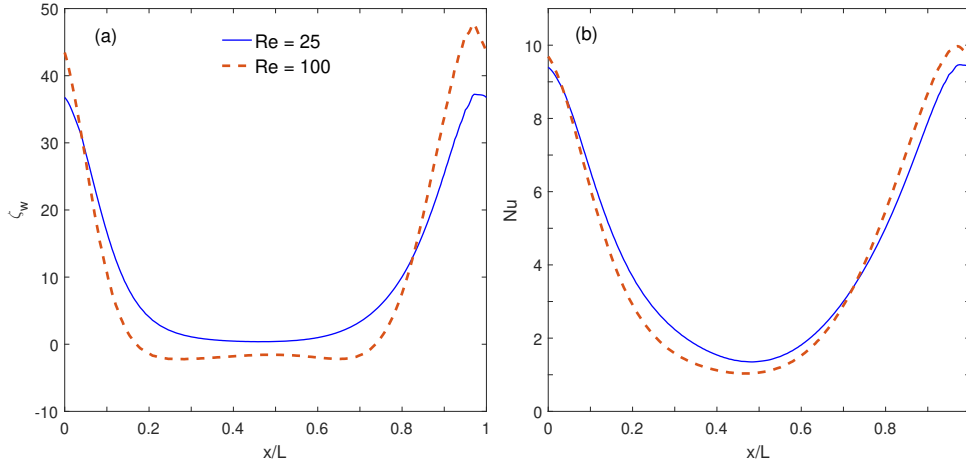


FIGURE 3.6: Distributions of the normalized wall vortex ζ_w and local Nusselt number Nu along the channel wall.

normalized wall vorticity ζ_w [65]

$$\zeta_w = \frac{1}{2} Re C_f \left(\frac{H_{max}}{H_{avg}} \right)^2 = \frac{1}{2} Re \frac{\tau_w}{\rho U_0^2 / 2} \left(\frac{H_{max}}{H_{avg}} \right)^2 \quad (3.36)$$

and the local Nusselt number Nu . Here C_f is the local frictional coefficient and τ_w is the wall shear stress. These distribution profiles are very similar to those reported in Ref. [65], both in the variation trend and magnitude. More quantitatively, we manually measure the velocity values u_x^c at the domain center ($L/2, y_c$) (y_c is the y -location of the channel centerline) from figures in Refs. [2, 54], and compare them to ours in Table 3.1. In addition, we have also calculated the friction factor f

$$f = \frac{\Delta P_L}{\rho U_0^2 / 2} \frac{H_{avg}}{L} \quad (3.37)$$

and average Nusselt number $\langle Nu \rangle$ for a periodic module [2, 47]

$$\langle Nu \rangle = \frac{[T_m(0) - T_m(L)] \int_{in} u_x dy H_{avg}}{LMTD \alpha} , \quad (3.38)$$

where $LMTD$ is the log-mean temperature difference in the module

$$LMTD = \frac{T_m(0) - T_m(L)}{\ln[T_m(L)/T_m(0)]} . \quad (3.39)$$

These values are also listed in Table 3.1 in comparisons with those from previous

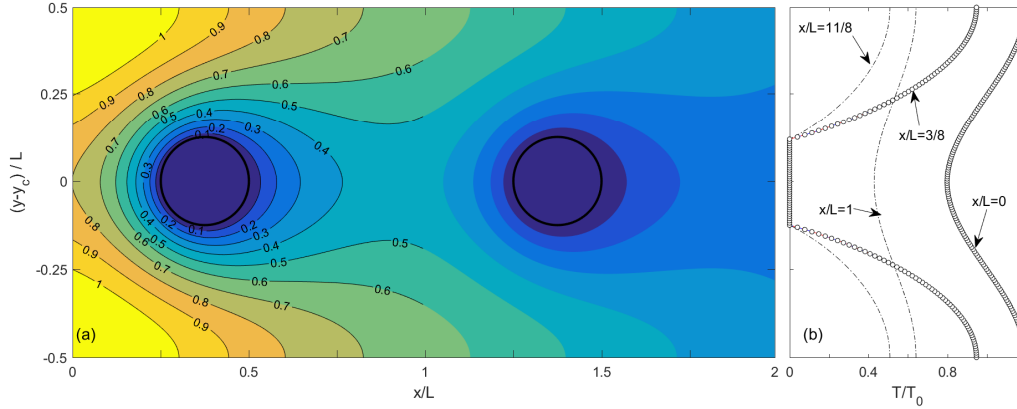


FIGURE 3.7: Result comparison of the simulations for the cooling process of flow around cylinder with one or two modules included in the simulation domain. In (a) for the temperature field, the color patches are from the two-module simulation, and the isotherm lines are from the one-module simulation. The temperature profiles at $x/L = 0, 3/8, 1,$ and $11/8$ (indicated by labels) are displayed in (b), with the symbols from the one-module calculation and curves from the two-module calculation.

studies. It can be seen there that our results, including the domain center velocity, friction factor, and average Nusselt number, all agree well to previous publications. As discussed in Ref. [54], the discrepancy among these studies might be due to the different numerical methods employed.

3.3.3 Heat Transfer in Flow through Square Cylinder Array

The last system we simulate represents the heat transfer process associated to laminar flow through a square array of circular cylinders, which resembles the interior configuration of a cross-flow tube heat exchanger [26, 30]. The periodic module here is a square with $L = H = 160$, and the cylinder has a diameter of $D = 40$ and its center locates at $(3L/8, L/2)$. The flow direction is from the left to the right in the x -direction, and the regular periodic boundary condition is applied along the top and bottom edges. The Reynolds number $Re = U_0 H / \nu = 2.4$ and the Prandtl number $Pr = 1$.

For a fully developed periodic incompressible flow, if the periodic relationships are physically correct and they have been accurately implemented in a numerical model, using one or two or even multiple periodic modules as the simulation domain should generate the same results. To confirm this statement, we perform two

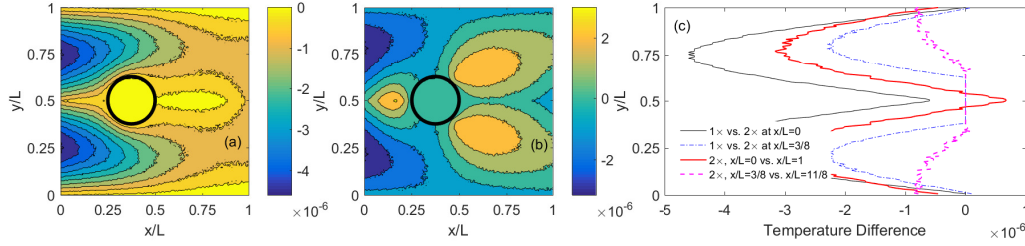


FIGURE 3.8: Distributions of temperature difference in the left $L \times L$ domain between the one-module and two-module simulations (a), and that between the left ($x \in [0, L]$) and right ($x \in [L, 2L]$) half domain from the two-module simulation (b). In (b) the temperature in the right half domain has been scaled up by a factor of $e^{\lambda_L L}$ for direct comparison. Panel (c) shows the temperature difference from panels (a) and (b) at two representative x locations.

separate simulations for the above described cylinder array system: the first one includes one module with a square simulation domain of $L \times L$, and the second one includes two modules with a rectangular domain of $2L \times L$ and it has two cylinders: one at $(3/8L, L/2)$ and another at $(11/8L, L/2)$. The cylinder surface temperature $T_w = 0$ and inflow average temperature $T_0=1$. No analytical solutions is available for this system. Comparison of these two sets of results is displayed in Fig. 3.7. Please note that in Fig. 3.7a for the temperature field, the color patches are from the two-module simulation while the isotherm lines are from the one-module calculation. Clearly they agree to each other excellently and the isotherm lines follow the color patch edges exactly. More quantitatively, in Fig. 3.7b, we plot the temperature profiles at several representative streamwise locations, and we see those at $x/L = 0$ and $3/8$ from the two simulations match each other perfectly. The difference in temperature in the first module from these two calculations is of the order $10^{-6} \sim 10^{-5}$. We also plot the temperature profiles at corresponding locations in the second module (i.e., $x/L = 1$ and $11/8$) from the two-module simulation, and we can clearly see the proportional similarity in variation as expressed in Eq. (3.11). Actually the profiles at $x/L = 1$ and $11/8$ scaled up by $e^{\lambda_L L}$ ($\lambda_L = 3.885233 \times 10^{-3}$ from the one-module simulation and $\lambda_L = 3.885264 \times 10^{-3}$ from the two-module simulation; they are almost identical) are also plotted in the figure; however they are visually indistinguishable from the profiles at $x/L = 0$ and $3/8$.

A more direct comparison of the temperature fields from these two simulations is

presented in Fig. 3.8. The magnitude of temperature difference, from the two different simulations, or between the left and right sections of the same two-module simulation, is of the order of $10^{-6} \sim 10^{-5}$. With the inlet mean temperature of 1 in these simulations, this difference can be considered as the relative errors as well. The patterns in Figs. 3.8a and b appear interesting; however, it is difficult for the authors to explore the underlying mechanisms due the system complexity. With this comparison, it is further confirmed that the periodic features have been correctly and accurately implemented in our method and program.

So far all our simulations are for the CWT boundary condition and only the DM approach has been used. At last, we test the SHF boundary condition and the ST approach using the same cylinder array geometry. Four individual simulations are conducted: CWT+DM (the same one-module simulation described above), CWT+ST, SHF+DM, and SHF+ST. To impose a desirable heat flux (i.e., normal temperature gradient) on the surface, the Neumann boundary method developed by Oulaid et al. [49] is employed. With the inlet mean temperature $T_0 = 1$ and wall temperature $T_w = 0$, the CWT case represents a cooling process. On the other hand, for SHF case, we use a uniform surface flux with $\partial T/\partial n = -0.01$ for the cylinder surface and it therefore is a heating process. Results from these simulations, including the temperature field in the domain and two representative transverse temperature profiles, are collected in Fig. 3.9. The cooling or heating effect from the cylinder is clearly indicated by the isotherms in Figs. 3.9 a and a', respectively. It is interesting to see that, in Fig. 3.9a' for the SHF boundary situation, the temperature increases along the centerline near the outlet. This is understandable since the outlet is close to the heating source (the cylinder) in the next module, and for this diffusion-dominant system (Peclet number $Pe = RePr = 2.4$), the heating flux from the next cylinder can reach a relatively long distance even against the flow direction. As for the results from the DM or ST approaches for both CWT and SHF boundary conditions, one can see again excellent agreement exists in Fig. 3.9, and no apparent difference can be spotted. The decaying rate λ_L value is 3.88554×10^{-3} from the DM approach, and 3.88533×10^{-3} from the ST approach. Such a nearly perfect match indicates that both

the DM and ST approaches can produce reliable results for simulating developed periodic thermal flows.

A similar comparison is performed in Fig. 3.10, which displays the distributions over the simulation domain between the ST and DM simulations with CWT (a and b) and SHF (a' and b') wall conditions. Again the difference magnitude is relatively small ($10^{-6} \sim 10^{-5}$), suggesting that both the DM and ST methods can be utilized to simulate incompressible periodic thermal flows. The temperature difference seems to vary more smoothly in space for the CWT system than the SHF system; however, the detailed mechanism responsible for this observation is out of the capacity of the authors.

3.4 Summary and Concluding Remarks

We have examined the periodic relationships in flow and temperature fields for fully developed periodic incompressible thermal flows with CWT and SHF boundary conditions, and proposed two LBM implementations (the ST and DM approaches) for such flow situations. The methods have then been tested carefully in several simulations by comparing our LBM results to those from analytical solutions, previous publications, and our own LBM simulations using different numerical techniques. The good performance suggests that our methods could be useful for future LBM thermal simulations.

Since the purpose of this chapter is to propose these LBM methods for periodic thermal flows, we have limited our formulations and demonstrations to 2D, laminar, and steady flow situations. Extending these methods to other LBM models (other lattice structures, three-dimensional, multiple-relaxation-time models, or even turbulent LBM models) should be relatively straightforward. Other alternative thermal LBM models [61, 17, 41] can also be adopted to solve the thermal field. In addition, although the systems considered in this chapter are relatively simple, more complex geometric shapes and boundary conditions (for example, different heat flux magnitudes at different wall locations) can be readily simulated by our methods. For more

realistic situations such as unsteady and turbulent periodic thermal flows, some numerical strategies [15, 59, 55] used in previous computational fluid dynamics (CFD) studies can be considered.

For the two numerical schemes to implement the periodic features of temperature in LBM, the ST approach has been typically used in traditional CFD studies, and certainly can also be adopted in LBM. On the other hand, the DM approach is unique for LBM with some computational advantages. In the DM method, extra calculations are only required for the thermal distributions crossing the periodic inlet/outlet boundaries; but in the ST method, an extra term has to be calculated for all distributions and at all lattice nodes. Furthermore, for systems with CWT boundaries, the ST approach also needs to calculate the streamwise derivative of temperature ($\partial\bar{\theta}/\partial x$ in Eq. 3.13), and this could further increase the computational demand. The method in Eq. (3.16) to calculate the decaying rate λ_L does not require a volumetric integration of temperature over the entire computational domain, and thus it could also be useful for improving the computational efficiency for other CFD methods.

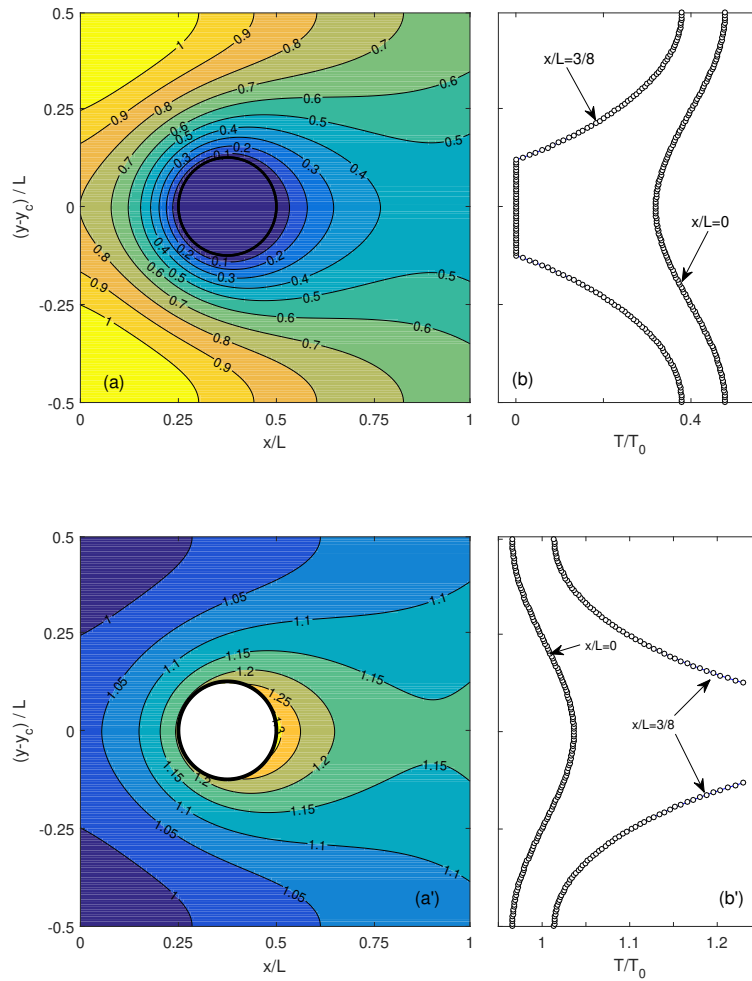


FIGURE 3.9: Result comparison of the simulations for the thermal flows around cylinder using the DM or ST approaches for the CWT (a and b) and SHF (a' and b') wall conditions. In the temperature fields (a and a'), the color patches are from the DM approach, and the isotherm lines are from the ST approach. The temperature profiles at $x/L = 0$ and $3/8$ (indicated by labels) are displayed in (b) and (b'), with the symbols from the DM approach and curves from the ST approach.

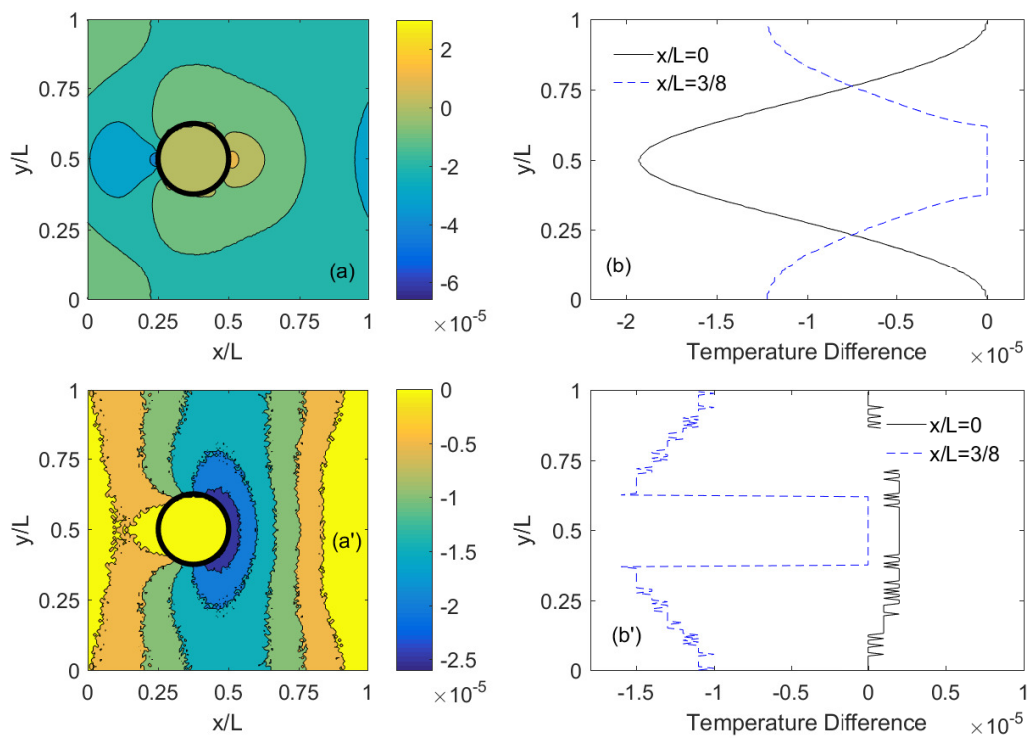


FIGURE 3.10: Distributions of temperature difference between simulations using the ST and DM approaches for the CWT (a and b) and SHF (a' and b') wall conditions. The temperature difference from panels (a) and (a') at two representative locations $x/L = 0$ (black solid line) and 3/8 (blue dashed line) are shown in (c).

Re	Center Velocity u_x^c		Friction Factor f		Nusselt Number Nu		
	Ref. [54]	this work	Ref. [54]	Ref. [47]	this work	Ref. [47]	this work
25	0.619	0.596	1.483	1.294	1.871	1.469	4.395
100	0.955	0.929	0.458	0.415	0.725	0.455	4.559

TABLE 3.1: Comparison of the center velocity u_x^c , friction factor f and Nusselt number Nu from our LBM simulations to those from previous publications. The data of Ref. [47] are approximated using linear interpolation or extrapolation based on the converted values from Ref. [54].

Chapter 4

Rectangular LBM For Anisotropic Flows ¹

4.1 Introduction

In many natural and engineering situations, fluid flows may exhibit nonuniform, inhomogeneous, and anisotropic features. One obvious example could be the flows through isotropic porous media with different permeability coefficients in different directions [31]. Flows in rectangular or elliptical channels with relatively large aspect ratios have a much abrupt variation in velocity in the narrower transverse direction than in the wider transverse direction. Also, for flows through channels with varying cross-sections, the cross-section variation may occur over a distance much longer than the cross-section dimensions, and thus the flow field experiences large gradients in the cross-sectional plane and small gradients in the streamwise direction. To simulate such flow systems, classical numerical methods, such as the finite-difference and finite-volume methods, typically adopt nonuniform meshes with a finer spatial resolution in the large velocity gradient direction to balance the simulation accuracy and efficiency [64]. However, for the lattice Boltzmann method (LBM), the flow anisotropy poses a challenge, since the general LBM requires an isotropic lattice structure and a uniform lattice grid [72]. To achieve a good accuracy

¹The contents in this Chapter had been published in *International Journal of Modern Physics C* (30: 1941001, 2019). Minor revisions have been made in this Chapter.

in representing the velocity variation in the large gradient direction, finer meshes are required in all directions although it might not be necessary.

To address this disadvantage in LBM, several attempts have been reported in the literature for rectangular or cuboid lattice structures. He et al. [23] proposed an interpolation scheme, where the regular LBM collision and propagation steps were performed on a nonuniform mesh grid. The post-propagation distributions at the nonuniform grid points were obtained by interpolations. Bouzidi et al. [5] modified the transformation matrix and equilibrium distribution functions of the multiple-relaxation-time (MRT) LBM method for two-dimensional (2D) rectangular lattice grids. Several coupling parameters were also introduced in the equilibrium functions and their values were determined from the stability analysis of the linearized dispersion equation. On the other hand, Zhou [84, 85] modified the equilibrium distribution functions and added extra forcing terms to the lattice Boltzmann equation so that the Navier-Stokes equation can be recovered from the Chapman-Enskog analysis. Another interesting approach was proposed by Hegele et al. [24], where extra lattice velocities were added and the lattice weight coefficients were also adjusted. Zong et al. [86] pointed out that the methods by Bouzidi et al. [5] and Zhou [84, 85] were not fully consistent to the Navier-Stokes equation, and a new MRT scheme for rectangular lattice grids was developed by introducing a more flexible coupling between the energy and normal stress moments. Peng et al. [53] then generalized Zong et al.'s method by incorporating stress components in the equilibrium moments to offset the anisotropy in the stress tensor for a rectangular lattice; and this method was also extended to three-dimensional (3D) situations by Wand et al. [67]. In general, relatively complicated mathematical formulations are involved in these rectangular or cuboid lattice models.

In this chapter, we propose an alternative approach for such systems. Different from previous methods discussed above which focused on modifications of the LBM algorithm and lattice structures, we first perform an appropriate coordinate and velocity transform on the system to be simulated to reduce or remove the physical anisotropy, and then the general LBM algorithms with regular isotropic lattice grids

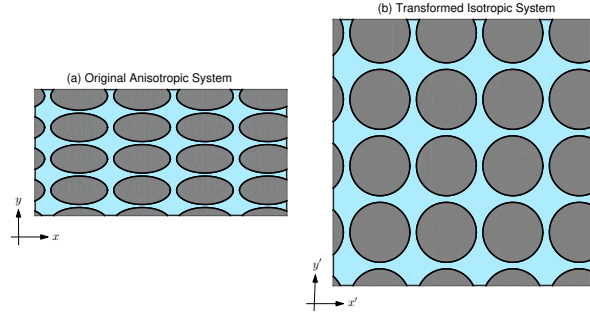


FIGURE 4.1: Schematic illustration of (a) an anisotropic flow system and (b) the transformed system with an approximate spatial isotropy.

can be applied to solve the transformed Navier-Stokes equations. The rest of the chapter is organized as follows: In Sect. 4.2, we introduce the key idea of the coordinate and velocity transform and derive the transformed governing equations that can be solved by general LBM methods. In Sect. 4.3, we investigate the performance of our method by simulating several model systems, including the straight channel flow, the Taylor-Green vortex, the wavy channel flow, and the flow through an array of elliptical particles. In particular, concerns on the numerical stability and accuracy are discussed and possible remedies are proposed in Sect. 4.3.5. At the end, summary and concluding remarks are presented in Sect. 4.4.

4.2 Coordinate and Velocity Transform to Reduce System Anisotropy

We take the system illustrated in Fig. 4.1a as an example of anisotropic flow systems. Due to particular solid object shape and packing configuration, the flow through this structure is highly anisotropic. In order to simulate this anisotropic flow accurately with general LBM methods, a fine, uniform grid mesh is necessary, although the flow velocity variation in the x direction is relatively gentle. To reduce or remove the spatial anisotropy, we would transform the system coordinates (x, y) as well as flow properties, (u, v) for the flow velocity and P for the pressure, to a new system via:

$$x' = x/a_x, \quad y' = y/a_y; \quad u' = u/a_x, \quad v' = v/a_y; \quad P' = P. \quad (4.1)$$

Here we use the superscript $'$ to denote the properties for the transformed system. The parameters a_x and a_y are the scaling coefficients in the x and y directions, respectively; and their values can be adjusted to achieve a more isotropic system after the transform. For example, using $a_x = 1$ and $a_y = 0.5$, the system in Fig. 4.1a is converted to that in Fig. 4.1b with the y direction being extended, and the new system is approximately isotropic in x and y directions. Associated with this transform, the governing continuity and Navier-Stokes equations for the original physical system

$$\frac{\partial u}{\partial x} + \frac{\partial v}{\partial y} = 0 \quad (4.2)$$

$$\frac{\partial u}{\partial t} + u \frac{\partial u}{\partial x} + v \frac{\partial u}{\partial y} = -\frac{\partial P}{\partial x} + \nu \frac{\partial^2 u}{\partial x^2} + \nu \frac{\partial^2 u}{\partial y^2} + g_x \quad (4.3)$$

$$\frac{\partial v}{\partial t} + u \frac{\partial v}{\partial x} + v \frac{\partial v}{\partial y} = -\frac{\partial P}{\partial y} + \nu \frac{\partial^2 v}{\partial x^2} + \nu \frac{\partial^2 v}{\partial y^2} + g_y \quad (4.4)$$

also change to

$$\frac{\partial u'}{\partial x'} + \frac{\partial v'}{\partial y'} = 0 \quad (4.5)$$

$$\frac{\partial u'}{\partial t} + u' \frac{\partial u'}{\partial x'} + v' \frac{\partial u'}{\partial y'} = -\frac{1}{a_x^2} \frac{\partial P'}{\partial x'} + \frac{\nu}{a_x^2} \frac{\partial^2 u'}{\partial x'^2} + \frac{\nu}{a_y^2} \frac{\partial^2 u'}{\partial y'^2} + \frac{g_x}{a_x}. \quad (4.6)$$

$$\frac{\partial v'}{\partial t} + u' \frac{\partial v'}{\partial x'} + v' \frac{\partial v'}{\partial y'} = -\frac{1}{a_y^2} \frac{\partial P'}{\partial y'} + \frac{\nu}{a_x^2} \frac{\partial^2 v'}{\partial x'^2} + \frac{\nu}{a_y^2} \frac{\partial^2 v'}{\partial y'^2} + \frac{g_y}{a_y}. \quad (4.7)$$

Here (g_x, g_y) are the body force density and ν is the kinematic fluid viscosity for the original system. It is interesting to notice that the new continuity equation Eq. (4.5) is identical to its original version Eq. (4.2), except with the superscript $'$ added to velocity and coordinate variables. The transformed Navier-Stokes equations Eqs. (4.6) and (4.7) are also similar to the original equations. Since the general LBM algorithm is developed to solve the standard Navier-Stokes equations, here we rewrite the transformed Navier-Stokes equations to:

$$\frac{\partial u'}{\partial t} + u' \frac{\partial u'}{\partial x'} + v' \frac{\partial u'}{\partial y'} = -\frac{\partial P'}{\partial x'} + \nu' \frac{\partial^2 u'}{\partial x'^2} + \nu' \frac{\partial^2 u'}{\partial y'^2} + g'_x, \quad (4.8)$$

$$\frac{\partial v'}{\partial t} + u' \frac{\partial v'}{\partial x'} + v' \frac{\partial v'}{\partial y'} = -\frac{\partial P'}{\partial y'} + \nu' \frac{\partial^2 v'}{\partial x'^2} + \nu' \frac{\partial^2 v'}{\partial y'^2} + g'_y; \quad (4.9)$$

where

$$g'_x = \frac{g_x}{a_x} + \left(1 - \frac{1}{a_x^2}\right) \frac{\partial P'}{\partial x'} + \left(\frac{\nu}{a_x^2} - \nu'\right) \frac{\partial^2 u'}{\partial x'^2} + \left(\frac{\nu}{a_y^2} - \nu'\right) \frac{\partial^2 u'}{\partial y'^2}, \quad (4.10)$$

$$g'_y = \frac{g_y}{a_y} + \left(1 - \frac{1}{a_y^2}\right) \frac{\partial P'}{\partial y'} + \left(\frac{\nu}{a_x^2} - \nu'\right) \frac{\partial^2 v'}{\partial x^2} + \left(\frac{\nu}{a_y^2} - \nu'\right) \frac{\partial^2 v'}{\partial y'^2}, \quad (4.11)$$

and ν' is the artificial viscosity for the transformed system. This equation system can now be solved by a general LBM algorithm using square lattice models, and details on LBM can be found in the literature [17]. In practice, by selecting $\nu' = \nu/a_x^2$ or $\nu' = \nu/a_y^2$, we can eliminate one second-order partial derivative term in Eqs. (4.10) and (4.11). Also we typically only need to scale the system in one direction, for example in Fig. 4.1 we have $a_x = 1$ and $a_y = 0.5$; and thus one of the pressure gradient terms in Eqs. (4.10) and (4.11) will disappear. The reminding partial differential terms in Eqs. (4.10) and (4.11) can be estimated by the central finite difference approximation.

4.3 Simulations and Discussions

Next we conduct several 2D simulations to verify our method and to examine its performance. The general SRT LBM method with the square D2Q9 lattice structure [78] are used in these calculations. The midpoint bounce-back boundary method [75] is adopted for the wall boundaries, and the general periodic boundary condition is applied at domain boundaries [17, 78]. The artificial body forces g'_x and g'_y are incorporated using the method proposed by Guo et al. [20]. Since the velocity variation mainly occurs in the transverse direction, we have $a_x=1$ for all the simulations in this work. The simulation results are then analyzed and potential remedies to improve the numerical accuracy and stability are proposed for future studies.

4.3.1 Poiseuille Flow in Straight Channel

We first test our method for the Poiseuille flow through a straight channel, which, in spite of its simplicity, has served as a common benchmark for new LBM models

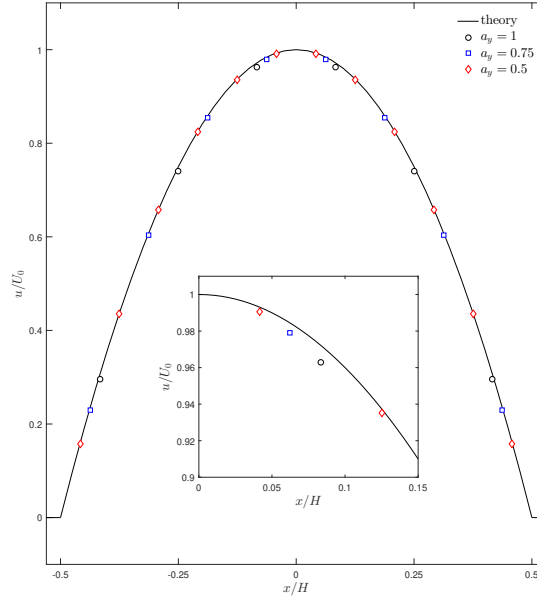


FIGURE 4.2: Simulated velocities for the straight channel flow using our rectangular LBM model with different a_y values. For comparison, the theoretical profile from fluid mechanics is also displayed as the solid line. The inset enlarges the results near the channel centerline for a better comparison of the calculated and theoretical velocities.

and boundary conditions. It is true that a rectangular lattice grid is not necessary for this simple flow through a straight, uniform channel, since a single column of lattice nodes across the channel width is adequate if the periodic boundary condition is implemented appropriately in the streamwise direction. However, analytical solutions for anisotropic flows are rare, and the Poiseuille flow is considered as the first system to confirm the validity of our method. Here we take a $L = 100$ long segment of a $H = 6$ wide channel as the physical domain, in which the flow field is to be solved. The driving force density along the channel is $g_x = 10^{-8}$ and the fluid viscosity is $\nu = 1/6$. All these properties are given as non-dimensional values. The Reynolds number $Re = U_0 H / \nu$ is 9.72×10^{-6} , and the nominal velocity here is taken as $U_0 = g_x H^2 / 8\nu$. Three calculations are carried out for this same system: $a_y = 1$, $a_y = 0.75$, and $a_y = 0.5$. While holding the total lattice number along the $L = 100$ length constant at 100, we have more lattice rows across the channel as we decrease a_y (i.e., as the space being stretched in the transverse direction), and thus a better representation of the velocity profile across the channel should be expected. Fig. 4.2 shows the calculated velocity profiles at these three different scaling levels

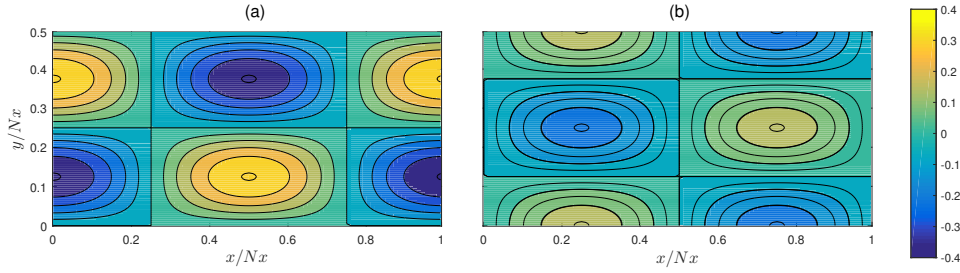


FIGURE 4.3: Comparisons of the simulated and analytical velocity distributions (velocity u in a and velocity v in b) for the Taylor-Green vortex flow with $L_x = 100$ and $L_y = 50$. The background color patches are from our LBM calculation and the black contour lines are from the analytical solution Eqs. (4.12-4.13).

(symbols), in comparison to the theoretical parabolic profile (solid line) from fluid mechanics. It can be seen there, as a_y decreases, we can include more lattice points across the channel width: 6 points for $a_y = 1$, 8 points for $a_y = 0.75$, and 12 points for $a_y = 0.5$. The improvement in agreement between LBM results and fluid mechanics theory is apparent in the inset of Fig. 4.2, and this is confirmed by the calculated relative errors: 1.2675×10^{-2} for $a_y = 1$, 7.1311×10^{-3} for $a_y = 0.75$, and 3.1696×10^{-3} for $a_y = 0.5$. Actually, these error values are identical to those from the regular LBM simulations (i.e., $a_x = a_y = 1$) with different channel width $H = 6, 8$, and 12 . This identity suggests that our method has not introduced extra inaccuracy for these straight channel flows. This is reasonable by considering the following facts. First, for this particular system, the LBM algorithm can reproduce the parabolic profile of velocity u exactly [39, 50], the velocity $v = 0$ and the pressure P is constant in the channel. Accordingly, the estimates of the partial differential terms in Eqs. (4.10) and (4.11) are exact with no extra errors from the central finite difference approximations. Although no downgrade in accuracy, further decrease in a_y causes numerical instability and the simulation does not converge. This issue will be discussed in Sect. 4.3.5.

4.3.2 Taylor-Green Vortex

The Taylor-Green vortex is an unsteady flow consisting of a series of decaying vortices in a rectangular periodic domain. This flow has often been used to test the performance of numerical methods including several precious rectangular LBM models

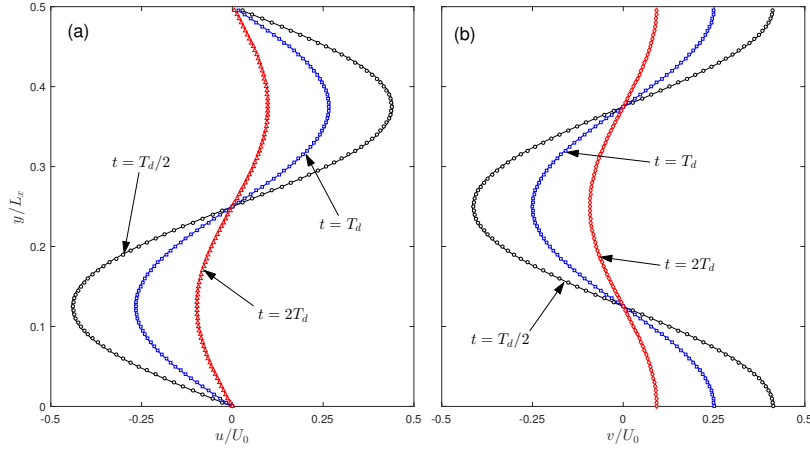


FIGURE 4.4: Comparisons of the simulated (symbols) and analytical (lines) velocity profiles (velocity u in a and velocity v in b) at $t = T_d/2$, T_d , and $2T_d$ along the vertical line $x = 0.125L_x$ for the Taylor-Green vortex flow.

[84, 24, 53]. The analytical solution of the decaying flow is given by [24]

$$u(x, y, t) = -U_0 \cos(k_x x) \sin(k_y y) e^{-t/T_d}, \quad (4.12)$$

$$v(x, y, t) = \frac{k_x}{k_y} U_0 \sin(k_x x) \cos(k_y y) e^{-t/T_d}; \quad (4.13)$$

where $k_x = 2\pi/L_x$ and $k_y = 2\pi/L_y$ are, respectively, the wave numbers in the x and y directions for the periodic rectangular domain of lengths L_x and L_y . U_0 is a parameter for the initial velocity magnitude, and the characteristic decay time is $T_d = 1/\nu(k_x^2 + k_y^2)$. We first consider the case with $L_x = 100$ and $L_y = 50$. By setting $a_x = 1$ and $a_y = 0.5$, this rectangular system is then mapped to a 100×100 square domain where the regular D2Q9 lattice structure can be applied. In our calculation, we have $U_0 = 0.0001$ and $\nu = 1/6$. The calculated velocity distributions at $t = T_d$ are displayed in Fig. 4.3, where an excellent agreement can be noticed between our simulation result and the analytical solution. More quantitatively, in Fig. 4.4, we plot the velocity profiles along a vertical line $x = 0.125L_x$ at three representative time instances $t = T_d/2$, T_d , and $2T_d$. The location $x = 0.125L_x$ is selected according to the particular velocity distributions in Fig. 4.3: The velocity $u = 0$ along $x = 0.25L_x$ and $0.75L_x$, and velocity $v = 0$ along $x = 0$, and $0.5L_x$. By plotting the profiles along $x = 0.125L_x$, we can see the spatial variation features for both u and v . We also

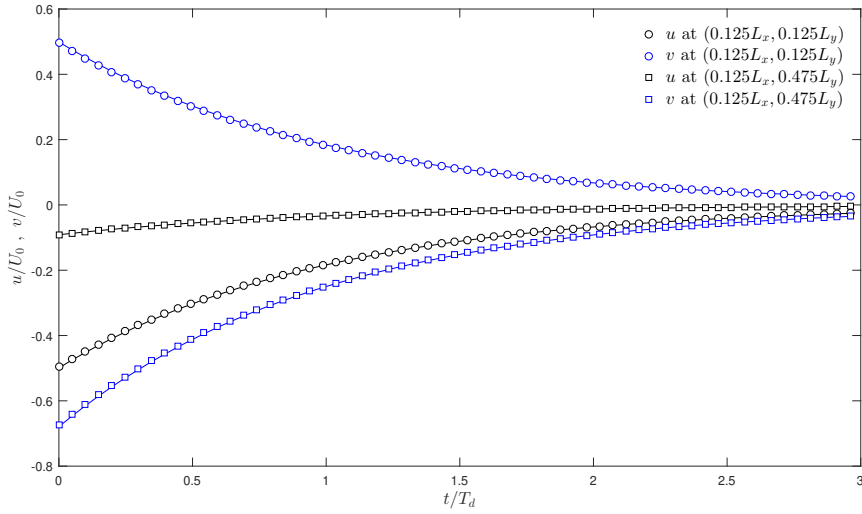


FIGURE 4.5: Comparisons of the simulated (symbols) and analytical (lines) velocities (black for u and blue for v) at two locations $(0.125L_x, 0.125L_y)$ (circles) and $(0.125L_x, 0.475L_y)$ (squares) for the Taylor-Green vortex flow.

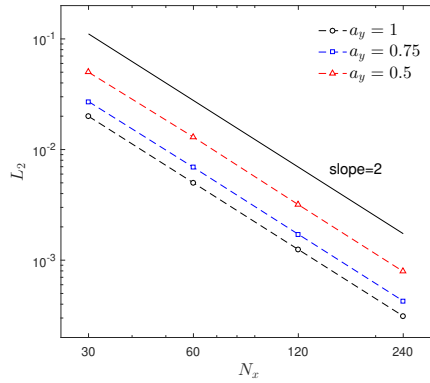


FIGURE 4.6: The velocity relative errors for the Taylor-Green vortex flow simulations with different aspect ratios and lattice mesh resolutions. The solid black line is plotted to indicate the second order convergence rate of our method.

examine the temporal decay behavior of the vortex flow by comparing the velocities at two representative locations $(0.125L_x, 0.125L_y)$ and $(0.125L_x, 0.475L_y)$ in Fig. 4.5. Again our LBM results match the theoretical solution well in these comparisons.

To evaluate the numerical accuracy more explicitly, following previous studies [24, 86], we perform a series of calculations with different aspect ratios and lattice resolutions. All the calculations are conducted over square $N_x \times N_x$ D2Q9 lattice domains. Therefore, with $a_x = 1$ and different a_y , the physical dimensions for the Taylor-Green vortex are $L_x = N_x$ and $L_y = a_y N_x$. The relative velocity error is defined as

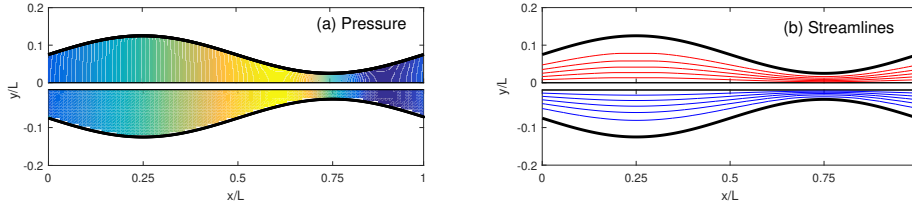


FIGURE 4.7: Comparisons of (a) pressure distributions and (b) streamlines for the wavy channel flow from (top) the fine mesh LBM simulation over square lattice grids and (b) the $a_y = 0.75$ simulation using our rectangular model.

$L_2 = [\sum |\mathbf{u}_n - \mathbf{u}_a|^2 / \sum |\mathbf{u}_a|^2]^{1/2}$ [24], where the subscripts a and n are adopted to denote, respectively, the numerical and analytical velocities, and both summations cover all $N_x \times N_x$ lattice nodes. Three aspect ratios ($a_y = 1, 0.75$, and 0.5) and four mesh resolutions ($N_x = 30, 60, 120$, and 240) are considered. Since the Taylor-Green flow is unsteady and the relative error L_2 is also changing with simulation time, we collect the L_2 values for all these simulations at a same normalized time $t/T_d = 1$. The log-log graph Fig. 4.6 shows that the numerical errors from our method is reducing with the mesh resolution increase at a second order convergence rate. When fitting the data points in Fig. 4.6 with straight lines, the slopes are 1.9980 for $a_y = 0.5$, 1.9978 for $a_y = 0.75$, and 2.0004 for $a_y = 1$. Although the second order convergence of the original LBM method is preserved, the absolute L_2 values increase as the aspect ratio a_y decreases. We attribute this decreasing accuracy with a_y to the finite difference approximations in our method, and more discussions will be presented next in Sect. 4.3.5. Similar accuracy-aspect dependency has also been reported for other rectangular LBM models [23, 86].

4.3.3 Flow through Wavy Channel

To introduce anisotropy to the flow field, here we consider a wavy channel with its width $H(x)$ varying symmetrically according to a sinusoidal function: $H(x) = H_{avg} + 2A \sin(\frac{2\pi x}{L})$, where H_{avg} is the average width over a period length L , and A is the wavy amplitude. The maximum width $H_{max} = H_{avg} + 2A$ occurs at $x = L/4$ and the minimum $H_{min} = H_{avg} - 2A$ occurs at $x = 3L/4$. Please refer Fig. 4.7 for the system geometry. Here we take $L = 100$, $H_{avg} = 15$, and $A = 5$, all nondimensional. The minimum channel width is $H_{min} = 5$. As in the previous section, the flow

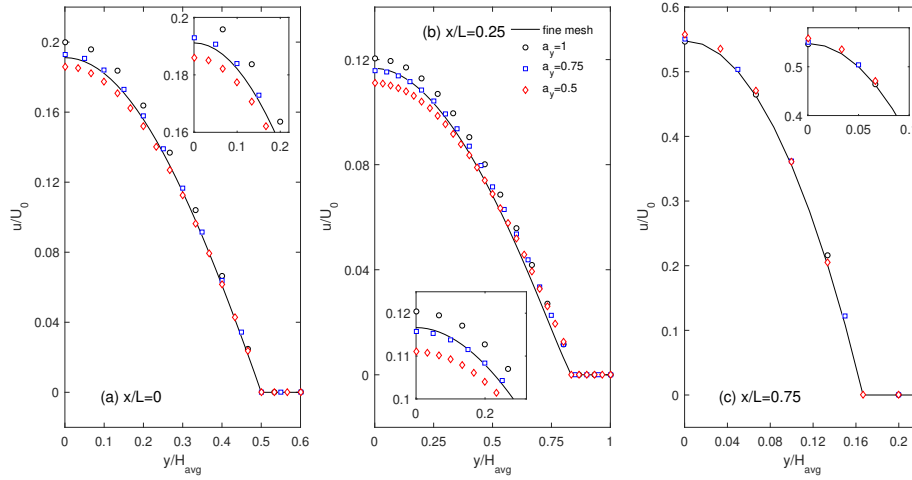


FIGURE 4.8: Comparisons of simulated velocity profiles for the way channel flow from our rectangular LBM model (symbols) and the fine mesh general LBM method (solid lines) at three streamwise locations. The inset in each panel enlarges the curve and symbols in the maximum velocity region near the centerline $y = 0$ for a better comparison.

is generated by a uniform body force $g_x = 10^{-8}$ and the fluid viscosity is $\nu = 1/6$. Considering the structure periodicity, we only include one wavelength long segment of the channel in our calculations. Again three sets of calculations are carried out with $a_y = 1, 0.75$, and 0.5 , all with 100 lattice nodes over the variation period L . Since the analytical solution for this flow is not available, a separate simulation is performed using the regular LBM method with the mesh resolution quadrupled (i.e., 400 lattice nodes over the wavelength). This 400-lattice calculation will be referred as the *fine mesh* simulation and its result will serve as the comparison standard.

Fig. 4.7 shows the pressure distributions (a) and streamlines (b) from the fine mesh simulation (top) in comparison to those from the $a_y = 0.75$ simulation (bottom). There is no apparent difference observed. A high pressure is built up at $x/L \sim 0.6$ due to the large flow resistant in the narrow section at $x/L = 0.75$; and accordingly the low pressure occurs at $x/L \sim 0.85$ after the neck section. The streamlines in Fig. 4.7b clearly indicates the high velocity at the neck segment $x/L \sim 0.75$ and the slow flow in the wide section $x/L \sim 0.25$, for the mass conservation principle. More quantitatively, we plot the profiles of the axial velocity u from these simulations across the channel at different locations along the channel in Fig. 4.8: (a) the mean-width location $x/L = 0$, (b) the maximum-width location $x/L = 0.25$, and

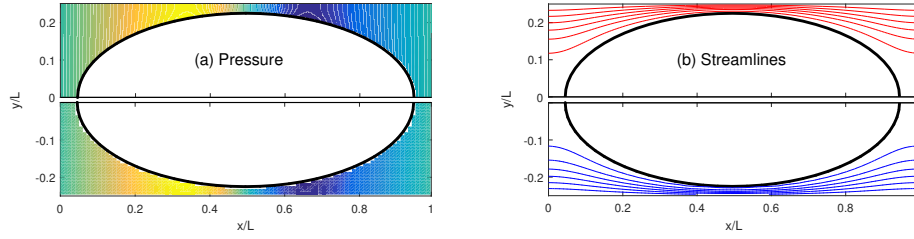


FIGURE 4.9: Comparisons of (a) pressure distributions and (b) streamlines for the flow through the elliptical particle array from (top) the fine mesh LBM simulation over square lattice grids and (b) the $a_y = 0.758$ simulation using our rectangular model.

(c) the minimum-width location $x/L = 0.75$. The results from our rectangular LBM model with different ratio a_y are displayed as symbols, and that from the fine mesh simulation is shown as black lines. For the system symmetry about the centerline $y = 0$, we only show the velocity profiles in the $y \geq 0$ region. The velocity magnitude is normalized with the maximum velocity U_0 through a uniform, H_{avg} -wide channel according the Poiseuille law, i.e., $U_0 = g_x H_{avg}^2 / 8\nu$. The Reynolds number $Re = U_0 H_{avg} / \nu$ is 1.5×10^{-4} . It is interesting to see that the best agreement between the rectangular-LBM results and the fine mesh simulation is observed at neck $x/L = 0.75$, and the worst at the maximum width $x/L = 0.25$. Please note this observation should not be attributed to our rectangular model, since the calculation with $a_y = 1$ (black circles in Fig. 4.8) is simply a regular LBM simulation over a uniform square lattice grid, just with a four-fold lower resolution compared to the fine mesh simulation (black lines in Fig. 4.8). With the ratio a_y decreases from 1 to 0.75 and then 0.5, more lattice nodes are employed in the y -direction, and intuitively a better accuracy is expected (as we see in the straight channel simulations above). However, it seems here $a_y = 0.75$ (blue squares in Fig. 4.8) yields the most accurate velocity, and the lower value $a_y = 0.5$, although with more lattice nodes (i.e., a finer mesh) in the transverse direction, results in a reduced accuracy. Please see Figs. 4.8a and b for this observation, and it will be discussed next in Sect. 4.3.5.

4.3.4 Flow through a Model Anisotropic Porous Medium

To further illustrate the application of our rectangular LBM model and also to verify the different effects of a_y on numerical accuracy observed in the straight and wavy

channel simulations, at last we simulate the system in Fig. 4.1a. This system consists of identical elliptical particles arranged periodically in both the x and y directions, and the flow is generated by a body force g_x . This system, in spite of its simplicity, can be considered as a model of flows through anisotropic porous media which are frequently encountered in many natural and engineering situations [31]. In our simulations, we consider a 2D domain of length $L = 100$ and width $H = 50$ as the periodic unit. The elliptical particle is located at the domain center and has semi-axes of $a = 0.45L = 45$ in the x direction and $b = 0.45H = 22.5$ in the y direction. Periodic boundary conditions are applied in both directions. As a result, the minimum gap width between two particles at $x = L/2$ is $H - 2b = 5$. Please refer Fig. 4.9 for the system geometry. For this system, the minimum a_y value for our current program is $50/93=0.538$, where 100 and 93 lattice nodes, respectively, are utilized in the x and y directions. Similar to previous systems, three different a_y ratios are tested: $a_y = 1$ (100×50 D2Q9 lattice mesh), $a_y = 0.758$ (100×66 D2Q9 lattice mesh), and $a_y = 0.538$ (100×93 D2Q9 lattice mesh). Again a fine mesh simulation with a 400×200 square mesh is performed for comparison. The calculation results are displayed in Figs. 4.9 and 4.10. The agreement in pressure distributions and streamline patterns in general are satisfactory (Fig. 4.9). The higher fluid pressure is established before and the lower pressure after the narrowest gap segment at $x/L \sim L/2$. The fastest flow velocity, indicated by the small distance between streamlines, is also observed in the minimum gap section due to the mass conservation. Velocity profiles at three streamwise locations are plotted in Fig. 4.10 for a detailed examination of the simulation accuracy: (a) $x/L = 0$, (b) $x/L = 0.25$, and (c) $x/L = 0.5$. The nominal velocity U_0 here is taken as the maximum velocity in a straight channel with the minimum gap width: $U_0 = g_x(H - 2b)^2/8\nu$. The Reynolds number $Re = U_0b/\nu$ is 2.5×10^{-5} . Here again we see the best agreement occurs at the narrowest gap position $x/L = 0.5$, and the more apparent deviations from the fine mesh simulation are noticed at $x/L = 0$ and 0.25 . Similar to those observed in Fig. 4.8 for the wavy channel simulations, the moderate $a_y = 0.758$ (blue squares) yields a better accuracy than the $a_y = 1$ (black circles) and $a_y = 0.538$ (red diamonds). The reverse effect of a higher resolution of $a_y = 0.538$ on the result accuracy will be analyzed next.

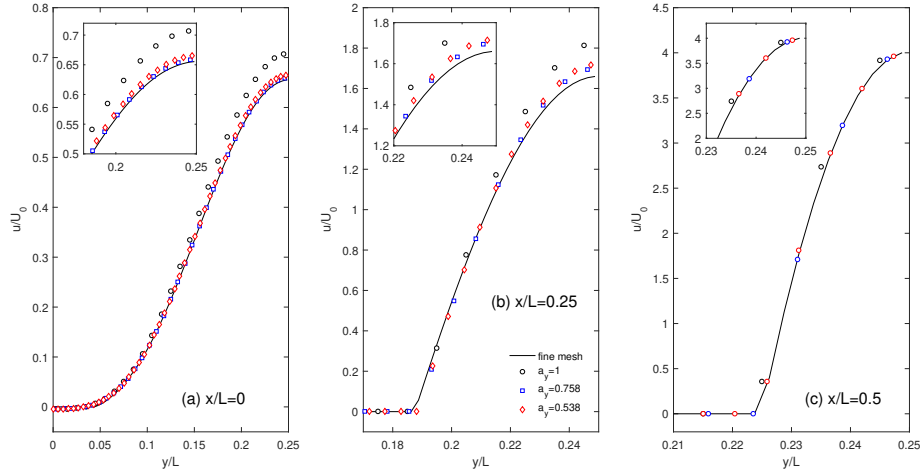


FIGURE 4.10: Comparisons of simulated velocity profiles for the elliptical particle array flow from our rectangular LBM model (symbols) and the fine mesh general LBM method (solid lines) at three streamwise locations. The inset in each panel enlarges the curve and symbols in the maximum velocity region near the top domain edge $y/L = 0.25$ for a better comparison.

4.3.5 Stability and Accuracy Analysis and Discussions

The difference in our rectangular model from the classical LBM algorithm using square lattices is the artificial force terms in Eqs. (4.10) and (4.11); therefore we should focus on these terms when exploring the potential causes of the stability and accuracy concerns noticed above. We first look at the numerical instability caused by a small a_y value. As mentioned above, the minimum value for a_y is 0.5 for the straight and wavy channel flows and it is 0.538 for the flow through elliptical particle array. Please note in all these calculations, we have $a_x = 1$ as the typical practice in such rectangular LBM models [5, 85, 84, 24, 86, 67]. The effect of a_y on the force term g'_y in Eq. (4.11) is relatively insignificant: g_y/a_y increases when a_y decreases, however, in a gentle fashion unless a_y becomes extremely small, the pressure gradient term $\left(1 - \frac{1}{a_y^2}\right) \frac{\partial P'}{\partial y'}$ should not be a major concern either since the pressure variation in the transverse direction is zero in the straight channel system and small in the wavy channel and ellipse particle systems (see Figs. 4.7a and 4.9a), and the last term $\left(\frac{\nu}{a_y^2} - \nu'\right) \frac{\partial^2 v'}{\partial y'^2}$ should also be unsubstantial considering the zero or small magnitude of the transverse velocity v' . On the other hand, for the force term g'_x in Eq. (4.10), we have the first two terms on the RHS disappear when $a_x = 1$, as well as the third term vanishes when we select $\nu' = \nu$, as we do in our simulations. the only term

left over on the RHS of Eq. (4.10) is the last term $\left(\frac{\nu}{a_y^2} - \nu'\right) \frac{\partial^2 u'}{\partial y'^2}$. The denominator a_y^2 plus the large velocity gradient in the transverse direction $\frac{\partial^2 u'}{\partial y'^2}$ in our simulated systems together can result in a relatively large body force term for our rectangular LBM calculation, and the large body force has been well recognized as a major cause to LBM simulation instability. Numerical experiments are conducted to confirm this analysis: we remove the last term in Eq. (4.10) and the simulations can remain stable with lower a_y values. We are aware that the results using this incomplete force term are not physically meaningful, and our purpose here is purely to numerically verify that the last term in g'_x is indeed the main cause of the simulation instability for our rectangular model.

We now turn our attention to the result accuracy. For the straight channel flow, the pressure P' is constant (the flow is driven by a constant body force), the transverse velocity $v' = 0$, and the streamwise velocity u' is constant in the x direction. In such a situation, the only non-zero partial derivative term in Eqs. (4.10) and (4.11) is $\frac{\partial^2 u'}{\partial y'^2}$. It has been shown that, for straight channel flows, the general LBM algorithm is equivalent to a central finite difference representation for the flow velocity [50, 39], and the velocity profile in a straight channel indeed follows a parabolic curve. In addition, we use the finite difference scheme to estimate the partial differential terms in our rectangular LBM calculations. With all these aspects considered, it is not surprising to see the increasing accuracy with finer resolutions for the straight channel flow. However, these idealized conditions do not present for other more complex flows like those in the wavy channel and particle array systems. A smaller a_y value, on one side, increase the number of lattice nodes in the transverse direction and thus a better representation of the velocity variation can be expected; on the other hand, the inevitable errors from the finite difference approximations for the partial derivative terms are amplified by the smaller denominators a_y^2 . These two factors have opposite influences on the overall numerical accuracy. Apparently, in our simulations of the wavy channel and particle array flows, the former is more predominant as we decrease a_y from 1 to 0.75, and the negative effect from the amplified errors has surpassed the benefit from the finer lattice grid as we further reduce the a_y value.

The low aspect limit ($1/a_y^2$ in our model description, maximum 2 for our simulations) is not unique to our rectangular model; instead, it appears as a common feature for most rectangular LBM models. He et al. [23] reported large grid aspect ratios up to 8; however, the system geometry considered in that study was relatively simple: it was actually a straight rectangular domain with no cross-sectional change. The inlet was set at the left boundary with a width narrower than the channel width. The top aspect ratio from other few rectangular models [5, 85, 84] were similar to ours (~ 2), and the Hegele et al. model [24] could only reach an aspect ratio of 1.5. The largest aspect ratios so far in the literature are those from the recent MRT models in Refs. [86, 53], with values in the range of $4 \sim 5$. The extension to 3D situations of the 2D model in Ref. [53] by Wang et al. [67] seems face the similar instability challenge, and only an aspect ratio of 2 can be reached when simulating the Taylor-Green vortex, although a much larger aspect ratio of 20 can be achieved for straight channel flow. The accuracy reported in these previous studies appears better than that in our wavy channel and elliptical particle array simulations; however, it should be noticed that, unlike the representative anisotropic flows employed here, the systems considered in these previous studies (including the Taylor-Green vortex flow and the lid-driven flow) have relatively regular geometry and are less relevant to the real potential applications of such rectangular models. Bouzidi et al. [5] used the flow through a straight channel with a circular cylinder in the center as the test system; however, the flow anisotropy is not as severe as in our two latter systems. It is not clear how the performance of these existing models would be when working on systems with curved boundaries and realistic, large velocity gradient differences.

All the simulation results presented above are obtained by using the SRT model and the midpoint bounce-back boundary method [75]; however, we have tested the MRT LBM model [17] and the extrapolation boundary method by Guo et al. [19]; and they are not helpful for improving either the stability or accuracy. Based on our above analysis, we re-examine the equations involved, and notice that Eqs. (4.6) and

(4.7) can also be rewritten as

$$\frac{\partial u'}{\partial t} + u' \frac{\partial u'}{\partial x'} + v' \frac{\partial u'}{\partial y'} = -\frac{1}{a_x^2} \frac{\partial P'}{\partial x'} + \nu'_x \frac{\partial^2 u'}{\partial x'^2} + \nu'_y \frac{\partial^2 u'}{\partial y'^2} + \frac{g_x}{a_x}. \quad (4.14)$$

$$\frac{\partial v'}{\partial t} + u' \frac{\partial v'}{\partial x'} + v' \frac{\partial v'}{\partial y'} = -\frac{1}{a_y^2} \frac{\partial P'}{\partial y'} + \nu'_x \frac{\partial^2 v'}{\partial x'^2} + \nu'_y \frac{\partial^2 v'}{\partial y'^2} + \frac{g_y}{a_y}, \quad (4.15)$$

with

$$\nu'_x = \frac{\nu}{a_x^2}, \quad \nu'_y = \frac{\nu}{a_y^2}. \quad (4.16)$$

Now Eqs. (4.14-4.15) make up a Navier-Stokes-like system for flow (u', v') , however, with anisotropic momentum diffusion coefficients ν'_x and ν'_y . Since the major challenge for the practical usefulness of our current rectangular model lies in the artificial force terms in Eqs. (4.10) and (4.11), solving the system (4.14-4.16) directly could be a potential remedy for improving the numerical accuracy and stability. One possible approach could be re-designing the transformation matrix \mathbf{M} in the MRT LBM method to achieve different viscosity coefficients, and thus only the pressure gradient terms will appear in the force terms. Since the pressure variation is much gentler in typical incompressible flows, the calculations would be more stable and accurate. This could be an interesting research topic to pursue in the future. We would like to clarify that the proposed MRT remedy is different from those existing rectangular MRT schemes in Refs. [5, 84, 86, 53]. Those previous MRT methods modified the LBM formulations so that they can use the anisotropic rectangular lattice structure; and our proposed approach will tune the LBM formulations to generate anisotropic momentum diffusion coefficients over the regular, isotropic lattice grids.

4.4 Summary and Concluding Remarks

In this chapter, we have presented a rectangular LBM scheme based on coordinate and velocity transformation for anisotropic flows. The transformed equation system can be solved with the general LBM method over isotropic lattice grids by collecting extra terms into the artificial force terms. Demonstration systems, including the straight and wavy channel flows, the Taylor-Green vortex, and the flow through

an ellipse particle array, have been simulated and the results have been analyzed. Similar to many existing rectangular LBM models, our method suffers numerical instability and inaccuracy at large aspect ratios (i.e., low a_y values). The underlying mechanism for the effects of a_y on the simulation performance has been carefully examined based on the expressions of the artificial force terms. Our analysis reveals that a smaller a_y value increases the magnitudes of the artificial force terms and therefore makes the calculation less stable; On the other hand, a smaller a_y has two opposite effects on the simulation accuracy: the finer mesh to represent the abrupt velocity variation better vs. the amplified finite difference errors in the partial derivative terms. A potential remedy has also been proposed to avoid the finite difference approximations. The method, simulations, and analysis in this study could be of interest for the development of more robust rectangular and cuboid LBM models in the future.

Chapter 5

Conclusion and Further Research

5.1 Conclusion

In Chapter 2, a conjugate interface method on the simulations of convection-diffusion systems between two materials with the interface discontinuity was proposed. The main feature of this method is that the original conjugate problem can be solved as two Dirichlet boundary value systems, as the interfacial scalar values can be obtained via extrapolations from each domain. The algorithm of the method is simple and straightforward. The method has been validated with steady and unsteady systems of flat and circular interfaces. The effects of various parameters (including the interface offset, transport diffusivity, heat capacity ratio, and interfacial conductance) have been investigated. Numerical stability has also been examined, and it is found that the method is stable over larger ranges of key system parameters, including the heat capacity, thermal conductivity, interface conductance, and temporal variation frequency.

In Chapter 3, the periodic relationships in flow and temperature fields for fully developed periodic incompressible thermal flows with CWT and SHF boundary conditions have been examined. Two LBM implementations for the periodic boundary treatment, the ST and DM approaches, have been proposed. The treatments were validated with flat and wavy channels and thermal flows around cylinders. The results suggest that the methods are capable of their purpose and could be used for future thermal flow simulation.

In Chapter 4, a rectangular LBM scheme for anisotropic flows based on coordinate and velocity transformation was proposed. The NS equation was transformed according to the new coordinate, and the extra terms would be merged into the body force term. Then, the system could be solved with the LBM. The method was validated with the straight and wavy channel flows and flow through an ellipse particle array. According to the results, the accuracy and numerical stability were not satisfied. A potential remedy has also been proposed to avoid the finite difference approximations. The method, simulations, and analysis in this study could be of interest for the development of more robust rectangular and cuboid LBM.

5.2 Future Research

Based on the counter-extrapolation method that was introduced in Chapter 2 of this thesis, the following further research is proposed. First, all the validation calculations in Chapter 2 was based on the MRT LBM model with D2Q5 lattice structure. As it was suggested in Chapter 2, this method should be able to extend into other lattice structures easily and can be applied in general for all CFD methods. Therefore, the simulation of the counter-extrapolation method for 3D lattice structures could be finished in the future. Second, all the validations in Chapter 2 were for stationary interfaces (the interfacial boundary has no velocity in its normal direction). Extending the method to LBM models with moving interface should be relatively straightforward. The only issue is that the nodes near boundaries may become a node of another domain as the boundary is moving, and the distribution functions for such nodes may not exist. One possible solution is to get the distribution functions via extrapolations from existing neighboring nodes. In the future, the simulation of the counter-extrapolation method with moving boundary can be considered. In addition, the systems in the validations are relatively simple, and extending the method to systems with more complex geometry shapes and boundary conditions could be considered in the future.

The inlet-outlet treatments for LBM simulations of periodic thermal flow were proposed in Chapters 3. The formulations and validations in Chapters 3 have been

limited to 2D, laminar, and steady flow situations as a concern of simplification. In the future, this work could be continued with other LBM models, such as other lattice structures, MRT models, or even turbulent LBM models. It is also worth noting that there are other alternative thermal LBM models can also be adopted to solve the thermal field, which could be used in future simulations. In addition, although the systems considered in Chapter 3 are relatively simple, more complex geometric shapes and boundary conditions (for example, different heat flux magnitudes at different wall locations) can be readily simulated by the methods proposed in Chapter 3 in future.

As for the rectangular LBM scheme that was proposed in Chapter 4, it is obvious that at its current stage, the method suffers numerical instability and inaccuracy at large aspect ratios. Therefore, dealing with the instability and inaccuracy issue should be the main direction for the future research of this method. One possible future solution is to apply the MRT LBM method and re-design the \mathbf{M} matrix to achieve different viscosity coefficients. By doing this, the pressure gradient terms would appear in the force terms. And because the pressure gradient would be small in incompressible flow, the calculations would be more stable and accurate. The re-designing work of the \mathbf{M} matrix and its validation could be finished in the future.

Appendix A

The Double-Distribution Thermal LBM Model

Here we describe the double-distribution lattice Bhatnagar-Gross-Krook (LBGK) model for thermal flows [22], although other LBM models are available in the literature [61, 17, 41]. Here two sets of density distribution functions are employed: one as f_i for the fluid dynamics and one as h_i for the thermal convection-diffusion equation. The subscript i denotes the lattice direction in which the distributions f_i or h_i move. The evolution of such density distributions can be described by two consecutive steps: the collision step and the propagation or streaming step. In the collision step, the incoming distributions $f_i(\mathbf{x}, t)$ and $h_i(\mathbf{x}, t)$, at a lattice node (\mathbf{x}, t) (\mathbf{x} as the position vector with two coordinate components x and y) from different directions $i = 0, 1, \dots, b - 1$ (b is the total number of lattice velocities of the lattice model employed), mix and then are redistributed into all lattice directions, with mass, momentum, and energy conserved. The new distributions are called post-collision distributions and they are represented as f_i^* and h_i^* in this work. The collision step can be expressed mathematically as

$$f_i^*(\mathbf{x}, t) = f_i(\mathbf{x}, t) - \frac{1}{\tau_f} [f_i(\mathbf{x}, t) - f_i^{eq}(\mathbf{x}, t)] + \delta f_i \quad , \quad (\text{A.1})$$

$$h_i^*(\mathbf{x}, t) = h_i(\mathbf{x}, t) - \frac{1}{\tau_h} [h_i(\mathbf{x}, t) - h_i^{eq}(\mathbf{x}, t)] + \delta h_i \quad . \quad (\text{A.2})$$

The relaxation parameters τ_f and τ_h are related to the fluid kinematic viscosity ν and thermal diffusivity α , respectively; the additional terms δf_i (usually called the forcing term) and δh_i (usually called the source term) can be tuned to recover the correct macroscopic momentum and energy equations. These issues will be discussed below. The fluid density ρ , equilibrium velocity \mathbf{u}^{eq} , and energy scalar A (could be the regular temperature T or its modified counterparts like \tilde{T} , θ , or $\bar{\theta}$, depending on which energy equation to solve by distributions h_i) can be obtained from the density distributions f_i and h_i as

$$\rho = \sum_i f_i, \quad \mathbf{u}^{eq} = \sum_i f_i \mathbf{c}_i / \sum_i f_i, \quad A = \sum_i h_i, \quad (\text{A.3})$$

where \mathbf{c}_i is the i -th lattice velocity. The equilibrium distributions f_i^{eq} and h_i^{eq} can then be calculated from these properties as [17, 11, 10]

$$f_i^{eq} = \omega_i \rho \left[1 + \frac{\mathbf{c}_i \cdot \mathbf{u}}{c_s^2} + \frac{(\mathbf{c}_i \cdot \mathbf{u})^2}{2c_s^4} - \frac{\mathbf{u}^2}{2c_s^2} \right], \quad (\text{A.4})$$

$$h_i^{eq} = \omega_i A \left[1 + \frac{\mathbf{c}_i \cdot \mathbf{u}}{c_s^2} + \frac{(\mathbf{c}_i \cdot \mathbf{u})^2}{2c_s^4} - \frac{\mathbf{u}^2}{2c_s^2} \right]. \quad (\text{A.5})$$

The parameter ω_i is called the lattice weight factor and c_s is the lattice sound speed. In the following propagation step, the post-collision distributions f_i^* and h_i^* will then move to the nearest neighboring lattice node at velocity \mathbf{c}_i over a time step δt :

$$f_i(\mathbf{x} + \mathbf{c}_i \delta t, t + \delta t) = f_i^*(\mathbf{x}, t) \quad ; \quad (\text{A.6})$$

$$h_i(\mathbf{x} + \mathbf{c}_i \delta t, t + \delta t) = h_i^*(\mathbf{x}, t) \quad . \quad (\text{A.7})$$

Now they become the incoming, pre-collision density distributions at node $\mathbf{x} + \mathbf{c}_i \delta t$, and the above described collision-propagation process can be repeated iteratively, till satisfactory results have been obtained.

Appropriate mathematical analysis like the Chapman-Enskog expansion can be performed to the above distribution dynamics, and the following macroscopic equations can be derived [17, 61]:

$$\frac{\partial \rho}{\partial t} + \rho \nabla \cdot \mathbf{u} = 0 \quad , \quad (\text{A.8})$$

$$\frac{\partial \mathbf{u}}{\partial t} + \nabla \cdot (\mathbf{u}\mathbf{u}) = -\frac{\nabla P}{\rho} + \nu \nabla^2 \mathbf{u} + \mathbf{F} \quad , \quad (\text{A.9})$$

$$\frac{\partial A}{\partial t} + \mathbf{u} \cdot \nabla A = \alpha \nabla^2 A + S \quad . \quad (\text{A.10})$$

The fluid properties \mathbf{u} , P , ν , and α are related to the LBM parameters by

$$\mathbf{u} = \mathbf{u}^{eq} + \frac{\mathbf{F}\delta t}{2\rho} \quad , \quad P = c_s^2 \rho \quad , \quad \nu = c_s^2 \left(\tau_f - \frac{1}{2} \right) \delta t \quad , \quad \alpha = c_s^2 \left(\tau_h - \frac{1}{2} \right) \delta t \quad . \quad (\text{A.11})$$

The additional terms δf_i and δh_i in Eqs. (A.1) and (A.2) are related, respectively, to the forcing term \mathbf{F} and source term S in the resulting macroscopic equations Eqs. (A.9) and (A.10) as

$$\delta f_i = \frac{\omega_i \mathbf{F} \cdot \mathbf{c}_i \delta t}{c_i^2} \quad , \quad (\text{A.12})$$

$$\delta h_i = \omega_i S \quad . \quad (\text{A.13})$$

These δf_i and δh_i terms can be conveniently adjusted according to the forcing or source terms in the macroscopic equations to be solved. In our next validation and demonstration simulation examples, we use the simple D2Q9 (2D and $b = 9$) square lattice structure, for which the nine lattice velocities are

$$\mathbf{c}_0 = \begin{pmatrix} 0 \\ 0 \end{pmatrix} \quad , \quad \mathbf{c}_{1-4} = \begin{bmatrix} \cos(i-1)\pi/2 \\ \sin(i-1)\pi/2 \end{bmatrix} \frac{\delta x}{\delta t} \quad , \quad \mathbf{c}_{5-8} = \sqrt{2} \begin{bmatrix} \cos(2i-9)\pi/4 \\ \sin(2i-9)\pi/4 \end{bmatrix} \frac{\delta x}{\delta t} \quad . \quad (\text{A.14})$$

The lattice weight factors are $\omega_0 = 4/9$, $\omega_{1-4} = 1/9$, and $\omega_{5-8} = 1/36$; and the lattice sound speed $c_s = 1/\sqrt{3}\delta x/\delta t$. δx is the lattice grid resolution.

Appendix B

The Analytical Solution for Developed Thermal Flow

For a fully developed incompressible flow between two parallel plates of a separation H , the streamwise velocity is

$$u_x(y) = \frac{3}{2}U_0 \left[1 - \left(\frac{2y}{H} \right)^2 \right] , \quad (\text{B.1})$$

and the transverse velocity is $u_y = 0$. Here U_0 is the mean velocity and the transverse coordinate y measures from the centerline at $y = 0$. The two channel walls then locate at $y = \pm H/2$. For the steady thermal flow simulated in Sect. 3.3.1, the energy equation Eq. (3.3) is simplified to

$$\frac{3}{2}U_0 \left[1 - \left(\frac{2y}{H} \right)^2 \right] \frac{\partial T}{\partial x} = \alpha \left(\frac{\partial^2 T}{\partial x^2} + \frac{\partial^2 T}{\partial y^2} \right) . \quad (\text{B.2})$$

Following Ref. [6], we define the new coordinates as $\bar{y} = 2y/H$ and $\bar{x} = \frac{2x/H}{PrRe'}$, where the Reynolds number is given as $Re' = 2U_0H/\nu$. Please note here the Reynolds number Re' is different from the Reynolds number $Re = U_0H/\nu$ used in Sect. 3.3.1. The energy equation Eq. (B.2) can then be written as

$$\frac{3}{8} (1 - \bar{y}^2) \frac{\partial T}{\partial \bar{x}} = \frac{\partial^2 T}{\partial \bar{y}^2} + \left(\frac{1}{PrRe'} \right)^2 \frac{\partial^2 T}{\partial \bar{x}^2} . \quad (\text{B.3})$$

To represent the similar temperature profile along this uniform duct, the temperature field is assumed as a product of a function Y (which only has \bar{y} as the variable) and a decaying function $e^{-8\lambda^2\bar{x}/3}$ along the flow direction:

$$T(\bar{x}, \bar{y}) = Y(\bar{y})e^{-\frac{8}{3}\lambda^2\bar{x}} . \quad (\text{B.4})$$

Here the parameter λ is called the eigenvalue and its value will be determined next. For the periodic situation in this study, we are only interested in the first eigenvalue and its corresponding mode, since higher order modes have disappeared in the developing region due to their faster decaying speed. Eq. (B.4) is now further simplified to a differential equation of function Y only as

$$Y'' + \left[1 + \left(\frac{8\lambda}{3PrRe'} \right)^2 \right] \lambda^2 Y - \lambda^2 \bar{y}^2 Y = 0 . \quad (\text{B.5})$$

Considering the flow and temperature symmetry about the channel centerline at $\bar{y} = 0$, we further express the function Y as a polynomial series of only even order terms:

$$Y(\bar{y}) = \sum_{i=0}^{\infty} b_i \bar{y}^{2i} . \quad (\text{B.6})$$

Submitting this series expression into Eq. (B.5) yields the following recursion relationships among the coefficients b_i :

$$b_0 = 1; \quad b_1 = \frac{mb_0}{2}; \quad b_i = \frac{mb_{i-1} + nb_{i-2}}{2(i+1)(2i+1)} \quad (i = 2, 3, 4, \dots) , \quad (\text{B.7})$$

with

$$m = - \left[1 + \left(\frac{8\lambda}{3PrRe'} \right)^2 \right] \lambda^2 ; n = \lambda^2 . \quad (\text{B.8})$$

A trial-and-error procedure is required to determine the value λ [6]. Here we start with the value of 1.6815953222 from Ref. [6], and a set of coefficients b_i (up to the 50th term in our calculation) can be calculated from Eq. (B.7). The function value of $Y(\bar{y} = 0)$ is then obtained from Eq. (B.6), and the difference between $Y(\bar{y} = 0)$ and 0 (the wall temperature requirement) can serve as the criterion to refine the λ value, until a satisfactory resolution is reached. For the system considered in this appendix with

$Pr = 0.7$ and $Re = 40$, the eigenvalue obtained from this trial-and-error process is $\lambda=1.675516290994$, which is slightly lower than the value from Ref. [6]. The Nusselt number can also be readily calculated from the calculated temperature profile from this λ value, in combination of the parabolic Poiseuille flow velocity Eq. (B.1). The analytical Nusselt number is constant along the channel of 3.7723, slightly larger than that in Ref. [6] (3.7704) where axial diffusion is neglected. This is reasonable since the axial diffusion effect enhances the heat transfer efficiency of the system; however with a relatively large Peclet number $Pe = RePr = 28$ here, the diffusion contribution to the overall heat transfer is not significant.

Reference

- [1] T. Adachi and H. Uehara. "Correlation between heat transfer and pressure drop in channels with periodically grooved parts". In: *International Journal of Heat and Mass Transfer* 44 (2001), p. 4333.
- [2] H. M. S. Bahaidarah, N. K. Anand, and H. C. Chen. "A numerical study of fluid flow and heat transfer over a bank of flat tubes". In: *Numerical Heat Transfer, Part A: Applications* 47 (2005), p. 417.
- [3] O. O. Bamiro and W. W. Liou. "A direct heating immersed boundary-lattice Boltzmann method for thermal flows". In: *International Journal of Numerical Methods for Heat and Fluid Flow* 24 (2014), pp. 169–200.
- [4] S. M. Becker and A. V. Kuznetsov. *Transport in Biological Media*. New York: Academic Press, 2013.
- [5] M. Bouzidi, D. d'Humieres, P. Lallemand, and L. Luo. "Lattice Boltzmann equation on a two-dimensional rectangular grid". In: *Journal of Computational Physics* 172 (2001), pp. 704–717.
- [6] G. M. Brown. "Entrainment of air into a liquid spray". In: *AIChE Journal* 6 (1960), p. 179.
- [7] S. Chapman and T. G. Cowling. *The Mathematical Theory of Non-Uniform Gases*. Cambridge University Press, 1970.
- [8] L. Chen, Q. Kang, B. A. Robinson, Y.-L. He, and W.-Q. Tao. "Pore-scale modeling of multiphase reactive transport with phase transitions and dissolution-precipitation processes in closed systems". In: *Physical Review E* 87 (2013), p. 043306.

- [9] L. Chen, Q. Kang, B. Carey, and W. Q. Tao. "Pore-scale study of diffusion-reaction processes involving dissolution and precipitation using the lattice Boltzmann method". In: *International Journal of Heat and Mass Transfer* 75 (2014), 483496.
- [10] Q. Chen, X. Zhang, and J. Zhang. "Effects of Reynolds and Prandtl numbers on heat transfer around a circular cylinder by the simplified thermal lattice Boltzmann model". In: *Communications in Computational Physics* 17 (2015), pp. 937–959.
- [11] Q. Chen, X. Zhang, and J. Zhang. "Improved treatments for general boundary conditions in lattice Boltzmann method for convection-diffusion and heat transfer processes". In: *Physical Review E* 88 (2013), p. 033304.
- [12] S. Chen, B. Yang, and G. Zheng. "A lattice Boltzmann model for heat transfer in heterogeneous media". In: *International Journal of Heat and Mass Transfer* 102 (2016), pp. 637–644.
- [13] A. R. R. Darzi, M. Farhadi, M. Jourabian, and Y. Vazifeshenas. "Natural convection melting of NEPCM in a cavity with an obstacle using lattice Boltzmann method". In: *International Journal of Numerical Methods for Heat and Fluid Flow* 24 (2014), pp. 221–236.
- [14] P. R. Di Palma, C. Huber, and P. Viotti. "A new lattice Boltzmann model for interface reactions between immiscible fluids". In: *Advances in Water Resources* 82 (2015), pp. 139–149.
- [15] M. Greiner, R. J. Faulkner, V. T. Van, H. M. Tufo, and P. F. Fischer. "Simulations of three-dimensional flow and augmented heat transfer in a symmetrically grooved channel". In: *ASME Journal of Heat Transfer* 122 (2000), p. 653.
- [16] K. Guo, L. Li, G. Xiao, N. AuYeung, and R. Mei. "Lattice Boltzmann method for conjugate heat and mass transfer with interfacial jump conditions". In: *International Journal of Heat and Mass Transfer* 88 (2015), pp. 306–322.
- [17] Z. Guo and C. Shu. *Lattice Boltzmann Method and Its Applications in Engineering*. Singapore: World Scientific Publishing, 2013.

- [18] Z. Guo and T. S. Zhao. "Lattice Boltzmann model for incompressible flows through porous media". In: *Physical Review E* 66 (2002), p. 036304.
- [19] Z. Guo, C. Zheng, and B. Shi. "An extrapolation method for boundary conditions in lattice Boltzmann method". In: *Physics of Fluids* 14 (2002), pp. 2007–2010.
- [20] Z. Guo, C. Zheng, and B. Shi. "Discrete lattice effects on the forcing term in the lattice Boltzmann method". In: *Physical Review E* 65 (2002), p. 046308.
- [21] Y. Han and P. A. Cundal. "Lattice Boltzmann modeling of pore-scale fluid flow through idealized porous media". In: *International Journal for Numerical Methods in Fluids* 67 (2011), pp. 1720–1734.
- [22] X. He, S. Chen, and G. D. Doolen. "A novel thermal model for the lattice Boltzmann method in incompressible limit". In: *Journal of Computational Physics* 146 (1998), p. 282.
- [23] X. He, L. Luo, and M. Dembo. "Some progress in lattice Boltzmann method: Part I. Nonuniform mesh grids". In: *Journal of Computational Physics* 129 (1996), pp. 357–363.
- [24] L. A. Hegele Jr, K. Mattila, and P. C. Philippi. "Rectangular lattice-Boltzmann schemes with BGK-collision operator". In: *Journal of Scientific Computing* 56 (2013), pp. 230–242.
- [25] D. Hlushkou, D. Kandhai, and U. Tallarek. "Coupled lattice-Boltzmann and finite-difference simulation of electroosmosis in microfluidic channels". In: *International Journal for Numerical Methods in Fluids* 46 (2004), pp. 507–532.
- [26] J. P. Holman. *Heat Transfer*. New York: McGraw-Hill, 1968.
- [27] Y. Hu, D. Li, S. Shu, and X. Niu. "Full Eulerian lattice Boltzmann model for conjugate heat transfer". In: *Physical Review E* 92 (2015), p. 063305.
- [28] R. Huang and H. Wu. "Phase interface effects in the total enthalpy-based lattice Boltzmann model for solid-liquid phase change". In: *Journal of Computational Physics* 294 (2014), pp. 346–362.

- [29] C. Huber, B. Shafei, and A. Parmigiani. "A new pore-scale model for linear and non-linear heterogeneous dissolution and precipitation". In: *Geochimica et Cosmochimica Acta* 124 (2014), pp. 109–130.
- [30] F. P. Incropera, D. P. DeWitt, T. L. Bergman, and A. S. Lavine. *Fundamentals of Heat and Mass Transfer*. 6th Ed. New York: John Wiley & Sons, 2006.
- [31] D. B. Ingham and I. Pop. *Transport Phenomena in Porous Media*. 1st. Kidlington, UK: Pergamon, 1998.
- [32] John D. Anderson Jr. *Computational Fluid Dynamics*. McGraw-Hill Education, 2012.
- [33] C. Aidun K. and J. R. Clausen. "Lattice-Boltzmann method for complex flows". In: *Annual Review of Fluid Mechanics* 42 (2010), pp. 439–472.
- [34] N. F. A. Kadir, D. A. S. Rees, and I. Pop. "Conjugate forced convection flow past a circular cylinder with internal heat generation in a porous medium". In: *International Journal of Numerical Methods for Heat and Fluid Flow* 18 (2008), pp. 730–744.
- [35] Q. Kang, P. C. Lichtner, and D. R. Janecky. "Lattice Boltzmann method for reacting flows in porous media". In: *Advances in Applied Mathematics and Mechanics* 2 (2010), pp. 545–563.
- [36] H. Karani and C. Huber. "Lattice Boltzmann formulation for conjugate heat transfer in heterogeneous media". In: *Physical Review E* 91 (2015), p. 023304.
- [37] T. Kruger, H. Kusumaatmaja, A. Kuzmin, O. Shardt, G. Silva, and E. M. Viggen. *The Lattice Boltzmann Method Principles and Practice*. Springer, 2017.
- [38] G. Le, O. Oulaid, and J. Zhang. "Counter-extrapolation method for conjugate interfaces in computational heat and mass transfer". In: *Physical Review E* 91 (2015), p. 033306.
- [39] G. Le and J. Zhang. "Boundary slip from the immersed boundary lattice Boltzmann models". In: *Physical Review E* 79 (2009), p. 026701.

- [40] L. Li, C. Chen, R. Mei, and J. F. Klausner. "Conjugate heat and mass transfer in the lattice Boltzmann equation method". In: *Physical Review E* 89 (2014), p. 043308.
- [41] Q. Li, K.H. Luo, Q.J. Kang, Y.L. He, Q. Chen, and Q. Liu. "Lattice Boltzmann methods for multiphase flow and phase-change heat transfer". In: *Progress in Energy and Combustion Science* 52 (2016), pp. 62–105.
- [42] S. Maruyama and T. Kimura. "A Study on Thermal Resistance over a Solid-Liquid Interface by the Molecular Dynamics Method". In: *Thermal Science and Engineering* 7 (1999), pp. 63–68.
- [43] P. Meng, M. Wang, and Z. Li. "Lattice Boltzmann simulations of conjugate heat transfer in high-frequency oscillating flows". In: *International Journal of Heat and Fluid Flow* 29 (2008), pp. 1203–1210.
- [44] A. A. Mohamad. "Simulation of flow and conjugate heat transfer in a macrochannel via lattice Boltzmann method". In: *Proceedings of the ASME International Mechanical Engineering Congress and Exposition 2007* (2008), pp. 1341–1346.
- [45] M. J. Moran, H. N. Shapiro, and D. D. Boettner. *Fundamentals of Engineering Thermodynamics 7th edition*. Wiley, 2010.
- [46] J. W. Murraya, J. Sunb, D. V. Patilb, T. A. Woodc, and A. T. Clarea. "Physical and electrical characteristics of EDM debris". In: *J. Mater. Process. Technol.* 229 (2016), pp. 54–60.
- [47] B. Niceno and E. Nobile. "Numerical analysis of fluid flow and heat transfer in periodic wavy channels". In: *International Journal of Heat and Fluid Flow* 22 (2001), p. 156.
- [48] C. Nonino, S. Savino, and S. Del Giudice. "FEM for the 3-D analysis of conjugate conduction-convection heat transfer in cross-flow microheat exchangers". In: *International Journal of Numerical Methods for Heat and Fluid Flow* 25 (2015), pp. 1322–1339.

- [49] O. Oulaid, Q. Chen, and J. Zhang. "Accurate boundary treatments in lattice Boltzmann method for electric field and electro-kinetic applications". In: *Journal of Physics A: Mathematical and Theoretical* 46 (2013), p. 475501.
- [50] O. Oulaid and J. Zhang. "On the origin of numerical errors in the bounce-back boundary treatment of the lattice Boltzmann method: a remedy for artificial boundary slip and mass leakage". In: *European Journal of Mechanics - B/Fluids* 53 (2015), pp. 11–23.
- [51] S. V. Patankar, C. H. Liu, and E. M. Sparrow. "Fully Developed Flow and Heat Transfer in Ducts Having Streamwise-Periodic Variations of Cross-Sectional Area". In: *ASME Journal of Heat Transfer* 99 (1977), p. 180.
- [52] H. A. Patel, S. Garde, and P. Keblinski. "Thermal Resistance of Nanoscopic Liquid-Liquid Interfaces: Dependence on Chemistry and Molecular Architecture". In: *Nano Letters* 5 (2005), pp. 2225–2231.
- [53] C. Peng, H. Min, Z. Guo, and L. Wang. "A hydrodynamically-consistent MRT lattice Boltzmann model on a 2D rectangular grid". In: *Journal of Computational Physics* 326 (2016), pp. 893–912.
- [54] A. G. Ramgadia and A. K. Saha. "Three-dimensional numerical study of turbulent flow and heat transfer in a wavy-walled duct". In: *International Journal of Thermal Sciences* 67 (2013), p. 152.
- [55] A. K. Saha and S. Acharya. "Unsteady RANS simulation of turbulent flow and heat transfer in ribbed coolant passages of different aspect ratios". In: *International Journal of Heat and Mass Transfer* 48 (2005), pp. 4704–4725.
- [56] M. Seddiq, M. Maerefat, and M. Mirzaei. "Modeling of heat transfer at the fluid-solid interface by lattice Boltzmann method". In: *International Journal of Thermal Sciences* 75 (2014), pp. 28–35.
- [57] C. Semperebon, T. Kruger, and H. Kusumaatmaja. "Ternary free-energy lattice Boltzmann model with tunable surface tensions and contact angles". In: *Physical Review E* 93 (2016), p. 033305.

- [58] W. Song and B. Q. Li. "Finite element solution of conjugate heat transfer problems with and without the use of gap elements". In: *International Journal of Numerical Methods for Heat and Fluid Flow* 12 (2002), pp. 81–99.
- [59] E. Stalio and M. Piller. "Direct numerical simulation of heat transfer in converging–diverging wavy channels". In: *ASME Journal of Heat Transfer* 129 (2007), p. 769.
- [60] W. D. Stein. *Transport and Diffusion across Cell Membranes*. London, UK: Academic Press, 1985.
- [61] S. Succi. *The Lattice Boltzmann Equation*. Oxford: Oxford Univ. Press, 2001.
- [62] S. Succi. *The Lattice Boltzmann equation for Fluid Dynamics and Beyond*. Springer, 2017.
- [63] J. Tu, G. H. Yeoh, and C. Liu. *Computational Fluid Dynamics 3rd Edition*. Butterworth-Heinemann, 2018.
- [64] H. K. Versteeg and W. Malalasekera. *An Introduction to Computational Fluid Dynamics*. Harlow, UK: Pearson, 2007.
- [65] G. Wang and S. P. Vanka. "Convective heat transfer in periodic wavy passages". In: *International Journal of Heat and Mass Transfer* 38 (1995), p. 3219.
- [66] J. Wang, Q. Kang, L. Chen, and S. S. Rahman. "Pore-scale lattice Boltzmann simulation of micro-gaseous flow considering surface diffusion effect". In: *International Journal of Coal Geology* 169 (2017), pp. 62–73.
- [67] L. Wang, H. Min, C. Peng, N. Geneva, and Z. Guo. "A lattice-Boltzmann scheme of the Navier-Stokes equation on a three-dimensional cuboid lattice". In: *Computers and Mathematics with Applications* 78 (2016).
- [68] Z. Wang, H. Shang, and J. Zhang. "Lattice Boltzmann simulations of heat transfer in fully developed periodic incompressible flows". In: *Physical Review E* 95 (2017), p. 063309.
- [69] Z. Wang and J. Zhang. "Simulating anisotropic flows with isotropic lattice models via coordinate and velocity transformation". In: *International Journal of Modern Physics C* 30 (2019), p. 1941001.

- [70] Z. Wang, F. Colin, G. Le, and J. Zhang. "Counter-extrapolation method for conjugate heat and mass transfer with interfacial discontinuity". In: *International Journal of Numerical Methods for Heat & Fluid Flow* 27 (2017), pp. 2231–2258.
- [71] F. H. White. *Fluid Mechanics 7th edition*. Springer, 2017.
- [72] D. A. Wolf-Gladrow. *Lattice-Gas Cellular Automata and Lattice Boltzmann Models: An Introduction*. Berlin, Germany: Springer, 2000, p. 180.
- [73] W. Xiong and J. Zhang. "A two-dimension lattice Boltzmann model for Uniform channel flows". In: *Computers and Mathematics with Applications* 61 (2011), pp. 3453–3460.
- [74] X. Yang, H. Huang, and X. Lu. "Sedimentation of an oblate ellipsoid in narrow tubes". In: *Physical Review E* 92 (2015), p. 063009.
- [75] X. Yin and J. Zhang. "An improved bounce-back scheme for complex boundary conditions in lattice Boltzmann method". In: *Journal of Computational Physics* 231 (2012), pp. 4295–4303.
- [76] H. Yoshida, T. Kobayashi, H. Hayashi, T. Kinjo, H. Washizu, and K. Fukuzawa. "Boundary condition at a two-phase interface in the lattice Boltzmann method for the convection-diffusion equation". In: *Physical Review E* 90 (2014), p. 013303.
- [77] C. Zhang, Y. Cheng, J. Wu, and W. Diao. "Lattice Boltzmann simulation of the open channel flow connecting two cascaded hydropower stations". In: *Journal of Hydrodynamics, Ser. B* 28 (2016), pp. 400–410.
- [78] J. Zhang. "Lattice Boltzmann method for microfluidics: models and applications". In: *Microfluidics and Nanofluidics* 10 (2011), pp. 1–28.
- [79] J. Zhang, P. C. Johnson, and A. S. Popel. "An immersed boundary lattice Boltzmann approach to simulate deformable liquid capsules and its application to microscopic blood flows". In: *Physical Biology* 4 (2007), pp. 285–295.
- [80] J. Zhang and D. Y. Kwok. "A 2D lattice Boltzmann study on electrohydrodynamic drop deformation with the leaky dielectric theory". In: *Journal of Computational Physics* 206 (2005), pp. 150–161.

-
- [81] J. Zhang and D. Y. Kwok. "Pressure boundary condition of the lattice Boltzmann method for fully developed periodic flows". In: *Physical Review E* 73 (2006), p. 047702.
- [82] T. Zhang, B. Shi, Z. Chai, and F. Rong. "Lattice BGK model for incompressible axisymmetric flows". In: *Communications in Computational Physics* 11 (2012), pp. 1569–1590.
- [83] Y. Zhang, R. Qin, and D. R. Emerson. "Lattice Boltzmann simulation of rarefied gas flows in microchannels". In: *Physical Review E* 71 (2005), p. 047702.
- [84] J. Zhou. "MRT rectangular lattice Boltzmann method". In: *International Journal of Modern Physics C* 23 (2012), p. 1250040.
- [85] J. Zhou. "Rectangular lattice Boltzmann method". In: *Physical Review E* 81 (2010), p. 026705.
- [86] Y. Zong, C. Peng, Z. Guo, and L. Wang. "Designing correct fluid hydrodynamics on a rectangular grid using MRT lattice Boltzmann approach". In: *Computers and Mathematics with Applications* 72 (2016), pp. 288–310.
- [87] Q. Zou and X. He. "On pressure and velocity boundary conditions for the lattice Boltzmann BGK model". In: *Physics of Fluids* 9 (1997), pp. 1591–1598.